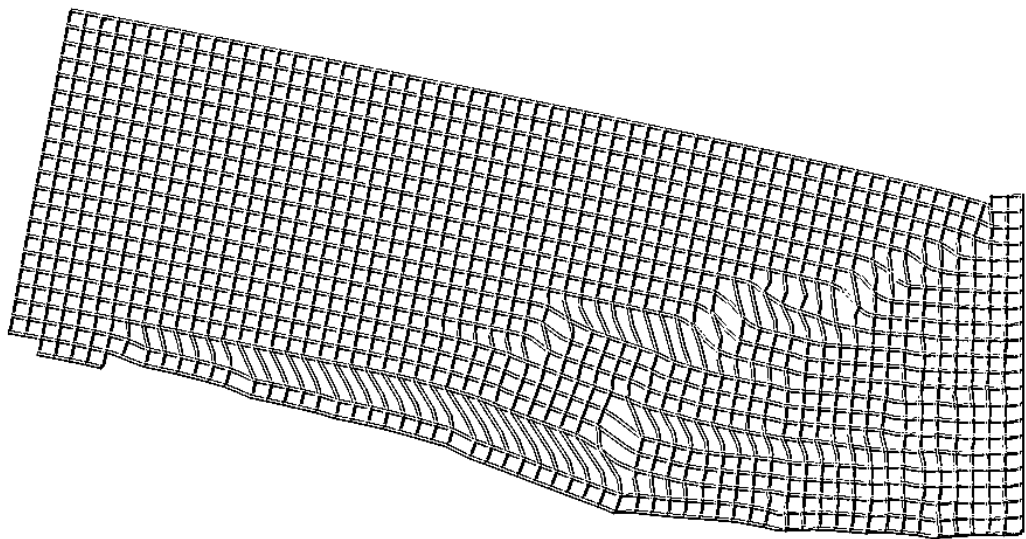


DELFT UNIVERSITY OF TECHNOLOGY

Non-Linear Finite Element Analysis of Shear Critical Reinforced Concrete Beams



MASTER THESIS REPORT

THIJS CLAUS

DELFT UNIVERSITY OF TECHNOLOGY

**Non-Linear Finite Element Analysis of
Shear Critical Reinforced Concrete
Beams**

by

Thijs Thomas Bernard Claus

A thesis submitted in partial fulfillment for the
degree of Master of Science

Civil Engineering and Geosciences
Department of Structural Engineering

April 2009

Preface

This document contains the Master thesis report: non-linear finite element analysis of shear critical reinforced concrete beams. This thesis is part of obtaining the degree of Master of Science at the faculty of Civil Engineering, Delft University of Technology. The author would like to express his gratitude towards his supervisors, in particular mr. Hendriks, for sharing their knowledge and their support during the realization of this thesis.

Examination committee:

Prof. Dr. Ir. J.G. Rots

Delft University of Technology | Civil Engineering and Geosciences | Computational Modeling of Structures

Dr. Ir. M.A.N. Hendriks

Delft University of Technology | Civil Engineering and Geosciences | Computational Modeling of Structures

Dr. Ir. P.H. Feenstra

Delft University of Technology | Civil Engineering and Geosciences | Computational Modeling of Structures

Dr. Ir. C. van der Veen

Delft University of Technology | Civil Engineering and Geosciences | Concrete Structures

Ir. L.J.M Houben

Delft University of Technology | Civil Engineering and Geosciences | Road and Railway Engineering

Abstract

This thesis concerns the computational aspects of non-linear finite element analysis (NLFEA) for shear critical reinforced concrete beams. This implies, modeling the behavior of reinforced concrete beams under shear loading up to failure using the finite element method. The objective was to investigate a number of aspects of NLFEA, such as: material parameters, constitutive model parameters, spatial discretization aspects, and incremental-iterative procedure aspects. Furthermore, an objective was to investigate the possibilities and limitations of smeared and discrete crack analysis. To this end, two benchmark studies were performed on two shear critical beams.

Both benchmark beams were obtained from a recent workshop on the assessment of the shear strength of concrete structures [26]. The beams are identified as benchmark beam A and benchmark beam B. Benchmark A is a normal size and strength beam loaded by a 3-point bending test. The beam is only reinforced with longitudinal reinforcement at the underside and in the web of the beam. The second benchmark, beam B, is a normal strength beam loaded by a 4-point bending test. The cross-section of the beam can be considered slender, with only one layer of reinforcement at the underside of the beam. A characteristic of both beams is that they do not contain shear reinforcement, this proved to be of significant importance for the structural response.

It was concluded that the very nature of the shear critical beams leads to a more problematic non-linear analysis than for example, a bending beam. The main structural characteristics of shear critical beams were found to be: brittle behavior, bi-axial stress states, and rotations of principal directions upon crack formation. These structural responses had a strong effect on the convergence characteristics of the incremental-iterative procedure. Only through extensive measures could a numerical equilibrium be obtained in every instance. These measures included: using a displacement controlled procedure, using small increment-size, allowing for a large number of iterations, using line searches, and using a secant stiffness based iteration method.

After a variational study of the constitutive models and material parameters, it was found that the tensile strength has a significant influence on the structural behavior of the beam, the failure mode and the ultimate shear load. It was also concluded that, next to the tensile behavior, it is necessary to include compressive softening in the constitutive model of concrete. Including compressive softening is important for the accurate representation of the formation and degradation of the compression struts.

Due to the bi-axial stress fields and the reinforcement action, the principal stress and strain directions showed rotation during the entire loading process. This rotation of principal directions proved to be of importance for the selected crack models. The crack models used in this thesis were based on the principles of the so-called smeared crack formulations. In total three crack models were investigated, namely: fixed, fixed multidirectional and rotating crack models. The following conclusions were established after analyzing benchmark A. The fixed crack model in combination with a constant shear retention factor proved to lead to very poor structural behavior. This was mainly due to excessive stress-locking through shear stresses on the crack faces. A fixed crack model based on variable shear retention, displayed slightly less stress-locking than compared to a constant shear retention, but not to such a degree that it constituted an accurate representation of the behavior of the beam. The multidirectional proved to be numerically unstable, and a structural response could not be obtained. The rotating crack model exhibited good structural responses and provided a reasonable approximation of the experimental results regarding the failure modes and ultimate failure loads. The predicted crack patterns of the rotating crack model were however substandard. And although the rotating crack model was not affected by stress-locking, it did prove to lead to the over-rotation of cracks in which the consequences were un-realistic strain-localizations.

Benchmark B could not be properly analyzed with a smeared crack formulation, therefore, a discrete crack approach was applied. The structural results from the discrete crack model were in good agreement with the experimental results, in both the failure mode as well as the failure load. The discrete crack analysis also displayed the formation of a very large bending crack constituting a severe snap-through in the load-displacement behavior. This crack formation corroborated the conclusions why the smeared crack models could not lead to correct structural response. The discrete crack analysis was extended with two different formulations for the modeling of aggregate interlock. It was found that, for this particular benchmark, that the aggregate interlock models had little influence on the overall behavior of the beam.

In relation to the spatial discretization, it was found that for benchmark beam A, quadrilateral elements perform optimally when the aspect ratio is close to 1.0 [-]. The crack formation and propagation with these types of elements, were in good agreement with the experimental results. However, from analyzing different mesh dimensions it was concluded that a significant dimensional bias exist, leading to large differences ($\simeq 20\%$) in ultimate shear load. Next to the standard rectangular quadrilateral mesh, it was found that a slanted quadrilateral mesh displayed poor structural results in crack formation, crack propagation as well as failure modes and failure loads. The use of triangular elements for the modeling of concrete fracture displayed a distinct directional bias, leading to unrealistic structural results. As a final aspect, the structural results of an entire beam model was investigated and compared versus the structural results of the symmetric model. It was found that the load-displacement behavior was affected on all occasions.

Contents

Preface	iii
Abstract	v
List of Figures	xi
1 Introduction	1
1.1 Background	1
1.2 Aim of the study	2
1.3 Outline of the thesis	3
2 Characteristics of concrete behavior	5
2.1 Uniaxial behavior of plain concrete	5
2.2 Biaxial behavior of plain concrete	5
2.3 Reinforced concrete under axial loading	6
3 RC beams subjected to shear loading	7
3.1 Force distribution	7
3.2 Shear failure mechanisms	7
3.2.1 Flexural shear failure	7
3.2.2 Shear Tension failure	8
3.2.3 Web crushing	9
3.2.4 Yielding of the shear reinforcement	9
3.3 Shear transfer in cracked concrete	9
3.3.1 Aggregate interlock	9
3.3.2 Dowel action	10
3.3.3 Axial steel stress	10
3.3.4 Residual stresses	11
3.3.5 Shear-stress in the compression zone	11
4 Numerical modeling of concrete fracture	13
4.1 Introduction	13
4.2 Discrete crack modeling	14
4.2.1 Interface modeling	14
4.2.2 Crack dilatancy	15
4.3 Smearred crack modeling	16
4.3.1 Smearred crack principle	16
4.3.2 Fixed total strain model	17
4.3.3 Rotating total strain crack model	18
4.3.4 Fixed multidirectional crack model	20
4.4 Tension softening	21
4.5 Shear retention	22

4.6	Unloading and Reloading	23
4.7	Compressive response of cracked reinforced concrete	24
5	Solution techniques NLFEA	25
5.1	The incremental-iterative procedure	25
5.2	Load and displacement control	25
5.3	Iterative procedures	26
5.4	Convergence criteria	27
5.5	Acceleration and arc length techniques	28
5.5.1	Arc length control	28
5.5.2	Line search algorithm	29
6	Benchmark: Beam A	31
6.1	Beam A properties	31
6.1.1	Geometry	31
6.1.2	Materials	31
6.1.3	Load carrying capacity	32
6.1.4	Experimental results	32
6.2	Pre-processing aspects	33
6.2.1	Modeling environment	33
6.2.2	Boundary conditions	33
6.2.3	Element selection	34
6.2.4	Spatial discretization	34
6.2.5	Material modeling	34
6.3	Preliminary analysis	35
6.4	Solution strategies	37
6.4.1	Iteration procedure	37
6.4.2	Norm tolerance	39
6.4.3	Increment size	41
6.4.4	Indirect displacement control	43
6.4.5	Summary	43
6.5	Constitutive model parameters	44
6.5.1	Tensile behavior	44
6.5.2	Tensile strength	45
6.5.3	Tension softening function	48
6.5.4	Mode I fracture energy	48
6.6	Evaluation of crack models	48
6.6.1	Fixed crack model with constant shear retention	49
6.6.2	Fixed crack model with variable shear retention	50
6.6.3	Fixed multi-directional crack model	51
6.6.4	Rotating total strain crack model	52
6.6.5	Summary	55
6.7	Spatial discretization	56
6.7.1	Mesh dimension	57
6.7.2	Mesh alignment	59
6.7.3	Symmetrical modeling	61
6.7.4	Summary	62
6.8	NLFEA versus experimental results	63
7	Benchmark: Beam B	69
7.1	Beam B properties	69
7.1.1	Geometry	69
7.1.2	Materials	69

7.1.3	Load bearing capacity	70
7.1.4	Experimental results	70
7.2	Pre-processing aspects	70
7.2.1	Modeling environment	70
7.2.2	Boundary conditions	71
7.2.3	Element selection	71
7.2.4	Spatial discretization	71
7.2.5	Material modeling	71
7.3	Preliminary analysis: smeared cracking	72
7.3.1	Improving preliminary results: rotating crack model	73
7.3.2	Improving preliminary results: fixed crack model	75
7.3.3	Summary	76
7.4	Preliminary analysis: discrete cracking	77
7.5	Shear formulations for discrete cracking	80
7.6	Symmetrical modeling	81
8	Conclusions and recommendations	85
8.1	Structural behavior of shear critical RC beams	85
8.2	Numerical aspects incremental-iterative analysis	85
8.3	Constitutive model parameters	86
8.4	Crack model evaluation	86
8.5	Spatial discretization	88
8.6	Discrete cracking	88
8.7	Recommendations	89
8.7.1	Recommendations for the NLFEA for shear critical RC beams	89
	Bibliography	91

List of Figures

2.1	Uniaxial behavior of plain concrete	6
2.2	Behavior of concrete under uniaxial tensile loading	6
3.1	Strut and tie model for a concrete beam reinforced with longitudinal and transversal reinforcement	7
3.2	Failure mechanisms of reinforced concrete under shear loading	8
3.3	Shear transfer Mechanisms in cracked concrete	10
4.1	Representation of two types of crack modeling	13
4.2	Coordinate system definitions	14
4.3	Softening diagrams for different crack representations	22
4.4	Shear retention formulations for fixed crack model	23
4.5	Unloading and reloading principles	24
4.6	Reduction compressive strength	24
6.1	Geometry characteristics and crack pattern at moment of failure, the critical crack for which the beam ultimately fails is highlighted. Dimensions are in [mm].	31
6.2	Finite element model beam A	34
6.3	Constitutive models reinforcement and concrete	35
6.4	Load-displacement diagrams for two analysis with different control procedures	36
6.5	Crack patterns at moment of failure of respective analysis	36
6.6	Characteristic behavioral patterns for different iterations methods of the Newton class. The force norm was applied for the analysis shown	39
6.7	Load-displacement diagrams with norm and increment variation	40
6.8	Crack patterns at respective moments of failure	41
6.9	Performance characteristics BFGS method with varying increment-sizes	42
6.10	Performance characteristics mN-R method with varying increment-sizes	42
6.11	Load-displacement diagram for a fully converged solution and a non-full converged solution	44
6.12	Load-displacement diagram for different constitutive model parameters	45
6.13	Principal tensile strain ϵ_1 at moment of failure of respective analysis.	46
6.14	Principal compressive strain ϵ_2 at moment of failure of respective analysis.	46
6.15	Load displacement diagrams for analysis with varying tensile strength and compressive fracture energy	47
6.16	Load-displacement diagram with fixed and rotating smeared crack models	49
6.17	Crack patterns for fixed crack model with shear retention $\beta=0.05$ (top) and $\beta=0.005$ (bottom). Only cracks are portrayed that have either undergone full mode I softening or display crack shear stresses s_{nt} of larger than 0.5 N/mm^2	50
6.18	Crack patterns for fixed crack model with shear retention $\beta=0.005$. Only cracks are portrayed that have either undergone full mode I softening or display crack shear stresses s_{nt} of larger than 0.5 N/mm^2	51
6.19	Crack-pattern at the moment of last converged increment for the multi-directional fixed model	52

6.20	Crack patterns for rotating crack model, only cracks that have undergone full mode I softening are depicted	53
6.21	Crack patterns at the location of the main longitudinal reinforcement of the beam near the support, only cracks that have undergone full mode I softening are depicted. The blue lines indicate the reinforcement.	53
6.22	Deformed mesh plots at moment of failure, deformations are exaggerated	54
6.23	Strain evolution of an element containing reinforcement using the rotating crack model	55
6.24	Investigated mesh designs	56
6.25	Load-displacement diagram for three different mesh dimensions	57
6.26	Principal tensile strain ϵ_1 for two different mesh dimensions at 2.50 [mm] displacement	58
6.27	Crack patterns at 2.0 [mm] displacement for different quadrilateral mesh dimensions	58
6.28	Contour plot shear strains ϵ_{xy} at moment of failure of respective analysis are portrayed. The reinforcement is indicated with blue lines	59
6.29	Crack patterns and strain ϵ_{xx} contour plots for triangular mesh designs at 2.0 [mm] displacement	60
6.30	Crack pattern for slant quadrilateral mesh	61
6.31	Crack patterns of entire beam model	62
6.32	Load-displacement diagram for experimental results and numerical analysis results	64
6.33	Crack patterns obtained from experimental results and from numerical analysis .	66
6.34	Crack patterns obtained from experimental results and from numerical analysis .	67
7.1	Geometry characteristics and crack pattern at moment of failure, the critical crack for which the beam ultimately fails is highlighted. Dimensions are in [mm]. . . .	69
7.2	Finite element model beam B	72
7.3	Constitutive models reinforcement and concrete	72
7.4	Load-displacement diagram with indication of critical events	73
7.5	Crack patterns during loading of smeared crack analysis beam B	74
7.6	Load-displacement diagram using a fixed model and 'forcing' the analysis	76
7.7	Crack patterns during loading of rotating crack model beam B	77
7.8	Discrete crack-pattern used in preliminary analysis	78
7.9	Load-displacement diagram for discrete crack model	79
7.10	Crack patterns a various stages of loading	79
7.11	Load-displacement diagram for discrete crack model with shear stiffness formulations	80
7.12	Crack-width and shear-stress on crack-faces with constant shear stiffness, at 70.0 [mm] displacement	81
7.13	Crack-width and shear-slip on crack-faces employing the rough crack model. Displayed increments represent the moment of failure	82
7.14	Load-displacement diagram for entire beam and symmetric beam models	82
7.15	Deformed models at respective moments of failure, deformations are exaggerated.	83

1. Introduction

1.1 Background

A number of uncertainties have recently risen regarding the shear capacity of concrete structures that were built during the period between the 1960's and the 1980's. These uncertainties arose from recent investigations into the (remaining) service-life of these concrete structures [18]. The main focus of the investigations was placed upon on bridge structures and similar types of structures such as viaducts and tunnels.

The reasons for these uncertainties are the fact that: building codes, traffic loads and traffic concentrations have undergone considerable changes since the period of time in which these structures were built. For example, there have been significant changes in the understanding of the materials and the mechanics involved with these structures. Also, traffic concentration increased, load per vehicle increased, and safety standards have risen to a stricter level. All of these factors combined have lead to questions whether these concrete structures have sufficient or additional load-carrying capacity.

To provide an answer for these question, a need was expressed to assess structures on their shear capacity using modern numerical methods such as the non-linear finite element analysis (NLFEA). In using numerical methods, the aim is to accurately predict the shear capacity, and assess whether the current safety standards are met and whether structures have additional load-carrying capacity.

At the moment, the use of NLFEA is becoming more and more widespread within the everyday practice of the structural engineer. This increase in use is mainly related to the previously stated circumstances regarding the strength and structural integrity of the damaged or deteriorated concrete structures. Despite this increasing use and accompanying sophistication of non-linear methods and computational abilities, the reliability of the results are very dependent on the expertise of the user and the selected models. This was particularly visible in a recent workshop on the shear strength concrete structures subjected to shear loading [26]. In this workshop two different NLFEA were compared with several analytical methods to provide an estimate for the ultimate shear load of several shear critical RC beams. Although both finite element analysis considered the same RC beams, the results showed significant differences between the analysis. The predicted ultimate shear loads ranged from 30 to 60% in comparison to the experimentally obtained ultimate shear load values.

One of the main reasons why the results of NLFEA lack in consistency, is a consequence of the fact that, to accurately predict the cracking of concrete, extensive models are necessary to ensure proper structural results. Over the years, a number of approaches were developed for non-linear modeling of concrete. Among the available options are: non-linear elasticity, plasticity, damage continuum, and smeared crack formulations. Most of these approaches are suited for certain

structures or loading situations. But there is no approach that performs well over the entire range of structural applications [23]. Selecting the correct constitutive and crack model for the given situation is therefore of critical importance.

Not only the lack of one single approach has hampered the analysis of shear critical RC beams, but also the very nature of shear beams has been the cause for large difficulties. This is because, unlike bending (mode I) failure, stress-states in shear critical beams tend to be particularly biaxial. The consequence of this being that intricate algorithms are necessary to properly portray these stress-states. Furthermore, the crack formations in shear critical beams are generally appear sudden which leads to brittle load-displacement behavior. Next to the brittle behavior, a number of complex load-carrying mechanisms occur in the cracked concrete, such as aggregate interlock and dowel action.

The consequence of these sudden crack formations and brittle behavior, is that a number of problems are encountered with regards to obtaining an equilibrium situation and the accurateness of this equilibrium situation. Because non-linear finite element analysis requires an incremental-iterative procedure to find a solution, the calculation process becomes considerably more complex. One of the main reason for this is the fact that the iterative procedure are based on stiffness formulation that rely on a reasonable prediction of the structure stiffness in the following loading increment. When this stiffness is strongly affected, for example due to large and sudden crack formations, or when multiple cracks localize in the same increment, convergence is difficult to obtain. Therefore, finding a solution within the boundaries of the error margin, requires a detailed strategy to assure the correctness of the solution.

1.2 Aim of the study

As was stated in the introduction, large variations are present in the results of finite element analysis of shear critical RC beams. These variations are related to: the accurateness of the obtained solutions, the identification of critical constitutive model parameters, the suitability of the employed crack models, and the dependency of structural results on the spatial discretization. To obtain insight into these factors, two benchmark studies of different shear critical beams will be employed to systematically map out the mentioned aspects. To clarify the assumptions that are inherent to the title and the aim of this study, we consider the following definitions:

- A shear critical beams is a beam that fails due to a shear failure mechanism, these mechanisms have described in section 3.2.
- With the definition non-linear finite element analysis only physically non-linear material behavior is implied.
- The RC beams in question will be proportionally loaded to their moments of failure.

1.3 Outline of the thesis

The thesis will start with a short introduction of the general behavior of concrete. Plain and reinforced concrete under axial and biaxial loading are discussed, and the principles of tension softening and tension stiffening. Following the general behavior of concrete an overview will be given, regarding the characteristics of concrete beams under shear loading. This includes: shear failure mechanisms, and shear stress transfer mechanisms. Next to the characteristics of the behavior of RC beams, an overview will be given on the numerical crack models that are applied in this thesis. There will be a main subdivision between discrete and smeared crack formulations. Discrete modeling will include the treatment of the constitutive relations for the use of line interfaces and the application of dilatancy models. The section on smeared crack modeling will treat models based on the total strain and decomposed strain formulations as well as the fixed and rotating crack models. As a final aspect, an overview will be given on the principles behind the incremental-iterative analysis. This includes the applied iterative methods, convergence criteria, load versus displacement control and the available acceleration techniques to improve convergence.

These preliminary chapters will form the basis for the first benchmark study which has been identified as beam A. Following pre-processing aspects this beam will be scrutinized on a number of different aspects, namely: the incremental-iterative procedure and its solution strategies, constitutive model parameters, crack model evaluation and the aspects of spatial discretization. The second benchmark study has been identified as beam B. The analysis of this beam consist of a so-called discrete crack analysis in which the crack have been implemented into the finite element model at a predefined location. The discrete crack analysis will consider different shear-formulations, and modeling aspects. The final chapter of this thesis contains the conclusions and recommendations regarding the findings of the benchmark studies.

The analysis in this thesis will be performed using the DIANA finite element code version 9.2.

2. Characteristics of concrete behavior

This chapter will shortly discuss a number of principles relating to the structural behavior of concrete and reinforced concrete. These principles include uniaxial and biaxial behavior and tension softening and stiffening phenomena.

2.1 Uniaxial behavior of plain concrete

When concrete is loaded in uniaxial tension, the starting load-path is governed by the elastic stiffness E_c . At approximately 60 to 80% of the tensile strength f_t , micro-cracks begin to form reasonably uniform through-out the specimen, resulting in a reduced stiffness. Due to the quasi-brittle nature of concrete, the tensile stresses do not reduce to zero upon reaching the ultimate tensile load. After the peak, the damage in the concrete starts to localize into a fracture zone at the weakest section while the remaining part of the specimen undergoes unloading. This behavior is known as strain-localization. Upon further loading the tensile stress reduces gradually with increasing deformation until a complete separation occurs. The negative branch of the stress-strain curve is known as the tension softening branch. A typical stress-strain curve of this behavior is depicted in figure 2.1a.

Concrete in uniaxial compression shows similar behavior as uniaxial tension. The response of concrete is linear-elastic up to about 30 to 40% of the peak stress f_c . Beyond this point, concrete behaves non-linear up to the peak stress with a decreasing stiffness due to micro cracking. When the maximum compressive strength has been reached, the formation of several macro cracks will occur, and the element will exhibit a growing deflection and a reduction in load bearing capacity. This will then lead to the total failure of the element under compression. The reduction of load bearing capacity after the formation of macro cracks leads to a descending branch of the stress-strain curve, which is characteristic for the softening behavior of concrete. Figure 2.1b shows a typical uniaxial compression stress-strain curve.

2.2 Biaxial behavior of plain concrete

Concrete subjected to biaxial loading exhibits a different response than in comparison with uniaxial loading. The biaxial stress states can be divided into three loading combinations, namely: tension-tension, tension-compression, and compression-compression. When a specimen is loaded in tension-tension the behavior is similar to uniaxial loading in both directions and can be modeled as such. For loading in tension-compression, the behavior of reinforced concrete is usually modified after cracking. The main reason for this is that the compressive strength of the concrete is affected by the stress-state in the tensile direction. The maximum compressive stress and strain increase with lateral compressive stress. In the compression-tension state, the compressive strength decreases almost linearly as the applied tensile stress increases. The

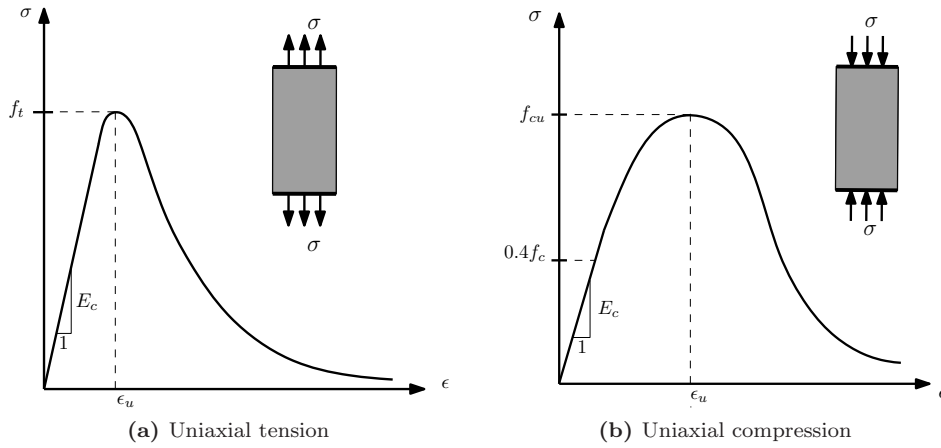


Figure 2.1: Uniaxial behavior of plain concrete

concrete strength in the compression-compression state, is higher by approximately 20% than compared to uniaxial compression. For biaxial tension, the strength is almost independent of the stress ratio.

2.3 Reinforced concrete under axial loading

When reinforced concrete is loaded in tension the linear-elastic behavior is similar as to plain concrete. When the tensile strength is approached, the existing micro cracks in the reinforced concrete will cause the formation of macro cracks. But due to the bond between the concrete and the reinforcement, a gradual redistribution of internal forces occurs. The redistribution of internal forces leads to a stiffer response than in comparison to only the stiffness of the reinforcement. This effect of increasing stiffness is called tension stiffening. An typical stress-strain curve of this phenomenon has been depicted in figure 2.2.

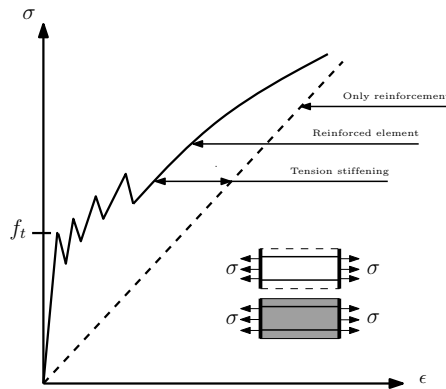


Figure 2.2: Behavior of concrete under uniaxial tensile loading

3. RC beams subjected to shear loading

This chapter will discuss the internal force distribution in shear loaded beams. Furthermore, the shear failure mechanisms as well as the shear transfer mechanisms will be discussed.

3.1 Force distribution

In general, RC beams are reinforced with two types of reinforcement, namely longitudinal bars and transverse stirrups. To illustrate the internal force transmission, the RC beam can be represented as a strut and tie model, as is displayed in figure 3.1. The strut and tie analogy represents the concrete beam as a truss with compression diagonals. In this model, the upper chord consist of concrete loaded in compression, and the lower chord consist of reinforcement loaded in tension. The forces between the upper and lower chord are transmitted via compression diagonals and vertical tension elements. The diagonals consist of concrete loaded in compression, while the stirrups act as the vertical tension elements.

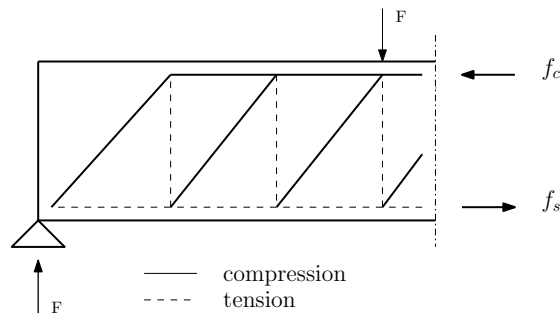


Figure 3.1: Strut and tie model for a concrete beam reinforced with longitudinal and transversal reinforcement

Using the strut and tie analogy, we can derive the conditions for the occurrence of the different failure mechanisms. In a recent workshop [26], four different global shear failure mechanisms were identified which can occur in ultimate limit state analysis. The mechanisms are depicted in figure 3.2 and will be treated in the following sections. There are also a number of local failure mechanisms possible, but these will not be considered in this thesis.

3.2 Shear failure mechanisms

3.2.1 Flexural shear failure

Flexural shear failure is a mechanisms in which flexure induced cracks grow at an angle into the web. To illustrate this type of fracture, we consider a beam that is loaded by a four point bending test. Between the support and the point load, a shear force and a moment is present. The moment decreases linearly over the distance from the point load to the support. If a

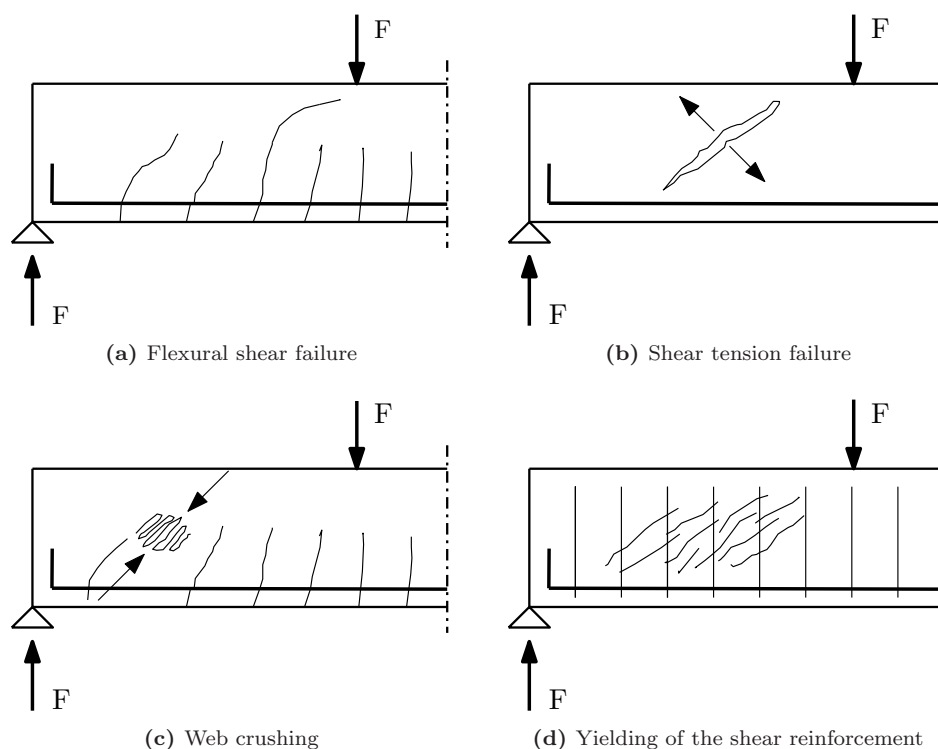


Figure 3.2: Failure mechanisms of reinforced concrete under shear loading

uniform longitudinal reinforcement is applied, which is considered standard, the beam has an increasing bending moment capacity near the support due to the diminished bending moment. Therefore instead of cracks perpendicular to the longitudinal reinforcement, a crack rotation will occur. Increasing the load leads to larger crack and eventually causes the beam to fail due to this mechanisms. In general flexural shear is caused by a standard load situation, with a normal ratio between the flexural and shear stresses. The use of transverse reinforcement such as stirrups will prevent the propagation of cracks into the web.

3.2.2 Shear Tension failure

Shear tension is a mechanisms in which a diagonal crack occurs due to the tension component of the principal stress. When we consider the strut and tie analogy, this failure can be considered as failure of the compression diagonal due to a biaxial tension-compression state. The main crack occurs at a varying angle of approximately 30° to 45° to the longitudinal axis, and is characterized by a sudden (brittle) development into the web of the beam. This means that this type of shear fracture can be considered to be a failure type without warning. In general this type of failure occurs for beam structures that have a high level of shear stress and a relative low level of flexural stress. For example, beam regions near supports are sensitive to this type of fracture.

3.2.3 Web crushing

Web crushing occurs when a structure has a high shear reinforcement ratio and a small amount of web surface. This implies that if a beam is reinforced with a large amount of stirrups, the compression diagonal may fail due to crushing of the concrete, before the stirrups have the possibility of reaching their yield strength. In principle this mechanism is the equivalent of failure of the compression zone in heavily reinforced structures loaded in flexure. There are no typical loading situations where only this type of failure occurs. However, this failure does tend to occur in I-beams with large flanges and small web dimensions.

3.2.4 Yielding of the shear reinforcement

Yielding of the shear reinforcement is a mechanism that is to be expected if the structural design of the beam is correct. In this case the stirrups will yield before failure occurs. This failure will be accompanied by a considerable deformation, implying that the failure mechanism provides warning before reaching the moment of failure. This type of failure has a smeared crack pattern, with a small number of dominating cracks. There are no typical load situations in which only this type of failure occurs. This type of mechanism is dependent on the type of structure and how it has been designed.

3.3 Shear transfer in cracked concrete

The transfer of shear force in cracked reinforced concrete is characterized by a number of complex phenomena [16], consisting of: aggregate interlock, dowel action, axial steel stress, and residual tensile stresses across the crack. These mechanisms are strongly dependent on the state of stress, the opening of the crack, and the restraint conditions.

The shear transfer capacity is also strongly dependent on the interaction between the mentioned transfer mechanisms. When shear stresses arise across a crack surface, a displacement (slip) tangential to the crack face occurs and the crack surfaces tend to separate. The reinforcing bars provide resistance against the separation of this crack face via the dowel mechanism and the axial steel stress. These mechanisms cause a strain in the steel and a decreased bond action, this then permits a crack to increase in width. The amount of reinforcement is therefore of large influence in the constraint of the crack face. The shear transfer mechanisms described are depicted in figure 3.3 and are elaborated on in the following sections.

3.3.1 Aggregate interlock

In normal strength concrete, the strength of the aggregate material will exceed the strength of the cement matrix material. Therefore cracking in concrete will commonly occur through the matrix and the bond zone between the matrix and the aggregate, as is depicted in figure 3.3a. Because the protruding aggregate particles on the crack face are larger than the crack width, the crack plane is considered to be rough. Therefore the crack plane provides resistance against slip, and is

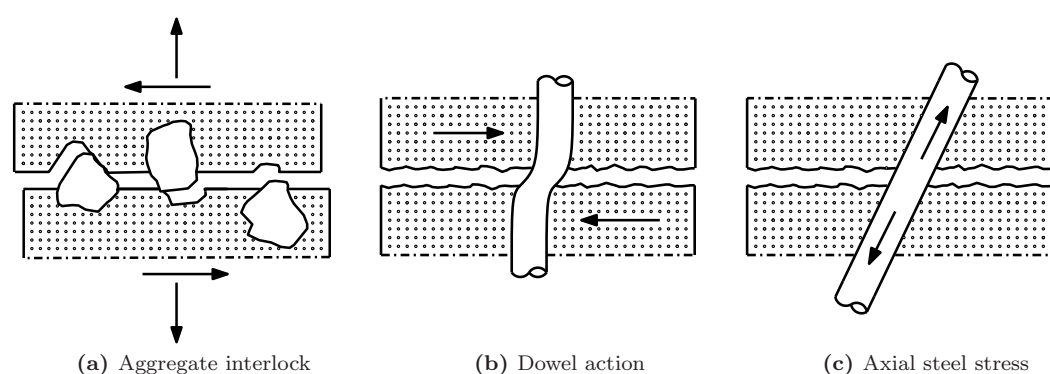


Figure 3.3: Shear transfer Mechanisms in cracked concrete

capable of transmitting shear force. This principle is called aggregate interlock. The magnitude of the aggregate interlock mechanism is dependent on the width of the crack. A larger crack width means a reduction of aggregate interlock because of the decrease of contact area between the aggregate particles. Another parameter that influences the aggregate interlock mechanism is the aggregate size itself, smaller particles will provide a smoother crack plane and therefore less friction. When considering high strength concrete, the aggregate interlock contribution becomes even less, due to smoother crack faces. This is caused by the fact that the crack will not only propagate through the cement matrix, but also through the aggregate particles.

3.3.2 Dowel action

A dowel is a reinforcement bar that is loaded by a transverse force. The mechanism of dowel action is based upon the behavior of the bar and the surrounding concrete. The dowel action consist of two components, namely: bending action, and shear action of the reinforcing bar. The contribution of dowel action to the shear resistance is a function of the amount of concrete cover of the longitudinal bars and the degree to which the vertical displacements of those bars at the inclined crack are restrained by transverse reinforcement.

3.3.3 Axial steel stress

Reinforcing bars generally cross cracks at different angles, this is particularly the case for transverse shear reinforcement. The component of the steel stress normal to the crack plane provides a contribution to the transfer of stresses across a crack. The magnitude of this force is strongly dependent on the amount of reinforcement and the bond properties. In members with shear reinforcement, a large portion of the shear is carried by the shear reinforcement after diagonal cracking has occurs. Next to the contribution to the shear capacity, shear reinforcement also provides a level of restraint against the growth of inclined cracks and thus helps to ensure a more ductile behavior.

3.3.4 Residual stresses

When cracks are formed in concrete, the concrete still has the ability to transfer tensile stresses across the crack face. These so-called residual stresses are present until the crack width becomes too large. This behavior is described by the strain softening diagram as was discussed earlier in section 2.1.

3.3.5 Shear-stress in the compression zone

Shear stresses that are present in the compression zone of the concrete, contribute to the shear resistance in a concrete member. The magnitude of that shear resistance is limited by the depth of the compression zone. Therefore, in a relative slender beams without axial compression, the shear contribution becomes relatively small, due to the minimal height of the compression zone.

4. Numerical modeling of concrete fracture

The following sections will treat different approaches for the modeling of fracture in concrete. A discrete interface formulation, a smeared total strain formulation, and decomposed strain formulation will be discussed. Furthermore, the governing constitutive relations, and their parameters will be discussed.

4.1 Introduction

In order to model the fracturing behavior of reinforced concrete, a large number of different approaches were developed over the last decades [23]. The main subdivision that can be made between the fracture models consists of continuum, discrete and mixed models. Continuum models are developed upon the framework of continuum mechanics, implying that an infinitesimal volume is considered with the material behavior being described by a stress-strain relation. Different fracture models in the continuum approach are: smeared cracking with decomposed or total strain models, plasticity based models, continuum damage models, and other frameworks. In case of modeling cracks in a discrete manner, interface elements with a finite lengths are used, and a relation is established between internal forces and the relative displacement and/or rotations. As a final option, mixed models combine both the continuous and the discontinuous models. The models applied in this thesis will be discussed in the following sections.

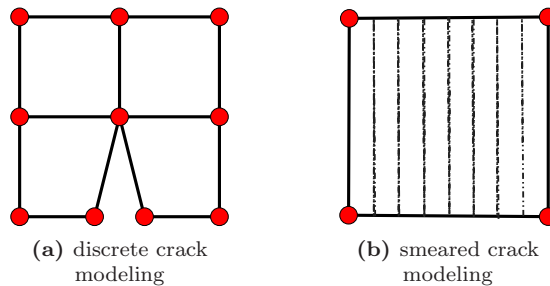


Figure 4.1: Representation of two types of crack modeling

Because the thesis will focus on the behavior of beam elements, rather than plate like elements, the discussed principles are defined in two dimensional coordinate systems. The global system is defined as a orthogonal (x, y) system, and the local system is defined as an orthogonal (n, t) system. In the local system, (n) is the direction normal to the crack face and (t) is the direction tangential to the crack face. Both systems are depicted figure 4.2, with figure 4.2a representing plane stress elements and figure 4.2b representing interface elements.

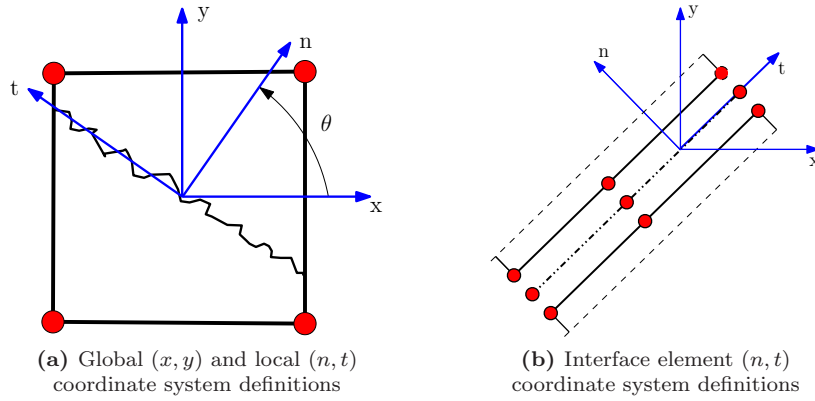


Figure 4.2: Coordinate system definitions

4.2 Discrete crack modeling

Discrete crack modeling creates a discontinuity (i.e. crack) by means of a separation of an element edge, see figure 4.1a. In order to make this separation, the user constructs interface elements at the desired crack location. One of the main drawbacks of this method is the fact that the separation of an element edge does not fit the nature of the finite element because of its discontinuity in nodal connectivity. A second disadvantage, inherent to the modeling of interfaces, is that only predefined crack paths along element edges are possible*. This however, can also be viewed as an advantage. For concrete structures that are characterized by the formation of dominant cracks at known locations, the discrete crack approach can offer a realistic results. Nevertheless, concrete structures are usually characterized by diffused crack patterns, especially in heavy reinforced structures. In such cases the smeared crack approach is often considered to advantageous over the discrete crack approach.

4.2.1 Interface modeling

The discrete crack approach is based on the construction of a interface element between the plane stress elements. In case of a two-dimensional configuration, line interface elements are used. These elements relate the forces acting on the interface to the relative displacement of the two sides of the interface (total relative displacement theory). The forces are defined in the traction vector \mathbf{t} and are defined in the (n, t) direction as:

$$\mathbf{t} = \begin{bmatrix} t_n \\ t_t \end{bmatrix} \quad (4.1)$$

The relative displacement vector $\Delta \mathbf{u}$ is defined as:

$$\Delta \mathbf{u} = \begin{bmatrix} \Delta u_n \\ \Delta u_t \end{bmatrix} \quad (4.2)$$

*This statement is not entirely true. The reason for this is that, discrete crack models exist in which the cracks can grow into an element or where automatic re-meshing procedures are applied. These models however, are not considered in this thesis.

In which Δu_n is the displacement in the normal direction of the crack and Δu_t the displacement in the tangential direction. The linear elastic relation between the vectors is given by:

$$\begin{bmatrix} t_n \\ t_t \end{bmatrix} = \begin{bmatrix} k_n & 0 \\ 0 & k_t \end{bmatrix} \begin{bmatrix} \Delta u_n \\ \Delta u_t \end{bmatrix} \quad (4.3)$$

The diagonal terms k_n and k_t are given high initial dummy stiffness, in order to recreate the actual rigid connection between the nodes of the plane stress elements. The behavior of the interface elements upon cracking is defined by two functions:

$$t_n = f_n(\Delta u_n) \quad (4.4)$$

$$t_t = f_t(\Delta u_t) \quad (4.5)$$

When equations (4.4) and (4.5) are linearized by means of the Jacobian, a tangential stiffness matrix is formed, relating the displacement vector with the force vector as:

$$\begin{bmatrix} dt_n \\ dt_t \end{bmatrix} = \begin{bmatrix} \frac{\partial f_n}{\partial \Delta u_n} & 0 \\ 0 & \frac{\partial f_t}{\partial \Delta u_t} \end{bmatrix} \begin{bmatrix} d\Delta u_n \\ d\Delta u_t \end{bmatrix} \quad (4.6)$$

The basis for the two functions represented in equations (4.4) and (4.5), are the tension softening relations, these will be discussed in section 4.4.

4.2.2 Crack dilatancy

In the previous section, a constitutive relation was presented (equation (4.6)) that describes the concrete behavior upon crack formation. In this relation, there is no coupling between the normal and tangential component of the traction vector \mathbf{t} . For a more sophisticated analysis, non diagonal terms can be introduced to couple both traction components. The reason for this coupling is to model the sliding (shear-slip) across a crack face. With the modeling of this shear-slip, an aggregate interlock formulation can be constructed.

There are a number of constitutive models available for this type of analysis, these models are based on two main configurations: an empirical formulation or a physical formulation. Both types of models define a non-linear relation as:

$$t_n = f_n(\Delta u_n, \Delta u_t) \quad (4.7)$$

$$t_t = f_t(\Delta u_n, \Delta u_t) \quad (4.8)$$

When equations (4.7) and (4.8) are linearized the following stiffness matrix \mathbf{K} is formed:

$$\mathbf{K} = \begin{bmatrix} \frac{\partial f_n}{\partial \Delta u_n} & \frac{\partial f_n}{\partial \Delta u_t} \\ \frac{\partial f_t}{\partial \Delta u_n} & \frac{\partial f_t}{\partial \Delta u_t} \end{bmatrix} \quad (4.9)$$

The stiffness matrix \mathbf{K} in equation (4.9) shows the non-diagonal terms that couples the crack normal traction with the tangential traction component

4.3 Smearred crack modeling

The need for a crack model that offers automatic generation of cracks and corresponding behavior, without a redefinition of the finite element topology, has lead to extensive use of the smeared crack approach. Rather than representing a single crack, the smeared crack model represents an area of the concrete that is cracked, as is illustrated in figure 4.1b. Modeling the crack by a representative area (i.e. an element area) was first developed in the fictitious crack model of Hillerborg [12], after which Bažant & Oh [2] extended it to finite element modeling by developing the crack band model. The fracture process in a smeared crack model is treated as a reduction of the material stiffness in the direction of the principal stress over the representative area. This reduction is related to the tension softening behavior of the concrete. Crack initiation occurs when the principal stress or a combination of principal stresses exceeds the tensile strength.

Within the context of the smeared crack models, two different stress-strain representations were developed, namely: a total strain based model and the decomposed strain model. A constitutive model based upon total strain describes the stress as a function of the strain, this means that the stresses are evaluated in the directions that are given by the crack directions. The decomposed strain model, represents the total strain as the summation of the elastic strain and the crack strain. with the latter strain made up out of several crack strains components, this is however not a requirement. The advantage of the strain decomposition is that other non-linear phenomena such as creep and shrinkage, can also be included.

4.3.1 Smearred crack principle

Before elaborating on the fixed, fixed multidirectional, and rotating smeared crack models, the basis for the constitutive models of the respective models is outlined. The models are based on the assumption that the constitutive relations are evaluated in a rotated, local coordinate system. This coordinate system is defined by the angle for which the crack is initiated, see figure 4.2a.

Concrete is initially represented as a linear elastic isotropic material, in which the relation between the stresses and strains are defined as:

$$\begin{bmatrix} \sigma_{nn} \\ \sigma_{tt} \\ \sigma_{nt} \end{bmatrix} = \frac{E}{1-\nu^2} \begin{bmatrix} 1 & \nu & 0 \\ \nu & 1 & 0 \\ 0 & 0 & \frac{(1-\nu)}{2} \end{bmatrix} \begin{bmatrix} \varepsilon_{nn} \\ \varepsilon_{tt} \\ \gamma_{nt} \end{bmatrix} \quad (4.10)$$

With E denoting the Young's modulus and ν the Poisson's ratio. When the major principal stress exceeds the tensile strength of the concrete or, in more general terms, when the combination of principal stresses violates the cut off criterion, a crack is initiated perpendicular to the direction of the principal stress. Upon this violation, A orthotropic relation is substituted for the initial

isotropic stress strain relation. The orthotropic relations is expressed through the secant stiffness matrix \mathbf{D}_{sec}^{nt} , which is defined as:

$$\begin{bmatrix} \sigma_{nn} \\ \sigma_{tt} \\ \sigma_{nt} \end{bmatrix} = \begin{bmatrix} \frac{\mu E}{1 - \nu^2 \mu} & \frac{\nu \mu E}{1 - \nu^2 \mu} & 0 \\ \frac{\nu \mu E}{1 - \nu^2 \mu} & \frac{\mu E}{1 - \nu^2 \mu} & 0 \\ 0 & 0 & \frac{\beta E}{2 + 2\nu} \end{bmatrix} \begin{bmatrix} \epsilon_{nn} \\ \epsilon_{tt} \\ \gamma_{nt} \end{bmatrix} \quad (4.11)$$

in which μ (mode I reduction) and β (mode II reduction) are related via the tension softening curve to the secant stiffness parameter.

4.3.2 Fixed total strain model

In a fixed smeared crack model, the crack is fixed upon initiation. The consequence of fixing the crack direction implies that upon rotating of the principal strain direction, a shear stress is generated across the crack face to ensure equilibrium. The consequence of this shear stress, is that a shear stiffness needs to be defined. Early attempts modeled the cracked concrete with a shear stiffness of zero, this however, resulted in number of numerical difficulties. Therefore a shear stiffness factor for cracked concrete was introduced: βG with $0 < \beta < 1$. This factor is called the shear retention factor and could be interpreted as the modeling of aggregate interlock. Most researchers adopt a constant shear retention factor, but there has been some use of a crack strain dependent retention factor.

To elaborate on the numerical algorithms behind the fixed crack model, the formulation of the total strain model is firstly discussed. The constitutive model of the total strain model is developed on the formulations of the Modified Compression Field Theory, originally proposed by Vecchio & Collins [24]. The basic concept of the total strain models is that the stress is evaluated in the directions that are given by the crack direction. The update of the strain increment in the total strain models is defined as:

$$\boldsymbol{\epsilon}_{xy} = \boldsymbol{\epsilon}_{xy} + \Delta \boldsymbol{\epsilon} \quad (4.12)$$

The local strain vector $\boldsymbol{\epsilon}_{ns}$ is related to the global strain vector $\boldsymbol{\epsilon}_{xy}$ through:

$$\boldsymbol{\epsilon}_{ns} = \mathbf{T}_{\epsilon}^{(t\theta)} \boldsymbol{\epsilon}_{xy} \quad (4.13)$$

And the local stress vector $\boldsymbol{\sigma}_{ns}$ is related to the global strain vector $\boldsymbol{\sigma}_{xy}$ in a similar manner:

$$\boldsymbol{\sigma}_{ns} = \mathbf{T}_{\sigma}^{(t\theta)} \boldsymbol{\sigma}_{xy} \quad (4.14)$$

In both formulations, $\mathbf{T}^{(t\theta)}$ represents the transformation matrix with angle θ at time t . In case of the fixed crack model, the rotation matrix is formed only once upon crack initiation. In case of the rotating crack model, the rotation matrix is constantly updated. To provide a general framework for the elaboration of the total strain model, the following derivations will implicitly consider the angle and the moment of rotation without using the respective notations.

The transformation matrix $\mathbf{T}_{\sigma,\epsilon}$ defines the rotation between the global (x, y) and local (n, t) coordinate systems. Given the angle θ the strain transformation matrix is given by:

$$\mathbf{T}_{\sigma,\epsilon} = \begin{bmatrix} \cos^2\theta & \sin^2\theta & \sin\theta\cos\theta \\ \sin^2\theta & \cos^2\theta & -\sin\theta\cos\theta \\ -2\sin\theta\cos\theta & 2\sin\theta\cos\theta & \cos^2\theta - \sin^2\theta \end{bmatrix} \quad (4.15)$$

The stress vector $\boldsymbol{\sigma}_{ns}$ in the local coordinate system is given by the general relation:

$$\boldsymbol{\sigma}_{ns} = \mathbf{D}_{ns}^s \boldsymbol{\epsilon}_{ns} \quad (4.16)$$

Which can also be defined in the global coordinate system by substituting equation 4.13:

$$\boldsymbol{\sigma}_{ns} = \mathbf{D}_{ns}^s \mathbf{T}_\epsilon \boldsymbol{\epsilon}_{xy} \quad (4.17)$$

Upon substituting equation 4.14, the relation between the global stress vector $\boldsymbol{\sigma}_{xy}$ and the global strain vector $\boldsymbol{\epsilon}_{xy}$ is obtained:

$$\boldsymbol{\sigma}_{xy} = \mathbf{T}_\sigma^{-1} \mathbf{D}_{ns}^s \mathbf{T}_\epsilon \boldsymbol{\epsilon}_{xy} \quad (4.18)$$

In which the matrix \mathbf{D}_{ns}^s represent the secant stiffness matrix of equation (4.11).

4.3.3 Rotating total strain crack model

A number of problems are related to the fixed crack model, which are the consequence of stress build up on the crack face. This build up of stress may lead to over-stiff response and un-realistic results [19]. The rotating crack model does not suffer from stress build-up because of the constant alignment of the principal strain directions with the crack direction.

The underlying smeared crack formulation of this model is essentially not different from the fixed crack model. In the rotating model, a crack is also formed to the normal of the principal stress, when a principal stress criterion is violated. However, in this model the crack directions are constantly updated to rotate with the principal strain directions during the loading process. Although this approach may seem physically incorrect, (because cracks in concrete cannot rotate, only principal directions can) the model has proven to be successful in the modeling of reinforced concrete. Also, there is no need for a shear retention factor, which simplifies the numerical implementation and provides more practicality for the user.

The rotating crack model is formulated in the principal strain directions. The reason for this is that, similar to the fixed model, the rotating model is in this case also based on the total strain formulation. This implies that the stress is evaluated in the directions that are given by the crack direction. And because the crack directions are kept orthogonal to the principal directions, the formulation can be given in the principal directions. This will facilitate with the definition of the co-axiality principle.

The incremental form of the constitutive relation between the principal stress $\Delta\sigma_{12}$ and principal strain $\Delta\epsilon_{12}$ is therefore defined as:

$$\begin{bmatrix} \Delta\sigma_1 \\ \Delta\sigma_2 \end{bmatrix} = \begin{bmatrix} \frac{\partial\sigma_1}{\partial\epsilon_1} & \frac{\partial\sigma_1}{\partial\epsilon_2} \\ \frac{\partial\sigma_2}{\partial\epsilon_1} & \frac{\partial\sigma_2}{\partial\epsilon_2} \end{bmatrix} \begin{bmatrix} \Delta\epsilon_1 \\ \Delta\epsilon_2 \end{bmatrix} \quad (4.19)$$

At the moment of crack initiation, both the shear stress σ_{xy} and shear strain γ_{xy} parallel to the cracks are zero. But after crack formation, a shear strain will occur on the surface of the crack. Due to this shear strain, the subsequent principal strain direction rotates from the previous principal direction. This rotation can be formulated using Mohr's circle with the definitions of the principal stresses and strains:

$$\theta_\sigma = \frac{1}{2} \arctan \frac{2\Delta\tau_{12}}{\sigma_1 - \sigma_2} \quad (4.20)$$

$$\theta_\epsilon = \frac{1}{2} \arctan \frac{\Delta\gamma_{12}}{\epsilon_1 - \epsilon_2} \quad (4.21)$$

For the rotating crack model it is required that the principal direction of the stresses and the strains coincide with each other to preserve co-axiality. This implies that $\theta_\sigma = \theta_\epsilon$. Evaluating this formulation leads to:

$$\Delta\tau_{12} = \frac{\sigma_1 - \sigma_2}{2(\epsilon_1 - \epsilon_2)} \Delta\gamma_{12} \quad (4.22)$$

In equation (4.22) the shear modulus G can be identified as:

$$G = \frac{\sigma_1 - \sigma_2}{2(\epsilon_1 - \epsilon_2)} \quad (4.23)$$

Combining (4.19) and (4.23) leads to the total formulation of the tangential stress-strain law for the rotating crack model:

$$\begin{bmatrix} d\sigma_1 \\ d\sigma_2 \\ d\sigma_{12} \end{bmatrix} = \begin{bmatrix} \frac{\partial\sigma_1}{\partial\epsilon_1} & \frac{\partial\sigma_1}{\partial\epsilon_2} & 0 \\ \frac{\partial\sigma_2}{\partial\epsilon_1} & \frac{\partial\sigma_2}{\partial\epsilon_2} & 0 \\ 0 & 0 & \frac{\sigma_1 - \sigma_2}{2(\epsilon_1 - \epsilon_2)} \end{bmatrix} \begin{bmatrix} d\epsilon_1 \\ d\epsilon_2 \\ d\gamma_{12} \end{bmatrix} \quad (4.24)$$

The tangential stress-strain law as presented in equation (4.24) implies that upon crack formation a negative pivot will occur in the tangential stiffness matrix. This negative pivot can have the consequence that the convergence of the iterative procedure can be lost. To avoid the loss of convergence a secant-stiffness matrix \mathbf{D}_{sec} can also be constructed in the principal direction in the following manner:

$$\mathbf{D}_{sec} = \begin{bmatrix} E_1 & 0 & 0 \\ 0 & E_2 & 0 \\ 0 & 0 & G \end{bmatrix} \quad (4.25)$$

The secant stiffness matrix will be used throughout the numerical analysis in this thesis.

4.3.4 Fixed multidirectional crack model

The fixed multidirectional crack models is a refined version of the fixed crack model. The aim of this model is to improve the simulation of the change in principal strain direction. The basic concept is the same as the fixed crack model, however, in the multidirectional model, new cracks are allowed to develop if the principal stress criterion is again violated in a different direction. The difference between the standard fixed model is that the crack do not necessarily have to be orthogonal, but can be formed under different angles that are controlled via a threshold angle. The implication of allowing cracks to form under different angles is that more than two cracks can be described within a single integration point.

In order to model multiple cracks, the total strain formulation cannot be used. The fixed multidirectional model will therefore be described using the decomposed strain model [19, 5]. The basic feature behind decomposed crack modeling is to decompose the total strain into an elastic and crack strain:

$$\epsilon = \epsilon^e + \epsilon^{cr} \quad (4.26)$$

Because we are now modeling multiple cracks, the crack strains are assembled in a vector in the following manner:

$$\Delta \mathbf{e}^{cr} = \langle \Delta e_1^{cr}, \Delta e_2^{cr}, \dots, \Delta e_i^{cr}, \dots, \Delta e_n^{cr} \rangle^T \quad (4.27)$$

The crack strains in (4.27) are composed out of two components:

$$\Delta e_i^{cr} = \langle \Delta \epsilon_{nn;i}^{cr}, \Delta \gamma_{nt;i}^{cr} \rangle^T \quad (4.28)$$

With the subscript i representing the individual crack. To relate the crack strain to the global strain the transformation matrix \mathbf{N} is applied in the following manner:

$$\Delta \epsilon^{cr} = \mathbf{N} \Delta \mathbf{e}^{cr} \quad (4.29)$$

Since this model consider a number of non-orthogonal crack, the transformation matrix \mathbf{N} also needs to be defined per crack strain.

$$\mathbf{N} = \langle \mathbf{N}_1, \mathbf{N}_2, \dots, \mathbf{N}_i, \dots, \mathbf{N}_n \rangle^T \quad (4.30)$$

In using the similar principles as the crack strain formulation the crack stresses per crack are also assembled in a vector:

$$\begin{aligned} \Delta \mathbf{s}^{cr} &= \langle \Delta s_1^{cr}, \Delta s_2^{cr}, \dots, \Delta s_i^{cr}, \dots, \Delta s_n^{cr} \rangle^T & \text{with} & \quad \Delta s_i^{cr} = \langle \Delta \sigma_{nn;i}^{cr}, \Delta \sigma_{nt;i}^{cr} \rangle^T \\ \Delta \boldsymbol{\sigma}^{cr} &= \mathbf{N} \Delta \mathbf{s}^{cr} \end{aligned} \quad (4.31)$$

The elastic stress-strain relationship is defined as:

$$\Delta \boldsymbol{\sigma} = \mathbf{D}^e \Delta \boldsymbol{\epsilon} \quad (4.32)$$

And the elastic stress-strain relationship is defined as:

$$\Delta s_i^{cr} = \mathbf{D}_i^{cr} \Delta \epsilon_i^{cr} \quad (4.33)$$

The matrix in (4.33) is a relation between the crack stress and crack strain. In this matrix the normal and shear stresses are un-coupled, therefore, the crack stresses are only governed by the corresponding crack strains. The un-coupling implies that the matrix only has non-zero term on the diagonals. These terms are D^I and D^{II} , and represent the tension softening diagram and the shear retention factor.

At this point, we have established the constitutive relations in the local coordinate systems for the crack stresses and strains. The constitutive relations between the stresses and the strains in the global coordinate system, can be determined from the original strain decomposition in (4.26). This results in the following relation for an arbitrary direction:

$$\Delta \boldsymbol{\sigma} = \mathbf{D}^e (\Delta \boldsymbol{\epsilon} - \Delta \boldsymbol{\epsilon}^{cr}) \quad (4.34)$$

Upon substitution of the relation for the elastic and crack strain, and multiplying by \mathbf{N}^T we end up with the following formulation:

$$\Delta \boldsymbol{\sigma} = [\mathbf{D}^e - \mathbf{D}^e \mathbf{N} [\mathbf{D}^{cr} + \mathbf{N}^T \mathbf{D}^e \mathbf{N}]^{-1} \mathbf{N}^T \mathbf{D}^e] \Delta \boldsymbol{\epsilon} \quad (4.35)$$

After the first crack, another crack is allowed to form if the tensile strength is again violated by the major principal stress, and if the angle between the existing crack and the direction of the major principal stress exceeds a certain angle. Usually, this threshold angle is set at a value of 60° , which implies a maximum number of crack which are formed to six [6].

4.4 Tension softening

The shape of the tension softening curve determines the behavior of the concrete upon cracking. Although many experiments have been performed on determining the exact shape of the curve, there is no consensus on the application of one specific curve. The used FE code offers three different types of softening curve, namely: linear, bi-linear, and non-linear. In order to define the strain softening behavior of concrete in a smeared crack formulation, three parameters need

to be defined, namely: (1) tensile strength of concrete, (2) the fracture energy, and (3) shape of the softening diagram.

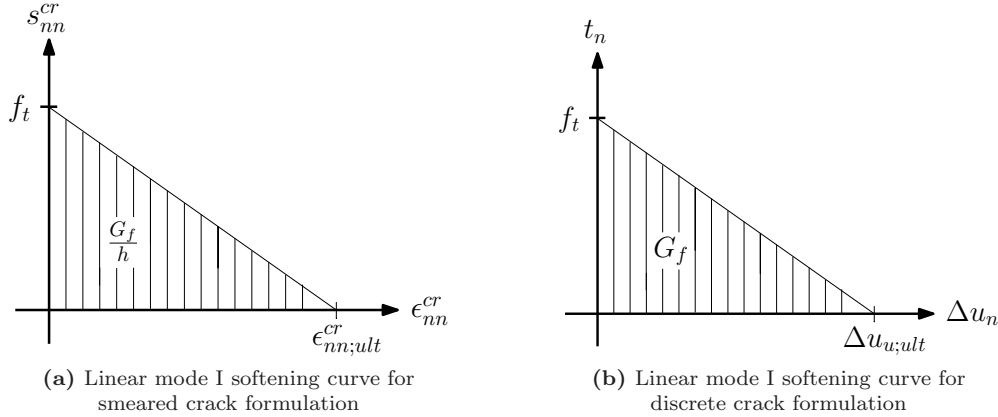


Figure 4.3: Softening diagrams for different crack representations

In a smeared crack formulation the mode I softening diagram is a function of the crack strain ϵ_{nn}^{cr} and the crack stress s_{nn}^{cr} , see figure 4.5. In case of a discrete crack formulation the mode I softening is a function of the relative displacement Δu and traction vector t , see figure 4.3b.

The area under the softening curve divided by the crack bandwidth, and represents the fracture energy G_f . This quantity defines the total energy release when an element is fully cracked, with fully cracked implying that either the relative displacement Δu or ϵ_{nn}^{cr} is larger than the ultimate value of these respective quantities*. The area under the softening curve can be integrated, this leads to the following expression regarding the ultimate value in case of a linear softening diagram. For a smeared crack formulation this is:

$$\epsilon_{nn;ult}^{cr} = \frac{2G_f}{hf_t} \quad (4.36)$$

For a discrete crack formulation this is:

$$\Delta u_{ult} = \frac{2G_f}{f_t} \quad (4.37)$$

The set of parameters that are present in equation (4.36) and (4.37) are defined by the user. The crack bandwidth h is defined by a representative dimension of the element size. The bandwidth depends in general on the chosen element type, element size and integration scheme. The fracture energy should be released over this width in order to obtain results that are objective with respect to mesh refinements.

4.5 Shear retention

Defining a shear retention factor is necessary in case of the fixed crack model. The reason for this lies within the assumption of a fixed crack. Upon the moment of crack formation, and therefore

*This definition is only valid for linear softening. Exponential softening function does not contain a ultimate crack strain because the function goes to infinity when approaching zero stress. When the term ultimate crack strain is used, it will be implied that this is the ultimate crack strain as is calculated with a linear softening diagram

crack fixation, the principal direction tend to rotate due to an unbalance caused by the reduced mode I stiffness of the crack. To ensure equilibrium a shear stress on the face of the crack is generated. The quantity of this shear force can be modeled in a number of different approaches: constant shear retention (figure 4.4a), variable shear retention based on shear strain (4.4b), and a full shear stress-strain relation (not depicted).

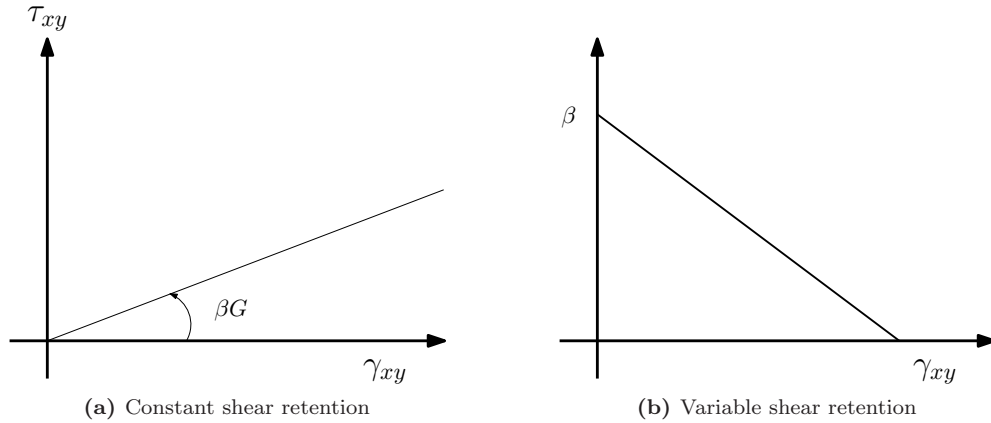


Figure 4.4: Shear retention formulations for fixed crack model

Defining a shear stiffness for the shear stress on the crack face can be interpreted a modeling aggregate interlock. However, a disadvantage of a constant and variable shear retention factor is that it does not accurately represent shear dilation and the dependence on the cracks shear on the crack opening displacement. The shear formulation in the fixed crack models are therefore limited in its representation of the physical reality.

4.6 Unloading and Reloading

The unloading and reloading behavior of cracks in concrete is a complicated phenomenon and is characterized by hysteresis loops [3]. The correct modeling of the unloading-reloading path is of particular importance in case of cyclic loading, where the unloading-reloading model dominates the behavior [10]. However, in case of non-linear analysis of shear critical RC beams under proportional loading, the unloading and reloading only occurs locally and is therefore less dominant. However, selecting the correct structural path is still of importance.

The unloading-reloading of cracks can occur through a two main approaches, namely: an elastic or secant approach (see figure 4.5). The elastic approach consists of using the elastic stiffness to return to the unloaded state. The result of which, is that a part of the strain remains. This implies that the crack does not actually close upon load reversal. The second approach consists of unloading through a secant relation to the origin. This approach has proven to be successful in the non-linear analysis of concrete structures and will be applied through-out the thesis.

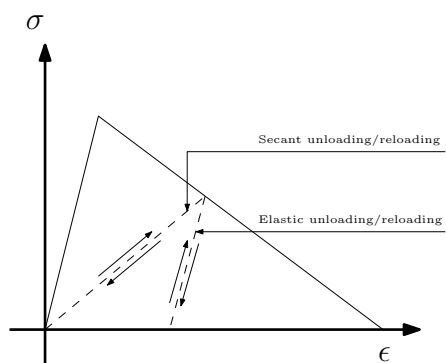


Figure 4.5: Unloading and reloading principles

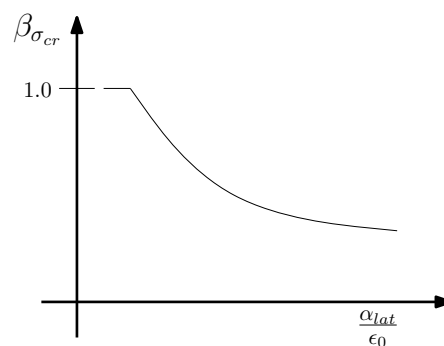


Figure 4.6: Reduction compressive strength

4.7 Compressive response of cracked reinforced concrete

Reinforced concrete that is loaded in compression and lateral crack formation due to tension, exhibits a lower strength and stiffness than uniaxially compression loaded concrete [25]. This compressive softening has a significant influence on the strength, ductility and load-deformation response of concrete. To accurately model this phenomenon a reduction factor $\beta_{\sigma_{cr}}$ is applied. This value of this reduction is related to the amount of damage that occurs in the lateral direction, see figure 4.6. This damage is monitored by the internal variables governing the tensile damage in the lateral directions, $\alpha_{l,1}$ and $\alpha_{l,2}$. An average lateral damage α_{lat} is computed and related to the initial strain ϵ_0 to represent the damage that has occurred.

5. Solution techniques NLFEA

The following sections will briefly discuss the principles behind the incremental-iterative method. These principles consist of: imposing the load on the FE model, iteration methods, convergence criteria, and acceleration techniques.

5.1 The incremental-iterative procedure

The solution procedure of a non-linear finite element analysis is based on an incremental-iterative formulation. This implies that the external load is divided into a number of increments, which are then imposed on the finite element model. Within each increment an iterative procedure is applied to obtain the equilibrium solution, hence the name incremental-iterative procedure. The application of load-increments with internal iterations instead of applying the entire load at once, is based on the following reasons:

- The algebraic equations that arise from the discretization of a non-linear continuum model are non-linear, these equations therefore necessitate an iterative procedure for its solution.
- Experiments show that most structural materials are path dependent, meaning that different levels of stress can be obtained, depending on the strain path that is followed.
- To ensure the convergence of the iterative procedure, the size of the load or displacement increment needs to be constrained. Otherwise, convergence will be difficult to obtain.

5.2 Load and displacement control

In case of an incremental-iterative analysis, there are two methods of imposing an external load and achieving convergence within each load step. The first method consists of applying a load divided into a number of increments, i.e. load control. The second method is based on applying a prescribed displacement divided into increments, i.e. displacement control. The choice for either of these methods can, in some cases, be determined by the nature of the problem. For example, with creep problems, the load will be prescribed and not the displacements. However, when there is no direct preference for either method from a physical point of view, the displacement control is usually applied. There are two main reasons for this choice, namely: (1) the tangential stiffness matrix is better conditioned for displacement control than for load control and (2) in using load control, the tangential stiffness matrix becomes singular at limit points in the load-deflection diagram.

To elaborate on the first statement, we consider the main distinction between load and displacement control, which is that load control procedure requires the inversion (LDU decomposition) of the stiffness matrix, while the displacement control procedure, only requires the inversion of

a reduced stiffness matrix. For symmetric matrices, which is very common for structural computations, it is possible to show that the spectral radius the reduced stiffness matrix is always smaller or at least equal to the full stiffness matrix [6]. This leads to the conclusion that a better conditioned tangential stiffness matrix leads to faster convergence, and since displacement control involves iterations with a better conditioned tangential stiffness matrix, the result is a faster converging iteration process.

The second reason basis itself on the fact that displacement control does not become singular at a local or global peak in the load-displacement curve. Singularities can however occur if load control is applied. The main reason for this is not the fact that the matrix is ill-conditioned but more due to finding an intersection between the imposed load and the load-displacement path at peak loads.

Although load-control has two major disadvantages over displacement control, it does have the advantage of overcoming a snap-back behavior in the load-displacement curve when using an arc-length control. This is not possible when using a displacement controlled procedure.

5.3 Iterative procedures

Two main classes of iteration methods are available for iterative part of the incremental-iterative procedure. The first class assumes that the stiffness matrix varies so slowly, that it can be set-up only once for the initial iteration and can be used throughout all of the subsequent iterations. These iteration methods are known as the linear and constant stiffness method. Because of the strong non-linear response of concrete, it can be expected that the stiffness varies greatly upon crack formations. Therefore, the stiffness matrix of these methods deviates considerably from the actual stiffness of the RC beam. The consequence being, that convergence will be very slow or will never occur at all. These methods are therefore considered to be unsuitable for non-linear finite element analysis involving concrete cracking.

The second class of iteration methods are based on a tangential stiffness matrix with or without subsequent updates to this tangential stiffness, the so-called Newton class iteration methods. The first one of these methods is the Regular Newton-Raphson method (rN-R), the tangential stiffness matrix \mathbf{K}_t is formulated as:

$$\mathbf{K}_t = \frac{\partial \mathbf{g}}{\partial \Delta \mathbf{u}} \quad (5.1)$$

In which \mathbf{g} represent the out-of-balance force vector and $\Delta \mathbf{u}$ the incremental displacement vector. The rN-R method sets-up a new tangential stiffness matrix with every iteration, this theoretically means that the convergence of the numerical error is quadratic. However, the rN-R suffers from convergence problems due to sudden non-linearities, such as local unloading from an inelastic state to an elastic state, that can arise during the increment.

Next to the rN-R the modified Newton-Raphson (mN-R) is frequently used for the non-linear analysis of structural problems. The stiffness matrix of mN-R is also based on the tangential stiffness as was formulated in equation (5.1). However, when comparing both methods, the

mN-R has the advantage that it is un-sensitive to non-linearities that arise during the loading increment. This is caused by the fact that the tangential stiffness matrix \mathbf{K}_t is only formed once per increment for the first iteration.

Next to both the Newton-Raphson iteration methods, the Secant-Newton (S-N) method is available. In the S-N method, the tangential stiffness matrix is approximated by a secant formulation. These methods replace most of the Newton-Raphson iterations with a cheaper update to the stiffness matrix, sacrificing convergence performance but making the average equilibrium iteration less expensive. In solving the non-linear equations, a secant method will perform the first iteration with the tangent formulation of (5.1). The following updates of the stiffness matrix will be based on the Secant Newton formulation. In this thesis the S-N iteration methods used consisted of the BFGS method, with the BFGS method defining its updated stiffness matrix inverse \mathbf{K}_{i+1}^{-1} as:

$$\mathbf{K}_{i+1}^{-1} = \left(\mathbf{I} + \frac{\delta \mathbf{u}_i \delta \mathbf{g}_i^T}{\delta \mathbf{u}_i^T \delta \mathbf{g}_i} \right) \mathbf{K}_i^{-1} \left(\mathbf{I} - \frac{\delta \mathbf{u}_i \delta \mathbf{g}_i^T}{\delta \mathbf{u}_i^T \delta \mathbf{g}_i} \right) + \frac{\delta \mathbf{u}_i \delta \mathbf{u}_i^T}{\delta \mathbf{u}_i^T \delta \mathbf{g}_i} \quad (5.2)$$

In which $\delta \mathbf{u}_i$ in the iterative part of the incremental displacement vector, \mathbf{g}_i the out of balance force vector for the particular iteration, and \mathbf{K}_i the previously obtained stiffness matrix.

5.4 Convergence criteria

In order to determine whether the iterative procedure has reached an equilibrium state, a criterium is needed to define the quantity of this state. Such a criterion generally formulates that when a norm of a certain quantity, e.g. force or displacement is within a certain user set boundary, the iteration process is considered to be converged. The most strict global criterion is the force norm. The force norm defines convergence when the current norm of the out-of-balance force vector \mathbf{g}_i has a value of less than a user-defined percentage of the original norm of the out-of-balance force vector \mathbf{g}_0 , as was determined at the start of the increment. The force norm is formulated as:

$$\frac{\sqrt{\mathbf{g}_i^T \mathbf{g}_i}}{\sqrt{\mathbf{g}_0^T \mathbf{g}_0}} < \epsilon \quad (5.3)$$

with ϵ being the measured quantity for defining convergence. Next to the force norm, the displacement norm can be used. This norm bases itself on the same principles as the force norm, but the measured quantity consist of the incremental displacement vector $\delta \mathbf{u}_i$:

$$\frac{\sqrt{\delta \mathbf{u}_i^T \delta \mathbf{u}_i}}{\sqrt{\Delta \mathbf{u}_0^T \Delta \mathbf{u}_0}} < \epsilon \quad (5.4)$$

As a final option the energy norm can be applied, which combines the incremental displacement vector $\delta \mathbf{u}_i$ with the internal force vector $\mathbf{f}_{int;i}$:

$$\left| \frac{\delta \mathbf{u}_i^T (\mathbf{f}_{int;i+1} + \mathbf{f}_{int;i})}{\Delta \mathbf{u}_0^T (\mathbf{f}_{int;1} + \mathbf{f}_{int;0})} \right| < \epsilon \quad (5.5)$$

As mentioned before, the force norm can be considered to be the most strict norm. The reason for this is that the displacement norm as well as the energy norm are less strict. This difference in strictness is caused by the presence of the incremental displacement vector $\delta \mathbf{u}_i$ in both norms which can indicate convergence more easily. The reason behind this, is that the incremental displacement vector represents the iterative change in displacement as calculated by the iterative procedure. When this value becomes small, for example due to a ill-conditioned stiffness matrix, the norm could indicate an untrue equilibrium.

The value of the convergence tolerance ϵ must be selected carefully, a too loose convergence norm may lead to inaccurate and unreliable results. On the other hand a too strict norm will lead to excessive computations, without improving on the results. The significance of the norm value is discussed in section 6.4.2.

5.5 Acceleration and arc length techniques

To accelerate and improve the convergence rate of the iterative procedures, a number of accelerating and arc length algorithms have been developed. These techniques will be shortly discussed in the following sections.

5.5.1 Arc length control

The arc-length technique has been developed for successfully finding convergence in case of snap-through and snap-back behavior in the load-displacement behavior of structures. The arc-length techniques uses a load factor $\Delta \lambda_i$ to constrain the incremental displacement vector $\delta \mathbf{u}_i$ by adapting the size of the load-increment. This is formulated in the following manner:

$$\delta \mathbf{u}_i = \mathbf{K}_i^{-1} \left(\Delta \lambda_i \hat{\mathbf{f}} + \mathbf{f}_{int}^t - \mathbf{f}_{int,i} \right) \quad (5.6)$$

Subsequently, the incremental displacement vector can be split into two parts:

$$\delta \mathbf{u}_i^I = \mathbf{K}_i^{-1} \left(\mathbf{f}_{int}^t - \mathbf{f}_{int,i} \right) \quad \text{and} \quad \delta \mathbf{u}_i^{II} = \mathbf{K}_i^{-1} \hat{\mathbf{f}} \quad (5.7)$$

The total iterative increment is then derived from:

$$\delta \mathbf{u}_i = \delta \mathbf{u}_i^I + \Delta \lambda_i \delta \mathbf{u}_i^{II} \quad (5.8)$$

With the superscript I denoting the contribution from the iterative procedure and superscript II denoting the contribution of the constraint equation. Two different formulations are available, in the used FE code, which define the load factor $\Delta \lambda_i$, namely the spherical path arc length method and the updated normal plane method. For further elaboration the reader is referred to [9, 13].

5.5.2 Line search algorithm

The previously described iteration methods are based on an initial prediction. It is not uncommon for this prediction to be "too far" from the actual equilibrium situation because of a strong non-linear response. In these cases it is therefore difficult to obtain convergence at all. To alleviate these problems the line search algorithm was introduced. The line search algorithm scales the incremental displacement vector $\delta \mathbf{u}_{i+1}$, obtained through the iterative method, to increase the convergence rate. The incremental displacement vector $\Delta \mathbf{u}_{i+1}$ with line searches is formulated as:

$$\Delta \mathbf{u}_{i+1} = \Delta \mathbf{u}_i + \eta \delta \mathbf{u}_{i+1} \quad (5.9)$$

The scale factor η is obtained through minimization of the energy potential Π as following:

$$s(\eta) = \frac{\partial \Pi}{\partial \eta} = \mathbf{g}(\eta)^T \delta \mathbf{u} = 0 \quad (5.10)$$

The solution of $s(\eta) = 0$ can be calculated by determining s at various values of η . The first two values are readily derived from the original iteration process. With these values the search direction can be obtained, and further calculations can be made. The line search algorithm usually does not continue until a value of $s = 0$ is found but terminates the line search if the absolute value is less than Ψ times the value $s(0)$. For further elaboration the reader is referred to [8, 13].

6. Benchmark: Beam A

The first benchmark study will be performed on a beam that was part of a recent workshop on the shear strength of concrete beams. The workshop was initiated by the Dutch Ministry of Transport, Public Works and Water management, and was organized by the Dutch Organization for Applied Scientific Research (TNO). The main objective was to obtain an accepted set of methods and guidelines for the assessment of concrete structures with respect to the shear capacity [26]. In this workshop the beam in question was identified as beam 5, for uniformity, it will now be referred to as beam A.

6.1 Beam A properties

6.1.1 Geometry

The benchmark object consists of a simply supported beam loaded by a single concentrated load in the center of the beam, see figure 6.1. The loading scheme results in a constant shear force over the length of the beam. The bending moment distribution varies bi-linearly over the length with its maximum value at the center of the beam. Longitudinal reinforcement is distributed over the height of the beam, with varying diameters. The bottom reinforcement consists of $2\varnothing 20$ [mm] and $1\varnothing 25$ [mm]. The web reinforcement consists of 5 layers of $2\varnothing 10$ [mm]. This leads to a total reinforcement ratio ρ_s of 1.27%. No shear reinforcement is present in the beam.

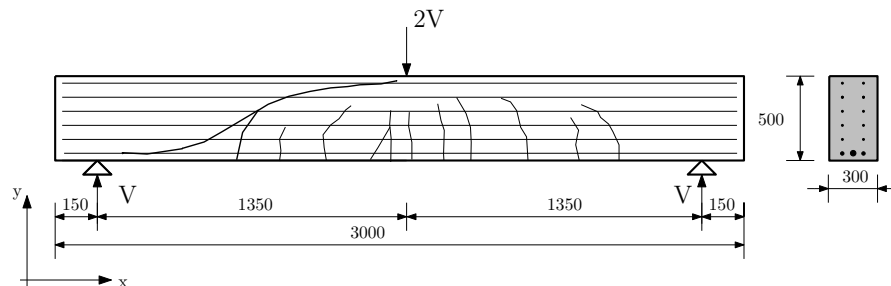


Figure 6.1: Geometry characteristics and crack pattern at moment of failure, the critical crack for which the beam ultimately fails is highlighted. Dimensions are in [mm].

6.1.2 Materials

The material properties have been provided by the workshop document. Properties that were not given have been computed using the CEO-FIP 1990 model code (MC90). This includes the tensile strength f_t , the modulus of elasticity of concrete E_c and the mode I fracture energy G_f . The material properties have been submitted to table 6.1.

Concrete					Reinforcement			
f_{ck}	37.0	[N/mm ²]	ν	0.15	[-]	f_y	398	[N/mm ²]
f_t	3.35	[N/mm ²]	G_f	0.075	[Nmm/mm ²]	E_s	210000	[N/mm ²]
E_c	35494	[N/mm ²]	d_{max}	10	[mm]	ν	0.3	[-]

Table 6.1: Material properties beam A for concrete and reinforcement

6.1.3 Load carrying capacity

The flexural moment-capacity of the beam is dependent on the amount of reinforcing bars that will contribute to the ultimate load by reaching their yield strength. It is therefore not possible to analytically determine an exact value for the flexural moment capacity, therefore an estimate is computed. The premise is considered that the bottom reinforcement and three layers of web reinforcement will reach their yield strength in case of flexural failure. This results in a moment capacity of 288.1 [kNm], with an applied load of $2V=426.8$ [kN]. The linear elastic capacity of the concrete section was determined at $2V=124.1$ [kN].

To analytically compute a shear capacity for this particular beam is not a simple task and depends strongly on the method in question. This is mainly due to the fact that the benchmark object is not reinforced with shear reinforcement. The analytical models that were presented in the shear workshop showed large differences in both the applied method and the predicted ultimate load [11]. We therefore provide an estimate for the ultimate shear load based on the shear capacity of the concrete section with an maximum allowable shear stress of $0.4f_t$. This leads to a maximum shear load of $V=201.0$ [kN].

6.1.4 Experimental results

The results were obtained from experiments performed by Podgorniak-Stanik in 1998 [15]. Although the beam was identified as beam 5 in the aforementioned workshop, the identification in the experimental results was "specimen BN50D". The ultimate shear load was determined at $V=162.7$ [kN]. From the experimental observations, the following comments were recorded:

The first flexural cracks occurred at a total load level of $2V=50$ [kN]. Thereafter, new crack developments consisted mainly of flexural cracks. On average, the flexural crack were spaced at 200 [mm]. At approximately $2V=200$ [kN] the maximum width of the flexural cracks was 0.25 [mm]. At this stage of the test it was evident that the tips of the flexural cracks were beginning to rotate in, toward the point of load application. by load stage 6 existing flexural crack on both ends of the beam had noticeable rotated to become primary diagonal crack. The flexural-shear crack extended for more than half of the specimen depth. The beam ultimately failed in shear at a shear load $V=162.7$ [kN]. The failure crack developed on the south end. This crack formed abruptly as it intersected the tips of the existing cracks. The beam displayed no warning as to imminent failure and did not possess any post cracking capacity once the failure crack developed.

6.2 Pre-processing aspects

6.2.1 Modeling environment

In accordance with one of the main assumptions of the beam theory e.g. the stress (σ_{zz}) in the out of plane direction is zero, the beam will be modeled with 2D plane stress elements. This will lead to an accurate solution without the use of an elaborate 3D model. Modeling in 2D will also reduce pre- and postprocess as well as the computational expenses. Because the beam and the loading scheme are symmetric, only half the beam can be used as a model, provided that the failure mode is also symmetric. In this particular benchmark, a symmetric model will be used throughout the study. To assess whether a possible non-symmetric failure mode is overlooked, a study will also be performed on a entire model in section 6.7.3.

6.2.2 Boundary conditions

Modeling only half the beam has consequences for the application of boundary conditions. In the centerline of the beam, the condition is enforced that the cross-section will remain perpendicular to the x -axis. To achieve this, all the nodes in the centerline are constrained in the x -direction. In order to let the beam expands and displace freely, the support condition consists only of a constrained y -direction.

The load and support forces are introduced via loading plates. The modeling of these loading plates is an essential part of the correct introduction of forces into the plane stress elements of the beam. Not applying load plates will lead to unrealistic stresses and unstable behavior of the incremental-iterative procedure. To avoid that the load plate of the concentrated load acts as a compression element together with the concrete, an interface element is applied. This interface element is constructed between the load plate and the concrete and represents a connection between the two materials. The interface describes a relationship between the tractions \mathbf{t} and the relative displacements $\Delta\mathbf{u}$ across the interface. In the normal direction of the interface, the stiffness modulus k_n was defined as $8.4e5$ [N/mm³]. This stiffness is derived with the premiss that the interface element represents a part of the load plate. This implies that the shortening of the load plate is the same as the relative displacement of the load-plate, thus:

$$\Delta u = \epsilon_s d \quad (6.1)$$

with ϵ_s being the strain and d defining the thickness of the load plate. Upon substituting the relationship between the stress and strain and rewriting the equation we obtain an equivalent stiffness for the interface in the normal direction:

$$k_n = \frac{E_s}{d} \quad (6.2)$$

This formulation represents an interface element with the same relative thickness as the entire load-plate. This would therefore lead to a doubling of the thickness of the load-plate. Because this is not correct, the stiffness of the interface element was selected at 1% of the thickness of the load-plate: $8.4e5$ [N/mm³]. The stiffness of the tangential direction k_t was chosen small, namely:

$k_n=50$ [N/mm³]. This proved to lead to correct results and the avoidance of compression forces in the load plate.

6.2.3 Element selection

The concrete is modeled using iso-parametric eight-node quadrilateral plane stress elements with 3×3 Gauss integration and quadratic interpolation.

The reinforcement will be modeled using an embedded formulation. The reason for this is that there are a number of bars at varying depths of the beam. Integrating these bars into the mesh lines would lead to a more difficult meshing procedure and an irregular sized mesh. These problems are avoided when embedding the reinforcement elements in a normal sized mesh. The embedded reinforcement formulation implies that the reinforcement strains are computed from the displacement field of the mother elements. Within each mother element the embedded elements are integrated using a 2-point Gauss integration.

A consequence of using the embedded principle is that a bond-slip model cannot be introduced. Another important consideration, when using an embedded or discrete truss formulation, is that the reinforcing bars have no bending stiffness. This means that the dowel action mechanism of the longitudinal reinforcement does not contribute to the shear capacity.

6.2.4 Spatial discretization

As a first estimate the mesh was designed with dimensions $b \times h = 50 \times 50$ [mm], with all of the elements having an aspect ratio of 1 [-]. The chosen dimension represents a normal sized mesh. Figure 6.2 displays the finite element model.

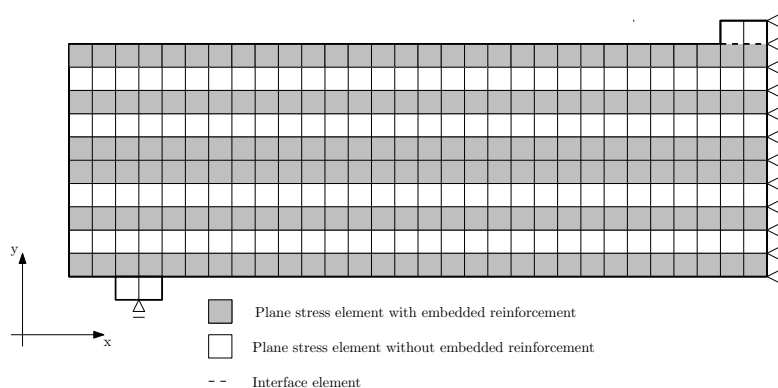


Figure 6.2: Finite element model beam A

6.2.5 Material modeling

The concrete will be modeled with linear softening in tension and parabolic softening in compression, unless indicated otherwise. The reinforcement will be modeled using the Von-Mises elastic-perfectly plastic constitutive model. See figures 6.3a and 6.3b.

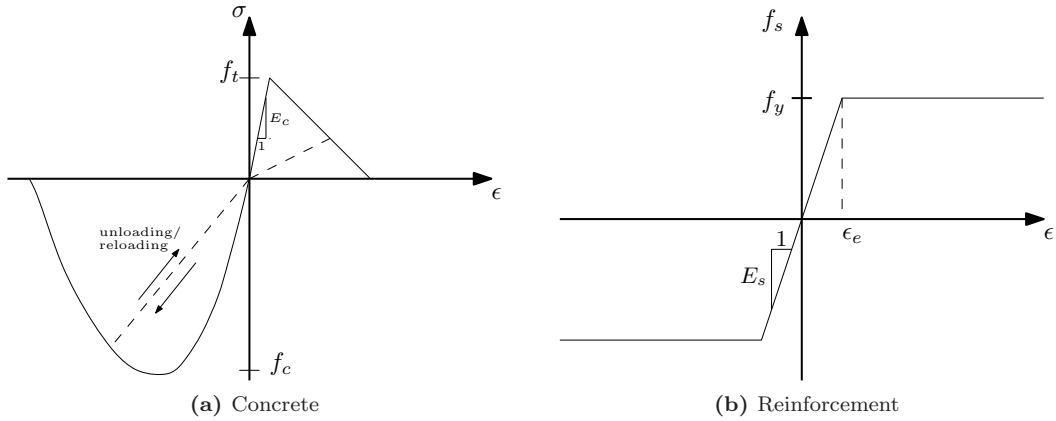


Figure 6.3: Constitutive models reinforcement and concrete

6.3 Preliminary analysis

Severe numerical difficulties are often encountered in the non-linear analysis of reinforced concrete structures. Structures that are characterized by softening material behavior therefore require advanced solution techniques to ensure that the incremental-iterative procedure provides correct results [7]. Therefore, in order to analyze the behavior of this benchmark object, the preliminary analysis consisted of a displacement controlled analysis in combination with a line-search technique and a force controlled analysis* in combination with a line search and an arc-length technique. The line search technique is designed to increase the convergence rate while the arc-length technique can trace the equilibrium path in both 'snap-back' and 'snap-through' behavior.

The incremental step-size in the displacement controlled analysis was set at 0.02 [mm]. Further aspects of the analysis process were: a regular Newton-Raphson procedure, with a maximum of 25 iterations. The convergence was governed by the force norm with a tolerance of 0.01 [-]. The force controlled analysis consisted of the same characteristics as the displacement controlled analysis, the only addition was the use of the updated normal plane arc-length method.

Both analysis consisted of the rotating total strain model, with a linear softening in tension. To avoid possible numerical complications with bi-axial stress states, a perfect-elastic model could be applied for concrete in compression. In this particular case however, this would have the consequence that the compressive concrete stresses would exceed the compressive yield strength. Not considering compressive strain softening would therefore lead to un-realistic results. Therefore, parabolic strain softening in compression was applied. The results from the analysis are presented through load-displacement diagrams[†], figure 6.4, that were monitored at the node of the applied displacement. Next to the load-displacement diagrams the crack patterns at failure of the respective analysis are depicted.

*From this point on, the term force controlled analysis always implies a force control procedure including an arc length method, although this may not be explicitly mentioned. The reason for this is that it is impossible for force control to overcome snap-through or snap-back behavior without an arc length. The use of only a force controlled analysis would therefore lead to poor results in the non-linear analysis of shear critical beams.

[†]From this moment on, all the load-displacement diagrams will imply shear-load V versus applied displacement. The depicted load-displacement behavior will always be monitored at the point of load application

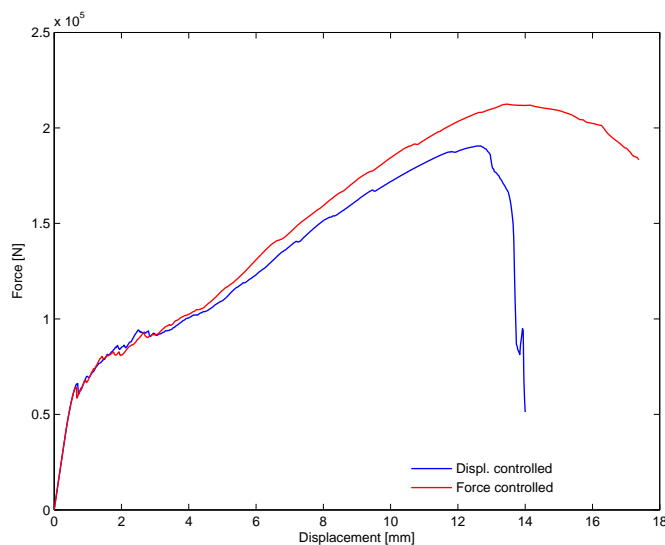
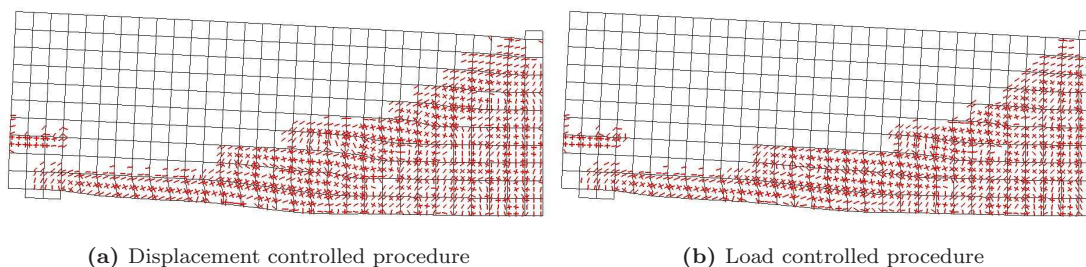


Figure 6.4: Load-displacement diagrams for two analysis with different control procedures



(a) Displacement controlled procedure

(b) Load controlled procedure

Figure 6.5: Crack patterns at moment of failure of respective analysis

When comparing the two load-displacement curves and the corresponding crack pattern development, we can distinguish reasonably similar behavior. Cracking is initiated when the linear-elastic capacity of the concrete section is reached. In the initial loading stage, the crack pattern consists of small cracks at the underside of the beam due to flexure. These cracks coalesce and form a number of large cracks, that grow diagonally into the web of the beam. After this stage of initial crack formation, the load displacement curves start to follow a stable path towards the ultimate failure load. For the displacement controlled procedure this is approximately $V=190$ [kN], while the force controlled procedure gives approximately $V=210$ [kN]. Although both beams fail at different load levels, the failure mode remains the same. In both analysis, the beams show failure due to a large crack, occurring approximately 650 [mm] from the support, leading upwards at an angle of roughly 45° . This crack is more prominently visible in the displacement controlled procedure, which also shows a more brittle failure than the force controlled analysis. When considering the manner in which the crack pattern evolved and the fact that the bottom reinforcement bars do not reach their yield strength, we can establish that the beam failed due to flexural shear. When comparing the experimental ultimate load value and the estimates made in the previous sections versus the numerical experiments, the load levels and failure modes are in good agreement.

The incremental-iterative processes of both analysis were characterized by high amounts of non-convergent increments*. When comparing the convergence characteristics of both analysis, little difference was distinguished between the force and displacement controlled analysis. The displacement controlled procedure lead to 42% of the increments failing to converge. while the load controlled analysis showed 46% of the increment failing to converge†. The main issue with a non-convergent increment is that it represents a un-true equilibrium situation, which has consequences for the accurateness of the solution. Therefore, the reliability of the solution devaluates considerably when large amounts of non-convergent increments are present. In this case, the non-convergent increments are seen as the main cause of the differences between the two performed analysis. In order to perform a consistent parameter analysis it needs to be ensured that the non-convergent increment do not compromise the results. The following sections will therefore consist of assessing different techniques for improving the incremental-iterative process, before continuing with a parameter variation.

6.4 Solution strategies

As was established in the preliminary analysis, finite element calculations involving strain softening often times lead to numerically unstable behavior of the incremental-iterative procedure. Even the application of line-search techniques and arc-length algorithms did not provide fully converged solutions.

The main objective of this section is to assess whether the incremental-iterative procedure can be ensured to result in a numerically stable and convergent process. This objective will be applied to both types of analysis that were presented in the preliminary analysis through a variational study. The displacement controlled procedure will be assessed on four parameters, namely: (1) The iteration procedure, (2) the number of iterations, (3) the norm tolerance and, (4) the increment size. The force controlled procedure will be extended with the findings of the displacement control variational study and through the use of indirect displacement control.

6.4.1 Iteration procedure

The characteristics of the available iteration procedures were discussed earlier in section 5.3. To investigate the effect of the different methods on shear critical beams, a comparison was made between the iterative procedure consisting of the Newton class methods‡. Included in this class are: the regular Newton-Raphson (rN-R), the modified Newton-Raphson (mN-R) and the Secant Newton (S-N) procedures, in which the Secant Newton method consisted of the BFGS method.

A comparison was made in relation to two different aspects, namely: the convergence rate and the required number of iterations. The analysis consisted of the same characteristics as the

*A non-convergent implies that the iterative procedure did not reach the value specified by the convergence norm within the maximum amount of iterations. This means that although no convergence occurred, the iterative procedure also did not diverge.

†Only the non-convergent increments that occur pre-peak are considered for the computations of the given percentages. Post-peak failed increments are not considered. This definition will be used through-out the thesis

‡Other possibilities include the constant stiffness and the linear stiffness method, but these are considered unsuitable for non-linear finite element analysis

preliminary displacement controlled analysis. The only difference was the maximum number of iterations, which was increased to 50 [-]. The reason for increasing the number of iterations is motivated by the fact that the mN-R as well as the BFGS procedure in general, require more iterations because the stiffness matrix is set-up only once at the beginning of the increment in case of the mN-R and the BFGS shows an oscillating type of convergence. The results from the analysis are displayed in table 6.2.

Iterative procedure	Non convergent increments [%]	Total number of iterations [-]
Regular Newton-Raphson	57.6	17182
Modified Newton-Raphson	31.6	15046
BFGS	3.0	3930

Table 6.2: Performance characteristics Newton class iterations methods

The performance of the Regular Newton-Raphson with regards to the convergence characteristics was very poor. In total, $\simeq 58\%$ of the increments failed to converge. The performance of the modified N-R, when compared to the regular N-R, was slightly more successful in relation to the convergence rate. Although the number of iterations is similar, the number of failed increments was only half that of the rN-R.

The behavior of the rN-R and mN-R generally showed two distinct patterns in case of a non-convergent increment (see figure 6.6), namely: (1) an initially converging behavior, changing to diverging behavior in a later stage, and (2) an initially converging behavior leading to an iterative process in which the iterative contribution $\delta\mathbf{u}$ to the incremental displacement was very small ($< 0.001\%$), with therefore no progress towards convergence. The first pattern was more prominently present in case of the rN-R, in which the tangential stiffness matrix \mathbf{K}_T is reformulated every iteration. This reformulation generally leads to faster convergence. In this particular case however, the newly formed tangential stiffness matrix often times lead to the wrong search direction and moved away from the actual solution. This behavior was less prominent in case of the mN-R where the tangential stiffness matrix is only set-up once, and in which the right search direction was obtained more often. The second pattern was exhibited by both procedures. Again the tangential stiffness matrix, which forms the relation between the out-of-balance force vector and the update in displacement was not configured properly. Therefore large numbers of iterations occurred in which the change of the incremental displacement update vector $\delta\mathbf{u}$ were very small.

A possible reason why the Newton-Raphson methods seems to fail is that the tangential stiffness matrix is not properly conditioned. The main reasoning for this statement is that a iteration method based on a secant stiffness, in this case the BFGS, provides significantly better results. The BFGS algorithm lead to a far more convergent numerical process, which in terms lead to a more computationally efficient calculation. The BFGS algorithm does however show, a distinct oscillating behavior towards convergence, with often times large variations ($\simeq 5\%$) between the iterated values of the norm of the out-of-balance force vector. The reasons for this oscillating behavior could possibly be caused by the fact that the stiffness matrix is updated every iteration. The BFGS method starts with a tangential stiffness matrix. After performing one iteration with

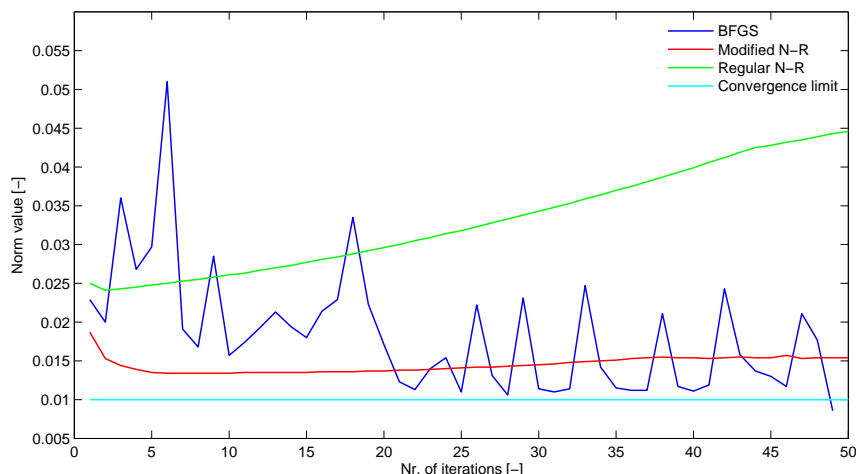


Figure 6.6: Characteristic behavioral patterns for different iterations methods of the Newton class. The force norm was applied for the analysis shown

this tangent, the subsequent iterations are evaluated with an updated tangential stiffness matrix using the Secant Newton formulation. The BFGS formulation, as was presented in section 5.3, uses previously calculated solution vectors and out-of-balance force vectors to achieve a better approximation. This update is particularly effective in many circumstances because the update to the tangent matrix is inexpensive and is done to a previously determined inverse so that no matrix inversion is necessary in most equilibrium iterations.

Although the application of the BFGS method was successful in achieving convergence, a small percentage non convergent increments remained. To eliminate this, the maximum number of iterations was increased to a 150 [-], which lead to a fully converged solution. Another essential aspect of the success of the BFGS procedure is the use of an explicit line search technique. The term explicit is used because the BFGS has an implicit line search technique built in to the iterative algorithm. The convergence characteristics of the BFGS procedure were not that different with or without the explicit line search. There was however a difference ($\simeq 20\%$) between the number of iterations needed per increment, which was larger when an explicit line search was not applied.

6.4.2 Norm tolerance

The norm tolerance is a quantity that defines whether the iterative process has reached an equilibrium state. When selecting stricter or slacker tolerances, the reached equilibrium states represent different levels of accurateness. Therefore the user of the finite element programme can determine the accurateness of the solution. In general, the tolerances are changed are for two reasons: (1) improving computation time by selecting a slacker tolerance and (2) selecting a more strict norm to ensure that the structural behavior is not affected by the accurateness of the equilibrium state of the previous increment. The second reasons bases itself on the fact that a slack tolerance leads to a build up of errors in the equilibrium states.

The preliminary analysis were governed by the force norm, with a standard tolerance of 0.01 [-]. Meaning that the remaining norm of the out-of-balance force vector, has a value of less than 1% of the norm of the out-of-balance force vector, determined at the start of the increment. This standard tolerance is used for a wide range of geometrically and physically non-linear calculations. In general it is not advised to adapt a slack tolerance, certainly not in the case of softening materials [13]. But the question is, as to what defines a strict or slack tolerance.

To assess the effect of different tolerances the displacement controlled analysis of the preliminary section was considered with varying norm tolerances. The selected tolerances consisted of a stricter value of 0.005, a more slack value of 0.02 and the standard value of 0.01 [-]. The analysis process were improved by applying the BFGS procedure from the previous section with 150 iterations. The force norm was applied because it is considered to be the most strict norm, and should provide results that can be considered to be as, or more accurate than the displacement or energy norm. The results are presented through load-displacement diagrams depicted in figure 6.7a

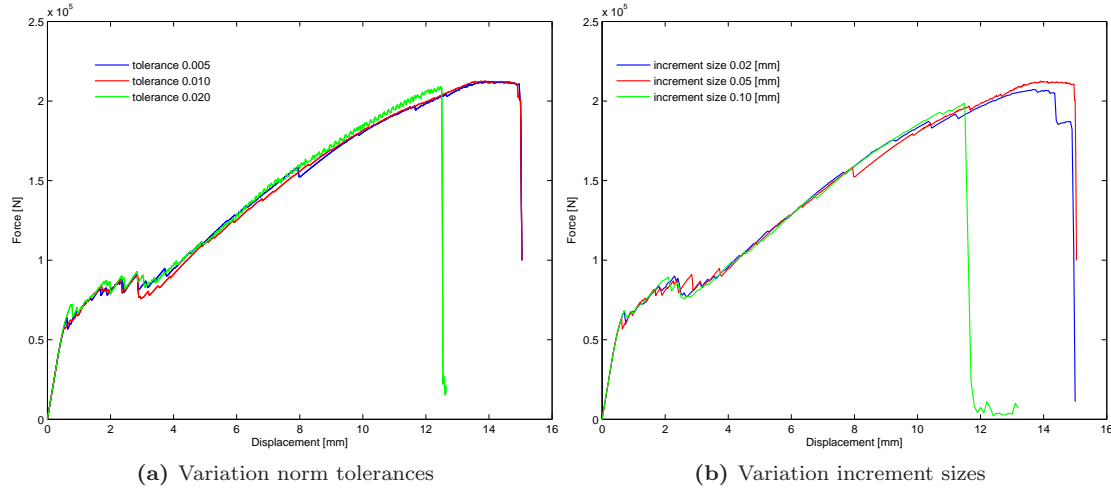


Figure 6.7: Load-displacement diagrams with norm and increment variation

When examining the load-displacement diagram, we can distinguish only little differences between the standard ($tol = 0.01$) and the more strict tolerance ($tol = 0.005$). Both analysis follow an almost identical path, with small variations in the range of 0.5-4.0 [mm]. The less strict norm ($tol = 0.02$) also displayed large similarities. However, with the slacker tolerance the beam failed earlier in comparison with the other analysis. Although the larger tolerance showed earlier failure, the accompanying load level was approximately similar. Besides this difference in displacement at the moment of failure, all of the analysis showed similar failure modes and crack patterns, see figure 6.8a and 6.8b.

When comparing the smallest tolerance with the standard tolerance, we can conclude that selecting a stricter norm tolerance generally does not lead to a stricter behavior of the rest of the incremental-iterative procedure. Meaning that the accurateness of the reached equilibrium state does not has a large influence on equilibrium states in the following increments. The levels of the out-of-balance force vector are more dependent on actual structural behavior than on previous levels of accuracy. All of the selected tolerances showed similar convergence characteristics

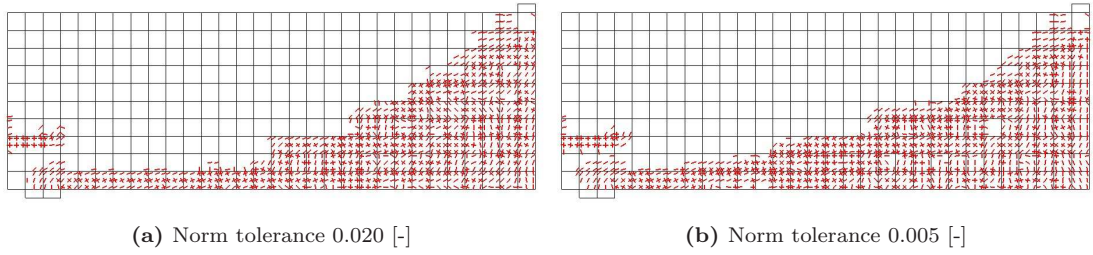


Figure 6.8: Crack patterns at respective moments of failure

with regards to the number of non-convergent increments. In all of the analysis the number of non-convergent increments was below 3%. The difference however, lies with the amount of computational cost, which was higher in case of a stricter tolerance. The standard and the more slack tolerance showed negligible differences but the strictest norm doubled the computation time due to the large number of iterations needed.

The general conclusion for this particular case, that choosing a more strict tolerance does not provide a more accurate solution and only leads to a greater computational cost. The second option of applying a more slack tolerance does not lead to increased convergence rate. It will lead to a slightly different structural behavior in relation to the ultimate load, that does not agree with the more accurate calculations.

6.4.3 Increment size

In general, a smaller increment size will be used for two main reasons, namely: (1) selecting a smaller increment size will provide a more stable and convergent numerical process, and (2) a smaller increment size will provide more accurate results. The first statement is based on the fact that when selecting a smaller step-size, the degree of non-linear response per increment is smaller and therefore the iterative procedure converges more easily. The second statement is motivated by that local strain localizations are better assessed and are not over-stepped which can be the case with larger increments. However, selecting a smaller step-size also leads to a larger computational expense, due to more increments being calculated. The large number of increments also lead to larger post-process files and accompanying post-process times.

To establish validity for the statement made above, a number of analysis were performed with varying increment sizes. Furthermore, to establish that the BFGS method is more numerically stable and more consistent with results than the (frequently used) modified Newton-Raphson, a variation was made between these iteration methods. Figures 6.9 and 6.10 display the load-displacement behavior of different increment-size and the accompanying percentage of non-convergent increments.

Upon examining the convergence characteristics of the BFGS procedure (figure 6.9b), a trend can be clearly distinguished that a smaller increment-size leads to a more stable and convergent numerical process. Next to this, it can also be distinguished that the load-displacement curves

of smaller increment-sizes tend to remain consistent with earlier analysis of large increment-sizes. The only difference occurs for the ductility of the beam, but the ultimate shear-load remain largely similar with an increasing number of increments. The modified Newton-Raphson however, does show a largely different behavior when compared to the BFGS method. First of all, the mN-R does not support the trend that, with a smaller increment-size the numerical stability is improved. Furthermore, large differences are encountered when using different increment-size. These differences lead to large variation in ultimate shear load ($\approx 40\%$) and in ductility ($\approx 75\%$) of the beam. The main reason for this difference between both iteration methods is the fact that the mN-R sets up a tangential stiffness matrix only once per load increment. When this tangential stiffness matrix is poorly conditioned, convergence is not obtained and the load-path may be influenced. This is not the case for the BFGS method, which applies a constant update to the initial tangential stiffness matrix.

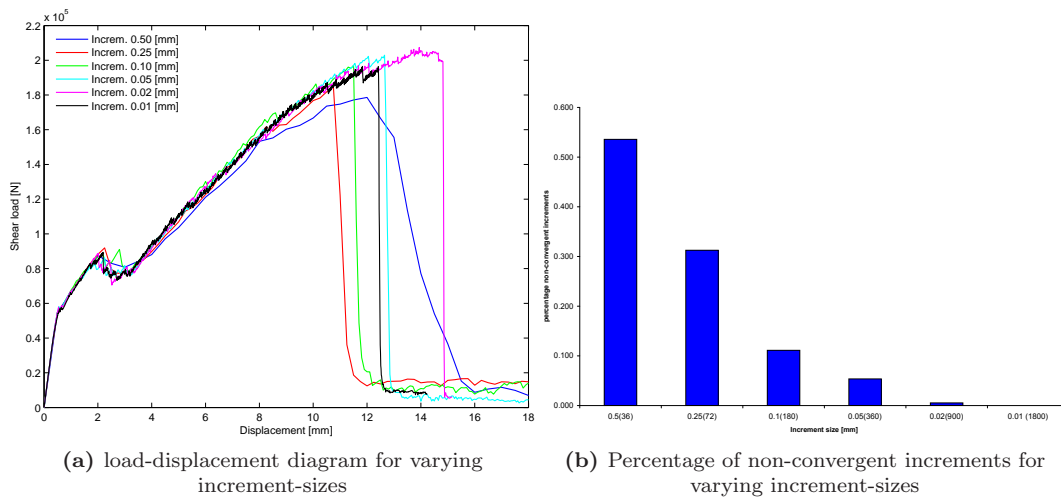


Figure 6.9: Performance characteristics BFGS method with varying increment-sizes

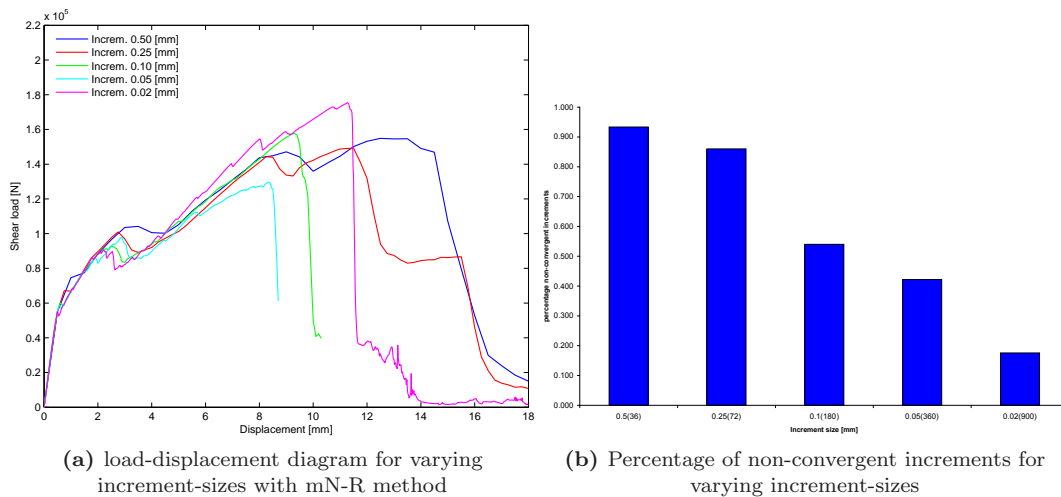


Figure 6.10: Performance characteristics mN-R method with varying increment-sizes

6.4.4 Indirect displacement control

The standard arc-length method, as used in the preliminary analysis, constrains the load vector by a constraint equation based on all the degrees of freedom in the model. In general, this does not lead to faster convergence in case of a strong non-linear response in reinforced concrete. This is because the global constraint equation cannot sense the local strain-localizations [6]. This was evident in the preliminary analysis in which the arc-length load controlled procedure did not provide better results than a standard displacement controlled procedure. To overcome these problems, indirect displacement control was introduced. In using indirect displacement control, only single nodal displacements or linear combinations of nodal displacements are selected that control the constraint equation. The only drawback is that by the use of indirect displacement control, the finite element calculation process loses its generality, because of the user selection of displacements.

Next to the loss of generality, the selection of an appropriate nodal displacement is usually not very straight-forward. In general, displacement are monitored at the edge of a structure, or in the case of large single cracks, at the tip of the crack. In this case, the crack pattern is too diffused to use the latter option. We therefore opt to constrain the arc-length through the nodal displacement at the location of concentrated load in the y -direction. A second analysis was performed with the monitored nodal displacement in the middle of the beam also in the y -direction.

The force controlled analysis was extended with the findings of the previous section to ensure that convergence would be reached. However, the convergence improving measures, that proved successful in the previous sections, did not provide better results for this particular case. Both analysis showed non-convergent increments ($\simeq 10\%$), even though the secant Newton procedure was employed with a large number of iterations. Furthermore, because the arc-length method constrains the length of the load vector to the degree of non-linearity, the number of load steps even increased to a 1050 [-]. These numerical difficulties lead to excessive calculations times, that were tripled when compared to the standard displacement procedure.

6.4.5 Summary

Benchmark beam A showed strong non-linear responses which lead to large numerical difficulties. One of the main reasons for this is that the brittle responses, severely influences the stiffness of the structures. The incremental-iterative does not have the intrinsic qualities to deal with these types of crack formations. Another main cause for these numerical problems are the occurrence of multiple cracks, limit points and bifurcations, which are usually associated with strain-localizations and alternative equilibrium states [8].

To overcome these difficulties the following measures proved to effective in achieving convergence (1) using a displacement controlled analysis (2) applying an iteration methods based on a secant stiffness formulation (3) applying small increment sizes and (4) allowing for a large number of iterations. The use of an load-controlled procedure in combination with an arc-length control did not provide full convergence, this was also established by [7, 8]

To underline the significance of reaching a fully converged solution, the displacement controlled procedure from the preliminary analysis was plotted versus the fully converged solution from the previous sections (figure 6.11). From this load-displacement diagram it is clearly visible that there are some significant differences. The main difference is that in case of the non-fully converged solution, the ultimate load is underestimated by approximately 15%. There are also differences regarding the overall stiffness of the structure and the displacement at the moment of failure (ductility). The non-fully converged solution also displays a more smooth load-displacement trajectory than in comparison to the fully converged solution. When comparing the ultimate shear load of the converged solution to the analytical and experimental values, we find better agreement than in case of the non-convergent solution.

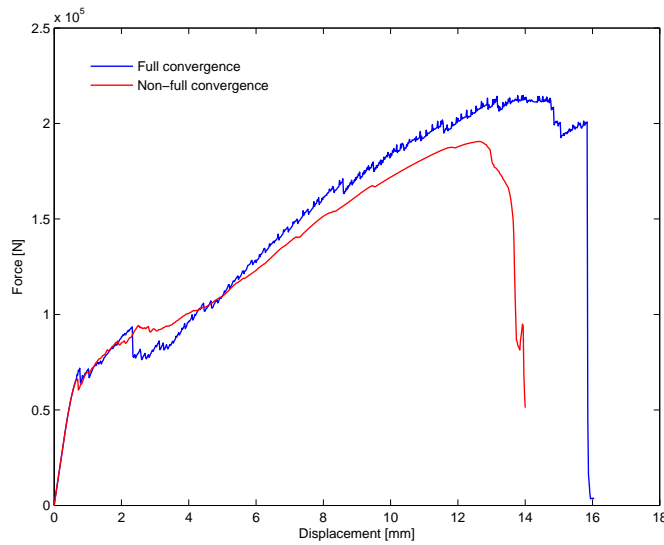


Figure 6.11: Load-displacement diagram for a fully converged solution and a non-full converged solution

From these conclusions the following is important to understand that: true snap-back behavior cannot be captured by a displacement controlled analysis and reaching a converged equilibrium only means that the finite element calculation has reached a solution deemed accurate enough by the user with the set of parameters used. Whether this holds in relation to the actual structural behavior can only be verified through experimental testing with large number of specimens.

6.5 Constitutive model parameters

6.5.1 Tensile behavior

Correct modeling of the tensile behavior of concrete constitutes one of the main objectives for obtaining a correct structural response of the finite element model. The reason for this is that crack formations due to tensile stresses are the main cause for failure of concrete under tension or compression loading conditions. In a smeared crack configuration, three main parameters need to be input for the constitutive model of concrete under tensile loading, namely: (1) the tensile strength of concrete, (2) the shape of softening function and (3) the amount of mode I fracture energy.

f_t [N/mm ²]	G_f [Nmm/mm ²]	Softening function [-]	Ultimate load [kN]	Failure mode [-]
3.35	0.075	linear	212.1	flexural shear
2.85	0.075	linear	177.5	flexural shear
3.85	0.075	linear	211.6	flexural shear*
5.00	0.075	linear	213.5	flexural shear*
3.35	0.150	linear	210.1	flexural shear
3.35	0.075	exponential	200.3	flexural shear

Table 6.3: Results from numerical analysis with variations of tensile strength, fracture energy and tension-softening function. The bold items are the varied parameters within the analysis. *Although the global failure mechanisms remains the same the stress-state for which these analysis fail is a tension-compression state, the other analysis fail solely due to tension

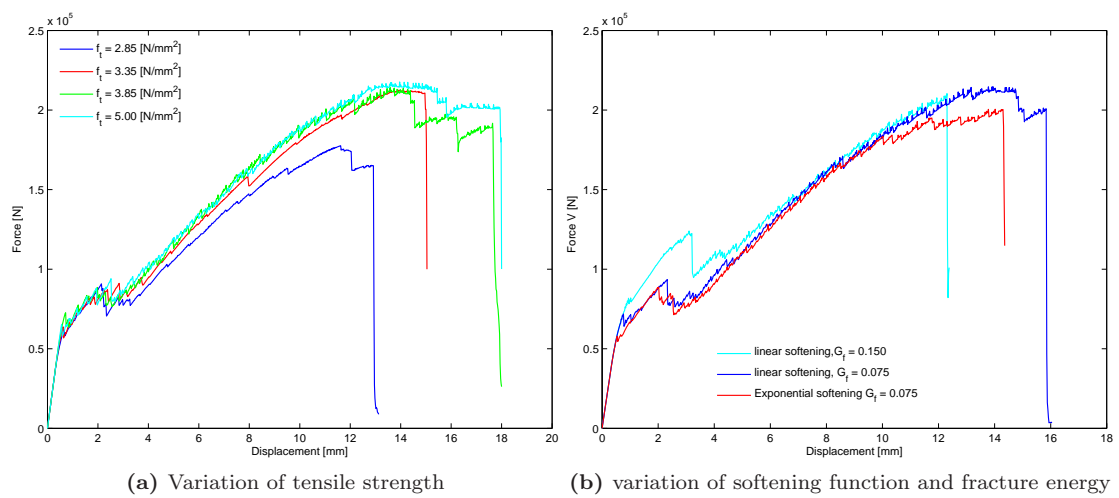


Figure 6.12: Load-displacement diagram for different constitutive model parameters

6.5.2 Tensile strength

The tensile strength of concrete is a material property that has a significant influence on the performance of RC beams. However, the exact value of the tensile strength can only be determined with a high degree of variation. When analyzing existing structures on their shear strength, the value of the tensile strength is even more difficult to obtain due to aging factors endured by the concrete structure during its life-time. Therefore, the objective of this section is to analyze the beam with the same material properties, but with a variation of the tensile strength. The reason for this is to assess the influence of the intrinsic uncertainty regarding the tensile strength. The tensile strength was varied with 2.85, 3.85 and 5.00 [N/mm²], the results have been submitted to table 6.3. The variation in tensile strength represent a variation of 30%. The largest tensile strength is chosen to be significantly higher to establish the following conclusions.

The analysis with the smallest tensile strength showed a significantly smaller ultimate shear load in combination with a less ductile behavior, e.g. less displacement before failure, than the standard analysis. The beam failed at $V=177.5$ [kN] with a displacement of approximately 12.0 [mm]. The analysis with the second largest tensile strength, 3.85 [N/mm²], resulted in a similar ultimate shear load as the original tensile strength, but displayed a more ductile post-peak behavior. To assess whether a more extreme value would lead to larger differences a tensile

strength of $5.0 \text{ [N/mm}^2\text{]}$ was applied. This analysis also proved to lead to a more ductile behavior but to only a negligible difference (1%) in the ultimate load.

It is interesting to see that in this particular case there is no proportionality between the ultimate load and the tensile strength. The smaller tensile strength lead to a reduced ultimate load, but the larger tensile strength did not lead to an increase in the ultimate load. The non-proportionality of the failure load is caused by the fact that, although the critical crack occur at the same location, the corresponding stress states are different. For the normal and reduced value of the tensile strength, the failure is solely due to tension. But in case of the larger tensile strength, the critical crack is formed under a bi-axial stress state* in which compressive and tensile strain localize. With this bi-axial stress-state the beam finally fails due to compressive failure of the compression diagonal. To illustrate the stress states, the magnitude of the principal strains are plotted in figures 6.13 and 6.14. The figures displayed consist of the analysis with tensile strengths 2.85 and $3.85 \text{ [N/mm}^2\text{]}$.

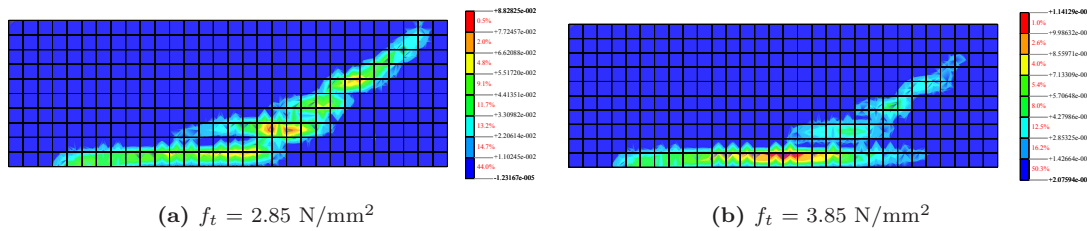


Figure 6.13: Principal tensile strain ϵ_1 at moment of failure of respective analysis.

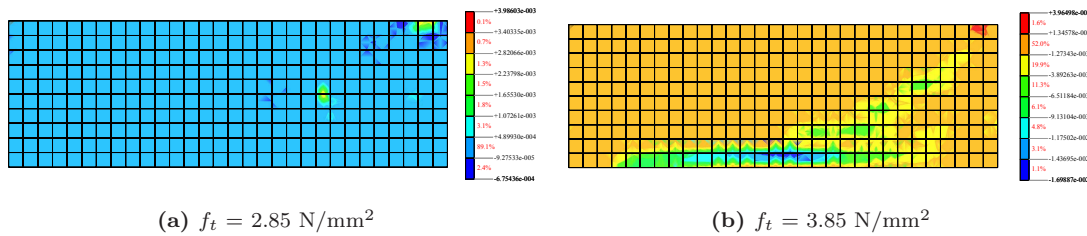


Figure 6.14: Principal compressive strain ϵ_2 at moment of failure of respective analysis.

When comparing the principal tensile strains we can distinguish that both analysis exhibit similar strain localizations for the ultimate crack. The difference between the analysis, is that in case of the smaller tensile strength the strain localizes more extensively. This more extensive localization leads to a smaller ultimate load than the standard analysis. The principal compressive strains show that the smaller tensile strength has almost no compressive strain localization, and that the compressive strain remains largely in the linear-elastic branch of the compression diagram. This behavior however, is not present in case of the larger tensile strength where the principal compressive strain localize in a similar manner as the principal tensile strains. This compressive strain shows extensive softening, and leads to failure of the beam.

*Although the beam fails due to failure of the compression diagonal it is important to mention that the bi-axial stress state contributes to this failure mode. The reason for this is the reduction of compressive strength due to lateral cracking according to the model of Vecchio and Collins

To further establish the conclusion that including compressive softening has significance influence on the structural behavior, a number of different analysis were performed in which the compressive fracture energy G_c was varied. The performed analysis consisted of using the tensile strengths 2.85 and 3.85 [N/mm²], with varying compressive fracture energies of 25.0 and 50.0 [N/mm]. Following the line of reasoning in the previous paragraph, the smaller tensile strength should encounter only a small influence from the difference in compressive fracture. While the larger tensile strength should encounter significant differences in structural behavior because of the failure of the compression diagonal. The performed analysis are presented through load-displacement diagrams in figure 6.15.

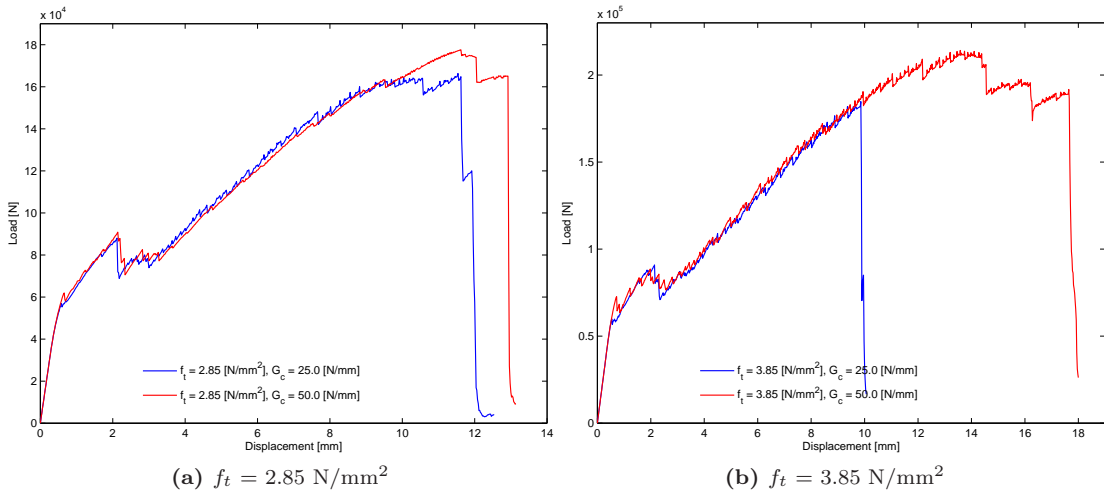


Figure 6.15: Load displacement diagrams for analysis with varying tensile strength and compressive fracture energy

Upon examining the load-displacement behavior of the tensile strength value of 2.85 [N/mm²], largely similar behavior can be distinguished. Only minor differences occur when the analysis reach their respective ultimate values. At this point, some compressive softening occurs and the influence is visible as a difference in ultimate load of approximately 5%. When examining the large tensile strength of 3.85 [N/mm²], the beginning stages also no real differences. However, at approximately 10.0 [mm] displacement, the analysis consisting of the smaller fracture energy shows failure at approximately 12% smaller value than the larger fracture energy. However, what is more important is that the ductility of the beam is severely affected by the smaller fracture energy, constituting a difference of roughly 80%.

The cause for this failure, is that the formation of a compression strut is not possible because of the low value of compressive fracture energy. The beam therefore fails in reasonable conjunction with the analysis consisting of the lower tensile strength. The analysis consisting of the smaller fracture energy, show a difference of 11% in the ultimate load value. The difference between displacement before failure is approximately 30%.

6.5.3 Tension softening function

As was outlined in section 4.4, there are a number of tension softening functions available. The linear softening function used in the previous sections is generally considered to be useful for overall structural applications. The reason for this being that the error introduced by using a linear diagram instead of non-linear diagram remains only small in case of normal sized beams [20]. The linear model however is considered to be a rough approximation of the actual behavior, which is captured more realistically by the non-linear models. These models based their respective softening functions on direct tension tests. For this section the used non-linear softening model was developed by Reinhardt [17].

When comparing the linear and non-linear softening functions, a difference of 5% was observed in the ultimate load value (see figure 6.12a). The reason for this seems to be that in the stage of extensive softening, right before failure, the non-linear softening function provided less stiffness leading to a smaller ultimate load. This reduced amount of stiffness was a consequence of more extensive softening that was observed in the later stages of the loading history.

6.5.4 Mode I fracture energy

The fracture energy is a measure for the amount of energy required to fully fracture a unit area of concrete. The mode I indication implies that the loading condition is pure tension only. The fracture energy that was used in the previous sections was determined with the use of the CEO-FIP model code 1990 (MC90). This code bases the fracture energy for concrete in tension as a function of the compressive strength and an experimentally obtained reference fracture energy.

The amount of fracture energy can also be seen as a measure for the ductility of the concrete. A zero energy value will lead to complete separation of the concrete upon violation of the tensile strength. Increasing the amount of fracture energy will lead to larger strains and more ductility. The amount of fracture energy can therefore be of importance in shear critical beams, where sudden crack formation are more likely to appear. To assess the effect of varying the fracture energy we compared the MC90 value of 0.075 versus a doubled value 0.15 [Nmm/mm²].

The influence of the larger fracture energy is clearly visible in the early stages of the tension stiffening of the beam. The large value provide a far more stiff behavior, after which a snap-through occurs and both the analysis follow an almost identical path. The analysis with the larger fracture energy does show a difference in the amount of displacement before failure. Although the ultimate load is very similar, 1% difference, the failure occurs prematurely in comparison to the standard analysis. One of the reasons for this behavior is that the beam has sustained more damage because of the initial drop in the load-displacement curve.

6.6 Evaluation of crack models

The smeared crack model used in the previous section was the rotating total strain model. Next to this smeared crack model, a fixed total strain model and a fixed multidirectional model are available. The main difference between the fixed and rotating total strain models are the manner

in which the cracks evolve under their respective loading history. Whereas the rotating crack model allows the crack to rotate with the axis of the principal strain, the fixed models constrain the cracks at the moment of formation and does not allow for rotation. The consequence of this latter approach is that the constraint of the cracks leads to a build-up of shear stresses on the face of the crack when the principal directions undergo rotation. The amount of shear stresses can be predetermined by a shear retention factor, that is defined either as a constant or a variable value. The description and details of the models were discussed in section 4.3.

This section will consider the performance of the rotating crack model versus the fixed crack model and multiple fixed crack model in combination with a constant shear retention of $\beta=0.05$ and $0.005*[-]$. This implies that upon rotation of the principal directions, a constant reduced shear modulus of respectively 5 or 0.5% of the original value was used. Next to the constant shear retention, a variable shear retention was investigated, that gives a relation for the shear retention factor in relation to the strain ϵ_{nn}^{cr} perpendicular to the crack. This implies that with increasing strain (crack width) there is a reduction in shear stresses. This appears to be a valid assumption since the amount of shear stresses are consequence of aggregate interlock, which is dependent on the constraint of the crack. Figure 6.16 displays the load-displacement diagrams that resulted from the different analysis.

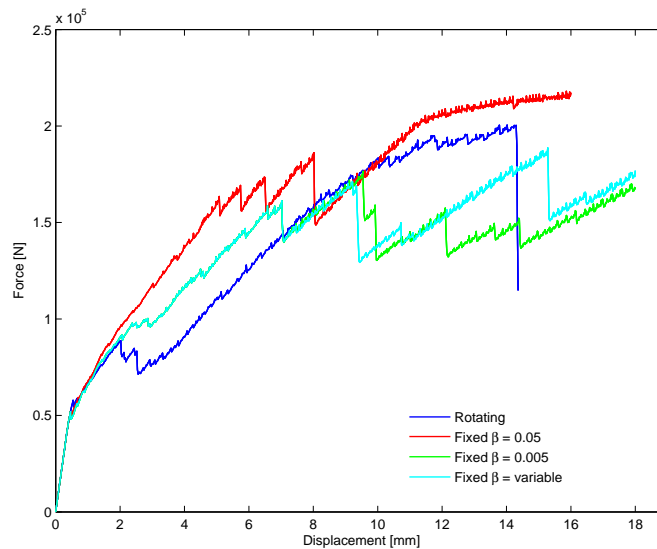


Figure 6.16: Load-displacement diagram with fixed and rotating smeared crack models

6.6.1 Fixed crack model with constant shear retention

In general the fixed crack model, in combination with a small (<0.05) constant shear retention, provides reasonable structural responses. However, due to shear stresses on the crack face, the ultimate load tends to be overestimated by these models. This shear stress occurs as a consequence of the rotation of the principal strain directions. In using a constant shear retention,

*This value for the shear retention can be regarded as zero. An actual value of zero would lead to numerical difficulties because of the fact that this value would constitute zero's on the main diagonal of the stiffness matrix. Therefore this value is chosen as very small

the shear stresses do not 'soften' down to zero upon increasing normal strain, which is more in agreement with the physical reality.

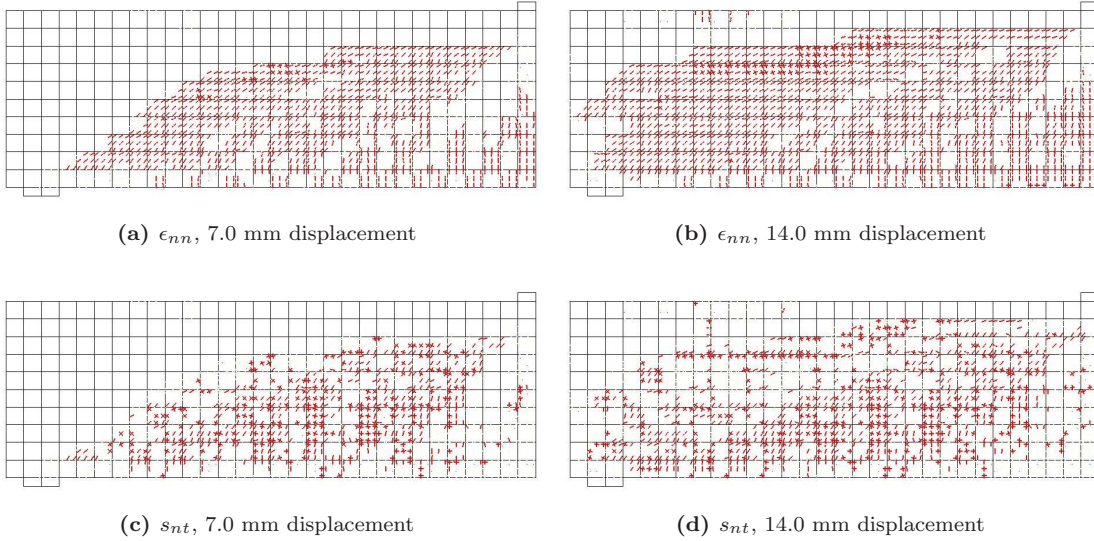


Figure 6.17: Crack patterns for fixed crack model with shear retention $\beta=0.05$ (top) and $\beta=0.005$ (bottom). Only cracks are portrayed that have either undergone full mode I softening or display crack shear stresses s_{nt} of larger than 0.5 N/mm^2

In this particular case, the analysis that consisted of the fixed crack model and a shear retention of 0.05 [-] lead to large shear stresses on the crack faces. The fixed model analysis with a shear retention of 0.005 [-], showed similar responses regarding crack formations and shear stress build-up as the larger shear retention factor. Only the degree of the stress-build up was slightly less severe.

The consequence of this shear build up is that the entire load-displacement behavior of the beam is compromised. From the load-displacement diagram in figure 6.16 we can clearly see a very different response when compared to the rotating crack model. The reason that the fixed model analysis do not end with a downward branch at the end of the diagram, is a caused by the fact that the entire load was carried by shear stresses on the crack-faces. The large build-up of shear stresses on the crack faces has two main consequences. Firstly the crack patterns are very extensive even in early loading stages, and secondly the beam exhibits additional load-carrying capacity only through shear stresses on the crack faces. To illustrate this the crack normal strain ϵ_{nn} and the crack shear stresses s_{nt} are depicted in figure 6.18. Only cracks are portrayed that have either undergone full mode I softening or display crack shear stresses s_{nt} of larger than 0.5 N/mm^2 When examining the crack patterns we can establish that the extent of the cracks is much larger when compared to the rotating crack model

6.6.2 Fixed crack model with variable shear retention

Next to the constant shear retention a variable shear retention factor can be used that is related to the amount of shear strain, see section 4.5. A linear descending variable shear retention factor and non-linear shear retention factor that descended exponential with increasing shear strain

were analyzed using the fixed crack model. Both these model however, did not lead to less stress-locking than in relation to a constant shear retention.

The response of both shear retention functions was similar. In the early stages of the loading process (<4.0 [mm]) both shear retention models showed crack pattern development that was in good agreement with the experimental results. However during subsequent loading, the principal directions start to rotate, and both models show excessive locking compromising the entire load-displacement behavior. A failure peak could therefore not be obtained and the analysis were ended.

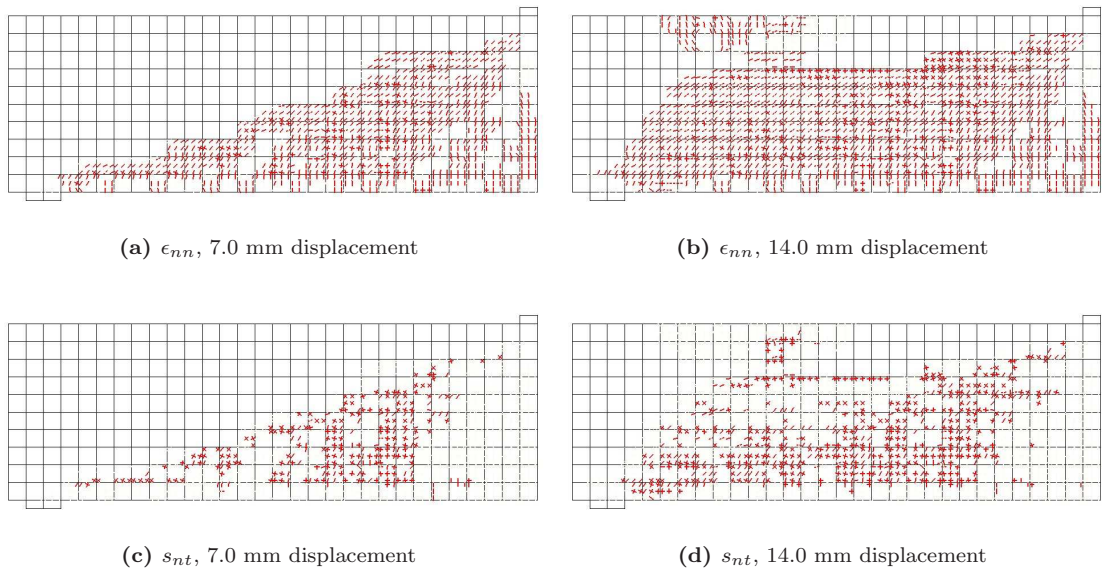


Figure 6.18: Crack patterns for fixed crack model with shear retention $\beta=0.005$. Only cracks are portrayed that have either undergone full mode I softening or display crack shear stresses s_{nt} of larger than 0.5 N/mm^2

To overcome the problems with excessive stress locking, a number of researchers have adopted different shear formulations. A widely used variant consists of shear retention factor based on the crack normal strain. This model is physically appealing since the shear transfer across crack is dependent on the aggregate interlock mechanism, and aggregate interlock is, among others, dependent on the width of the crack. However no such model is directly available in the used FE code, and is therefore not further investigated.

6.6.3 Fixed multi-directional crack model

The fixed multi-directional crack model allows for the formation of multiple fixed cracks under a predefined angle. This model constitutes a intermediate between fixing orthogonal cracks (fixed crack model) and allowing for constant rotation (rotating crack model) of orthogonal cracks. The fixed multidirectional is not based on the total strain formulation but uses the decomposed strain formulation in order to overcome certain difficulties regarding the correct representation of multiple cracks. In this particular analysis the angle for which a new crack may be formed was set at 60° , and the linear tension cut-off criterion was used.

Upon performing the analysis it was found that the model provided a good initial representation of the crack pattern (figure 6.19) and the accompanying load-path. However, at approximately 4.0 [mm] displacement, the iterative procedure would diverge. When examining the model for a possible cause for this problem, no real indications such as irregular deformations or sudden extensive crack patterns were found. It was therefore concluded that the divergence was solely caused by a numerical issue. To stabilize the numerical procedure, a number of measures were applied to improve and possibly ensure convergence. As a first measure, the increment size was decreased to 1/2 and 1/4 times the original increment-size. This measure however, did not lead to any improvement divergence still occurred. As a second measure the linear tension cut-off criterion was replaced by a constant cut-off criterion, this however also did not lead to the avoidance of divergence. Further measure included linear softening instead of exponential softening, and omitting the use of compressive softening. Both these measures did not lead to improved behavior of incremental-iterative procedure. As a final measure, a restart of the incremental-iterative procedure was performed with a different stiffness. This measure was motivated by the fact that the iterative procedure diverged at the very first iteration. The BFGS method used a tangential stiffness at the very first increment, therefore the restart was performed with a stiffness obtained from previous convergent increment. However, again no improvements were obtained. Therefore the fixed multidirectional crack model was abandoned as a feasible crack model for this particular beam.

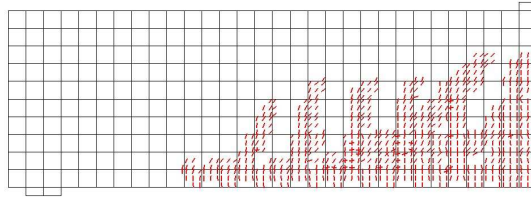


Figure 6.19: Crack-pattern at the moment of last converged increment for the multi-directional fixed model

6.6.4 Rotating total strain crack model

The rotating crack model for has proven to be reasonably successful in modeling reinforced structures that are dominantly loaded in mode I [22, 14, 20]. In this particular case, the performance of the rotating crack model was also in good agreement with the experimental results. An ultimate shear load of $V=200.3$ [kN] was found, with a crack pattern that corresponds with the experimentally obtained crack pattern. Figures 6.20a and 6.20b depict the crack pattern for two different load-stages. Only cracks that have undergone full mode I softening (i.e. $\epsilon_{nn}^{cr} > \epsilon_{nn;ult}^{cr}$) are portrayed. From these crack patterns we can distinguish that the rotating crack model gives a far less extensive crack pattern, than in comparison with the fixed model. However, the crack pattern of the rotating model is still far more extensive than for in comparison with the experimental crack patterns. A more detailed elaboration of the rotating crack model versus the experimental results is given in section 6.8.

The application of the rotating crack model does show one drawback, that is a consequence of the rotation of the principal directions. Because cracks rotate constantly in order to remain

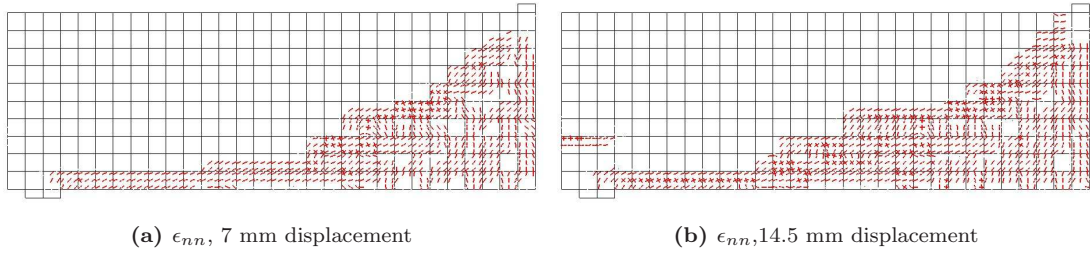


Figure 6.20: Crack patterns for rotating crack model, only cracks that have undergone full mode I softening are depicted

perpendicular to the principal strain directions, they can also exhibit an over-rotation. An over-rotation in this case, is a rotation of a crack to such a degree that it does not conform with the physical reality. The main issue with rotating cracks is that, because of the nature of the smeared cracking concept, cracks represent a reduced stiffness in the direction to the normal of the crack. That means that if a crack is formed and undergoes softening, it represents a reduced stiffness in its initial direction. When this crack rotates, the direction of the reduced stiffness also rotates leading to a reduced or even zero stiffness in an initially un-cracked direction.

To illustrate the over-rotation of cracks, the crack-patterns of the fixed and rotating crack model are depicted in figure 6.21a and 6.21a. Because the fixed crack does not allow for rotating we see that the cracks remain virtually perpendicular to the reinforcement and only show different angles in elements above the reinforcement. The rotating crack model however, shows cracks that have aligned with the reinforcement. This rotation is physically un-realistic because cracks generally stay perpendicular to the reinforcement.

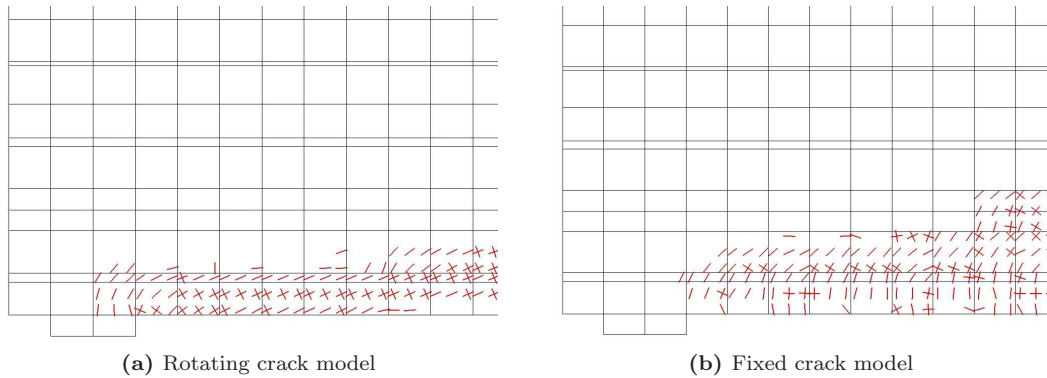
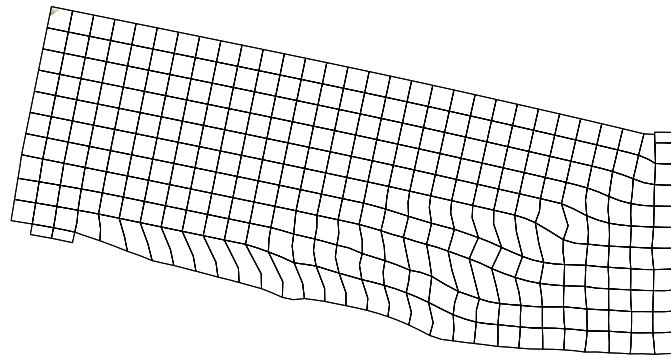


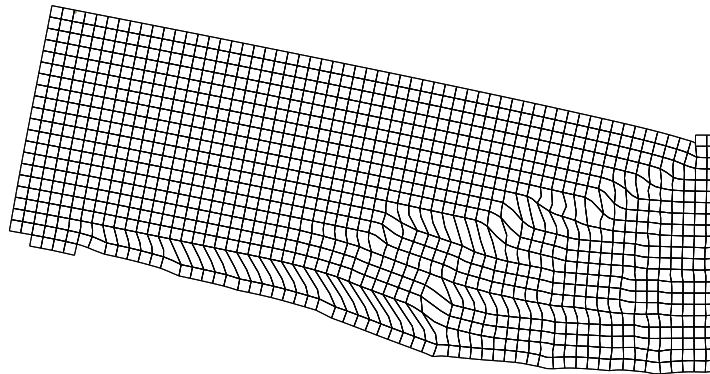
Figure 6.21: Crack patterns at the location of the main longitudinal reinforcement of the beam near the support, only cracks that have undergone full mode I softening are depicted. The blue lines indicate the reinforcement.

The over-rotation of crack has two main consequences, namely: (1) unrealistic strain and therefore deformation localizations and (2) unrealistic crack propagation in element containing reinforcement. To illustrate the first statement, figure 6.22a and depicts the deformed mesh of the rotating crack model analysis at the moment of failure. The deformed mesh shows the failure of the beam through the shear-band caused by the critical crack. However, it is also visible that the deformation is localized in element containing reinforcement (red lines) and that these

localizations extent horizontally over a number of elements. The exact extent of the influence of these strain-localizations on the ultimate load and failure mode is difficult to assess. The main reason for this is that there are no other smeared crack models, used in this thesis, that could provide results for comparison. When comparing the deformations and crack-pattern formation between the analysis and the experimental results, some differences can be distinguished. The main difference is that the ultimate crack in the experimental results is a reasonably continuous crack without horizontal cracks in the web section of the beam. The analysis results of the rotating crack model on the other hand, predict horizontal cracks in the web section of the beam and more extensive horizontal cracking at the location of the bottom reinforcement.



(a) Mesh 50×50 $b \times h$ [mm]



(b) Mesh 25×25 $b \times h$ [mm]

Figure 6.22: Deformed mesh plots at moment of failure, deformations are exaggerated

When analyzing the behavior of the crack that over-rotate, it was found that the over-rotation occurs only in particular cases. The main observation was that the cracks only rotate in elements containing reinforcement. Upon further analysis it was found that using triangular element instead of quadrilateral element did not prevent rotation of cracks towards reinforcement. Another aspect of the rotating crack model is that upon mesh refinement, the strain localizations remain within the reinforced element. It was also found that the strain-localizations are more extensive with more element undergoing shear deformation. This is illustrated in figures 6.22a and 6.22b through deformed mesh plots, and the strain evolution of a typical element containing reinforcement is shown in figures 6.23a and 6.23b. Another important observation was the fact that cracks, for the large part, rotate while softening. Upon crack formation, the crack are perpendicular to the reinforcement, with during softening a gradual rotation towards the reinforcement. At the moment that the crack are fully softened there directions remain reasonably unchanged.

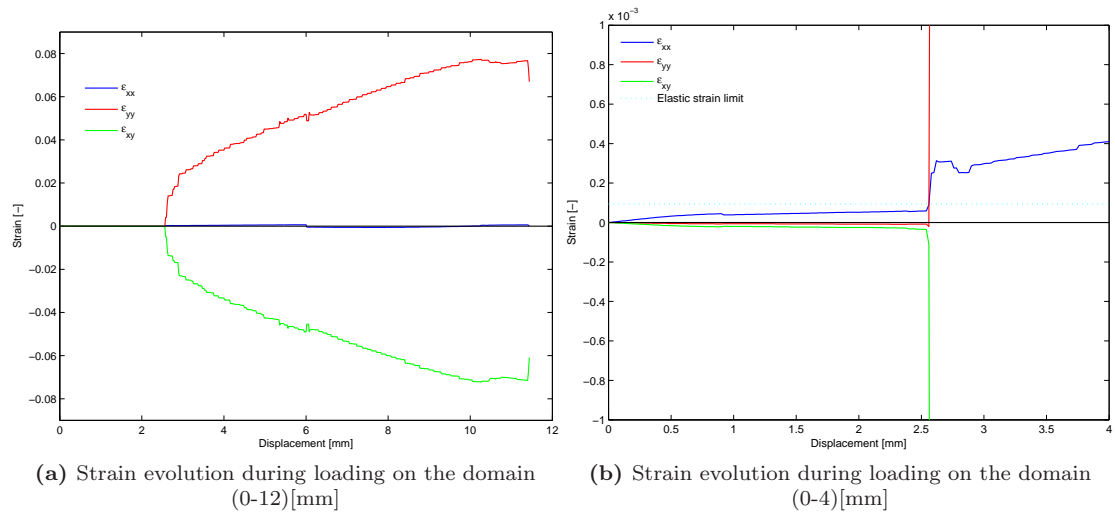


Figure 6.23: Strain evolution of an element containing reinforcement using the rotating crack model

The exact cause for this phenomenon of over-rotating cracks and the accompanying strain localization is difficult to assess. However, as a tentative conclusion, two main reasons are considered to be the cause of the problem, namely: (1) experimental of panels with large shear stresses show that the rotation of principal stress directions lag behind the rotation of principal strain directions [21], and (2) the transfer of concrete stresses to steel stresses is considered to be not properly configured for element that are reinforced in only one direction. To elaborate on the first statement, experiments have shown that principal stress and strain directions do not always coincide. The rotating crack model however enforces that the principal directions always coincide with the so-called co-axiality principle, as was presented in section . To enforce this coincidence of principal directions, rotating crack model generates a shear stiffness. This shear stiffness would explain the typical strain-deformations. The second statement is motivated by the fact that upon the moment the concrete stresses are normally transferred to the steel, the rotations occur. It is probable that the strain and stress directions deviate from each other, creating the earlier mentioned shear increment. This would again explain the shear stiffness and why this only happens in element containing reinforcement.

When discussing whether the rotating crack model can be made more physically correct by not allowing over-rotation of crack we come a few possible measures. First off all, it is possible to allow the crack to rotate only over a predefined range, this would circumvent a possible over-rotation of the cracks. However, defining such an angle is difficult to physically justify. Another possibility could be to include the dowel-action mechanism. The inclusion of this mechanism could play an important role on element stiffness level, because it provides a resistance against the shear deformation of the element.

6.6.5 Summary

From the previous sections, the following conclusions can be drawn regarding benchmark A. The tensile strength has a large influence on the structural behavior of the beam. It has an influence

on the ultimate shear load and the stress-states for which the failure crack is developed. The fracture energy and the shape of the softening function do not have significant influence than the tensile strength.

For this particular benchmark the use of the fixed crack models with a constant shear retention did not provide correct results. The combination of the fixed model with the constant shear retention will lead to a build-up of shear stresses on the crack face, which influence the structural behavior of the beam. In this case the stress-locking caused excessive crack patterns and over-stiff behavior. Selecting a very small value of the shear retention factor or using a variable shear retention factor did not improve the structural results. The fixed multidirectional model showed divergence for this particular benchmark, extensive measure could not avoid divergence and therefore, proper results could not be obtained. The rotating crack model provides results that are structurally in good agreement with the experimental results. However, the rotating crack model suffers from over-rotating of cracks leading to un-realistic shear localizations.

6.7 Spatial discretization

Spatial discretization or mesh design, is an important part of a correct finite element model. However, guidelines for the type of element and their respective dimensions are not widely available for specific structural problems. The objective of this section is to map out the influence of the different mesh characteristics such as element choice and dimensional properties of the mesh design. These characteristics will be compared on three different aspects, namely: (1) objectiveness of results upon mesh refinement, (2) crack formation and propagation in relation the mesh alignment and (3) differences between triangular and rectangular mesh designs. The investigated mesh-designs are depicted in figure 6.24. As a final aspect of spatial discretization, an analysis will be performed on a model of the entire beam.

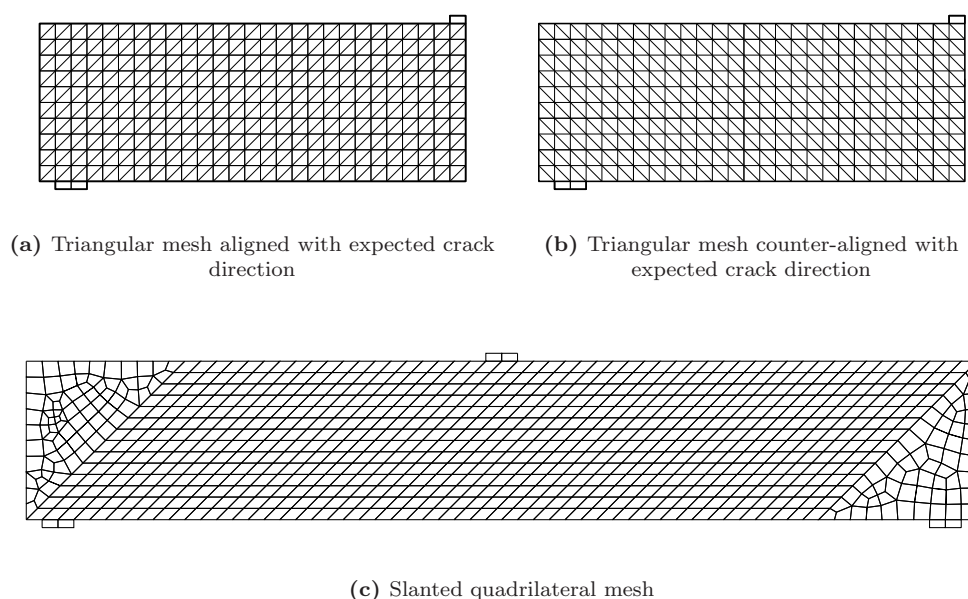


Figure 6.24: Investigated mesh designs

6.7.1 Mesh dimension

In general it can be established that there are three criteria for defining the dimensions of a mesh (1) a too coarse mesh size (2) a correct mesh size and (3) a too fine mesh size. The consequences of a too coarse mesh size are that general accuracy requirements are not met. The obtained results may therefore lead too wrong conclusions regarding the shear capacity of the beam. The consequence of selecting a too small element size is that although accuracy increases, the calculation process may become computationally very expensive, since a larger stiffness matrix requires more computations to set-up and solve the set of linear equations. Selecting the correct mesh dimension is therefore not a straightforward task. Therefore, in this section the standard quadrilateral mesh ($b \times h = 50 \times 50$ [mm]) as used in the previous sections was examined and compared to finer mesh designs of $b \times h = 35 \times 35$ and $b \times h = 25 \times 25$ [mm]. The mesh designs will be assessed on their structural response with particular attention for the objectiveness of the results upon mesh refinement. This objectiveness implies that upon selecting a smaller mesh dimension the structural response remains the same. In a smeared crack formulation using the fracture energy approach, the mesh objectivity is obtained through an equivalent crack bandwidth h . This crack bandwidth relates the energy dissipation during fracture to the dimension of the element to ensure objective results. The bandwidth was defined as \sqrt{A} , with A defining the element area, for a quadrilateral plane stress elements.

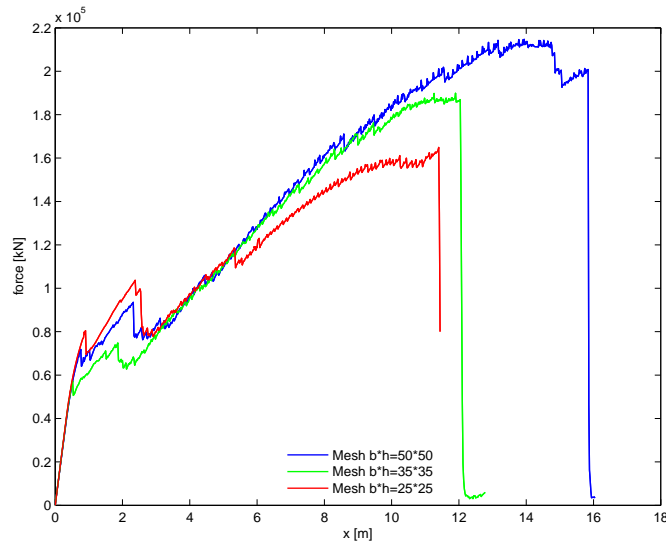


Figure 6.25: Load-displacement diagram for three different mesh dimensions

After analyzing the standard mesh dimension versus both the finer mesh dimensions, it was found that a pronounced mesh bias was distinguishable. The bias is particularly visible in the load-displacement diagram as depicted in figure 6.25. From this diagram we can observe that after 6.0 [mm] displacement the curves start to follow different load-paths, which eventually results in a difference of approximately 40.0 [kN] between the largest and the smallest ultimate load value. Upon further investigation of the differences between the analysis, two main observations were made: (1) the strain localizations tends to localize in single elements only and (2) the deformation consequences of the over-rotation of cracks near reinforcement layers is more pronounced in case of a finer mesh.

To illustrate the first observation, the contour plots of the principal strain ϵ_1 are depicted in figure 6.26a for the largest mesh dimension and 6.26b for the smallest mesh dimension. The depicted strain-contour represents an early stage of loading, in which the flexural cracks start to grow into the web. From these figures, the strain-localization in only single elements is clearly visible. In general, mesh objectivity is obtained through the use of the fracture energy approach. In this particular case, this objectivity does not seem to be compromised. The reason for this is that although the strain localizations are smaller, the strain peaks are significantly higher. Because the fracture energy represents the area under the softening branch, the ultimate strain varies with different mesh dimensions. The consequence is that the strain should be larger for a smaller mesh dimension to dissipate the same amount fracture energy as a larger mesh dimension. In this case the strain of the $b \times h = 25 \times 25$ [mm] should be approximately 1.75 times the strain of the larger mesh dimension, $b \times h = 50 \times 50$ [mm]. This statement however cannot be completely verified.

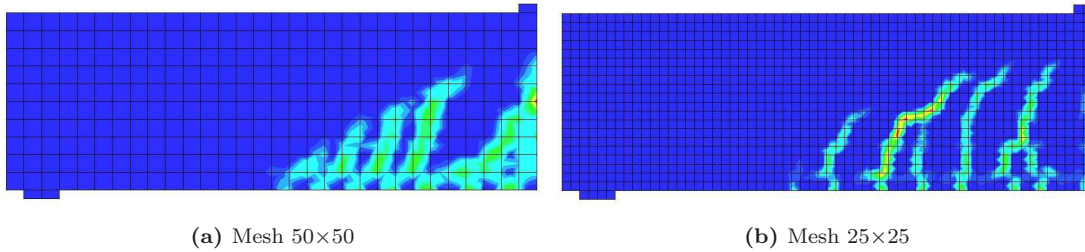


Figure 6.26: Principal tensile strain ϵ_1 for two different mesh dimensions at 2.50 [mm] displacement

The second observation that is made with a finer mesh dimension is that the rotation of the principal directions is more pronounced. From the crack patterns in figure 6.27a and 6.27b we can observe an interesting difference between the analysis. The smallest mesh design shows a more distinct crack pattern (as could be expected) than the larger mesh designs, who show a more blunt crack formation with less distinction between different cracks.

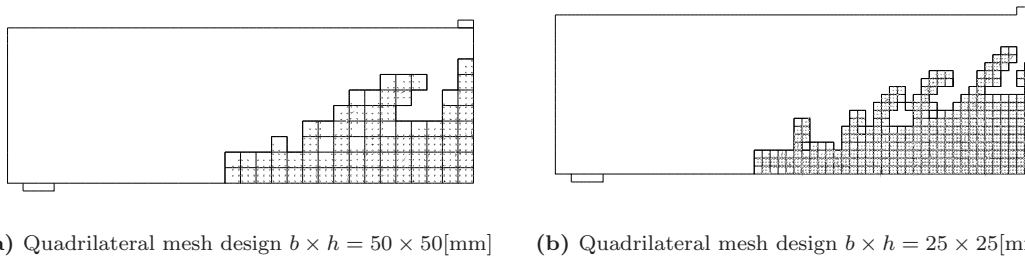


Figure 6.27: Crack patterns at 2.0 [mm] displacement for different quadrilateral mesh dimensions

What is also visible, is that the over-rotation of the principal directions and the accompanying crack formation along the bottom reinforcement in case of the 50×50 [mm] mesh. This over-rotation leads to a crack formation along the entire underside of the beam. In normal circumstances this is not the expected crack pattern. In the case of the two smaller mesh dimensions the over-rotation occurs not only for the bottom reinforcement but also for the web reinforcement.

In section 6.6.4, it was elaborated that the over-rotation of the principal directions expresses itself in shear and transversal strains. To show that a finer mesh is more sensitive for over-rotation, the shear strains have been depicted in figure 6.26a. The large mesh dimension shows only significant shear strains localizations at the location of the bottom reinforcement. The overall picture of shear strain localizations is one of a very blunt nature. The smaller mesh dimension however also shows more pronounced shear strain localizations at the locations of the main as well as the web reinforcement. The question could be posed whether these localizations are actual behavior of the RC beam. However, in normal circumstances a crack will not likely propagate horizontally into the web. When we disregard these localizations around the web reinforcement, we can distinguish a fairly good agreement between the critical crack formations of the experimental results and of these results.

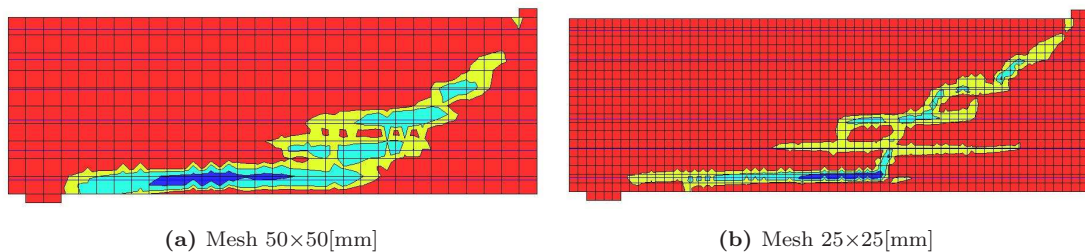


Figure 6.28: Contour plot shear strains ϵ_{xy} at moment of failure of respective analysis are portrayed. The reinforcement is indicated with blue lines

6.7.2 Mesh alignment

Because of the nature of quadrilateral elements and their selected orientation, the respective mesh designs generally consist of reasonably square elements aligned with the orthogonal $x - y$ system. When applying triangular elements, the mesh is also by nature aligned or counter-aligned with the expected crack pattern. Crack formation in concrete however, has the tendency to rotate after formation and propagate at an angle towards the compression zone of the beam. This is certainly the for flexural crack that form in the shear spans of RC beams. To assess the influence of the alignment of the elements in relation to the crack formation and propagation, a comparison is made between a number of different mesh designs. The mesh designs with triangular elements are depicted in figure 6.24a and 6.24b. These figures display two mesh designs using triangular elements but differ in the direction of the mesh lines. Furthermore, a comparison will be made between the standard mesh design as used in the previous sections, and an slanted (aligned) quadrilateral mesh. The slanted mesh designs consists of a model of the entire beam, this was necessary for a correct mesh design

The quadrilateral meshes consisted of the standard eight-node element with 3×3 Gauss integration. For the triangular mesh, six-node elements were applied. These triangular element were integrated using 7-point Gauss integration. This integration scheme proved to give numerical stable results, unlike the 3 and 6-point Gauss integration schemes that resulted in numerical problems due to spurious energy modes.

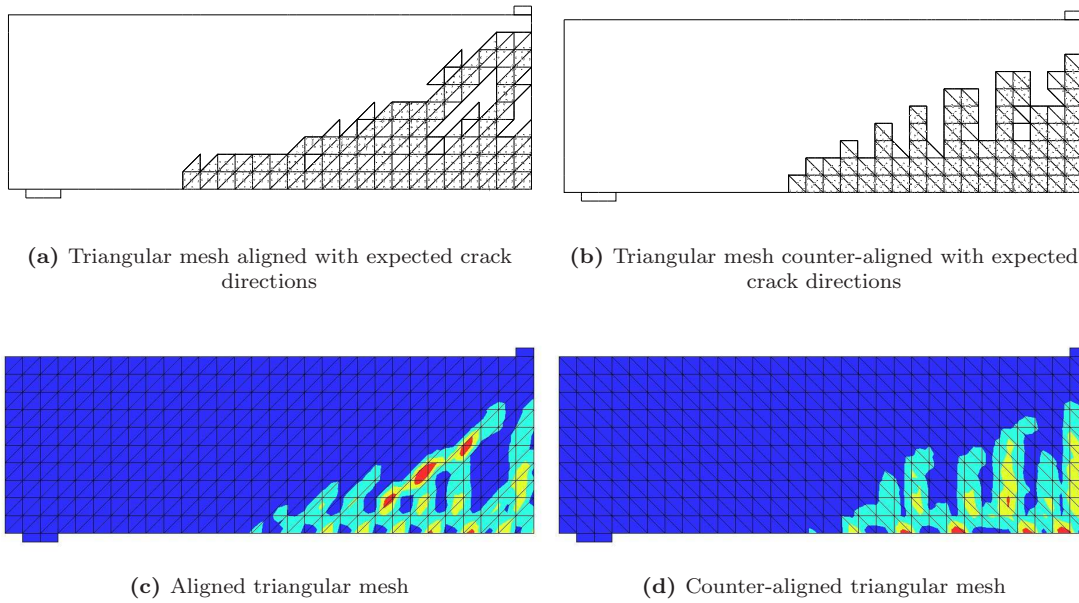


Figure 6.29: Crack patterns and strain ϵ_{xx} contour plots for triangular mesh designs at 2.0 [mm] displacement

One of the main observations in comparing the analysis results, is that there is a significant directional bias when using triangular elements. The crack formations in case of the aligned triangular mesh show a very different crack pattern in comparison to the counter-aligned mesh. The aligned triangular mesh shows a crack formation, in which the main cracks slope upwards towards the loading plate. In this stage of the load application the beam is in the starting stages of tension-stiffening, the cracks that follow from this tension-stiffening are expected to be formed due to flexure, and form perpendicular to the longitudinal axis. This crack patterns is much more visible in case of the counter-aligned mesh. To further illustrate the directional bias, the strain ϵ_{xx} contour is plotted in figures 6.31c and 6.29d. The contour plots clearly show how the strain in the aligned mesh has the tendency to localize in the direction of the element lines.

As a consequence of this dimensional bias, the ultimate shear load is affected. In case of the aligned mesh, the beam fails due to reaching its flexural moment capacity, $V=218.3$ [kN]. This is an interesting fact because although aligned meshes show easier crack propagation, the ultimate load is not lower. The counter-aligned mesh shows a ultimate load and failure mode that is consistent with a rectangular mesh. An important observation is that the crack direction of the individual integration points are very similar, in both triangular mesh designs. The main difference occurs for the direction in which the crack grows over the elements.

When comparing the standard quadrilateral mesh design versus the slanted mesh design, we can again distinguish a directional bias. This bias however is less pronounced when compared to the triangular elements. Figures 6.30a to 6.30c show three crack patterns. From these crack patterns a number of observations can be made. In the beginning load stages, we see that the cracks have the tendency to align with the mesh, with a large crack at the left-side of the beam. Upon further loading, the main crack however develops on the right-side of the beam, in the counter-aligned direction. This crack also leads to final failure. The accompanying failure load

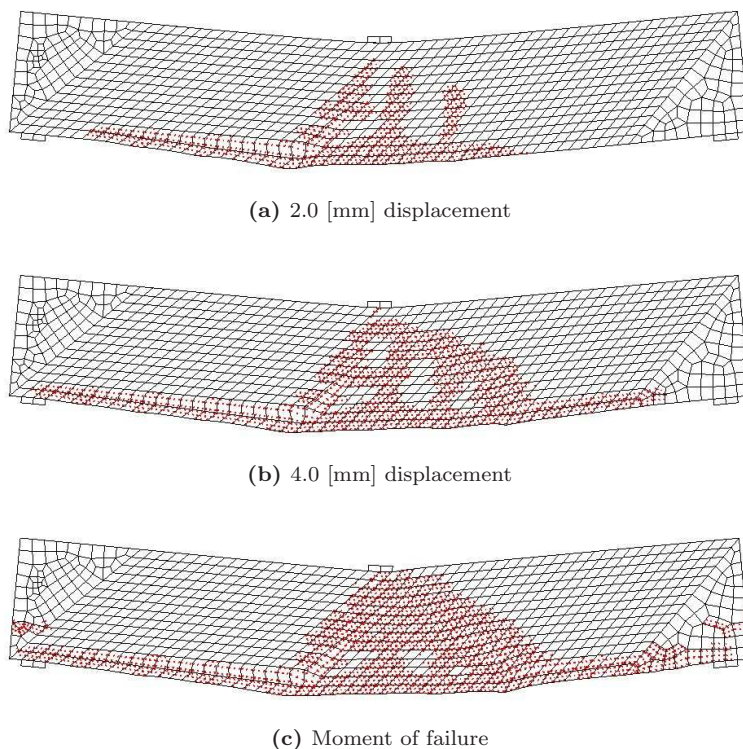


Figure 6.30: Crack pattern for slant quadrilateral mesh

$V=225.7$ [kN], with a failure occurring through the beam reaching its flexural moment capacity. This means that the beams behaves stiffer than a normal aligned mesh.

Both the slanted quadrilateral mesh and the aligned triangular mesh show failure by reaching the moment capacity of the beam.

6.7.3 Symmetrical modeling

The model that was used in all of the previous sections consisted of only half the beam (except for the slanted mesh design), as was depicted in section 6.2.1. In order to determine whether this choice for using symmetry has any influence on the structural response of the beam, an analysis was performed with a model of the entire beam. The results of this analysis are depicted through the crack-patterns in figures 6.31a, 6.31b and 6.31c.

From the first crack-pattern it can distinguished that there are a number of symmetrical flexural cracks, and one large diagonal crack on the right-side of the beam (figure 6.31a). The formation of this crack leads to a redistribution of forces, and to the formation of another large diagonal crack (figure 6.31b), making the crack pattern symmetrical. After this symmetric crack formation the crack propagates only on the left-side of the beam. After an initial drop the beam finally fails abruptly due to the major crack at the left-side of the beam.

From this analysis it is interesting to see that there are large differences as well as large similarities between the analysis. When comparing the symmetric model versus the entire model, the failure mechanisms and crack patterns are very similar. The value for the ultimate shear load differs

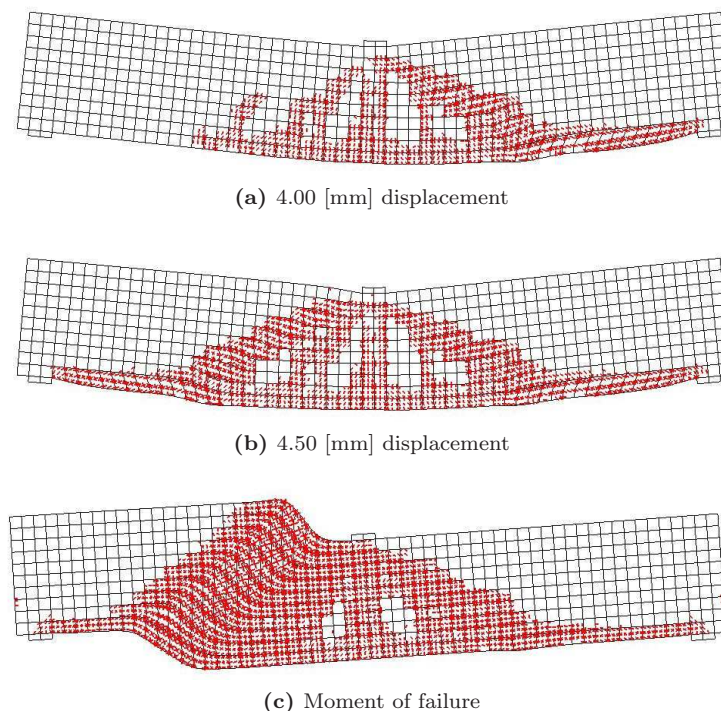


Figure 6.31: Crack patterns of entire beam model

only slightly (1%). Another key similarity is that the moment of failure is very brittle for both models. Besides these similarities, there are significant differences in the total structural behavior up to failure of the beam, as is clearly visible in the load-displacement diagram. The model of the entire beam behaves stiffer in the stages initial cracking, and over the beam also shows a large number of snap-through's that do not occur at all for the symmetry model. This leads to the conclusion that with this particular benchmark, the modeling a symmetric model leads to an a similar failure mode and ultimate shear load value. But it also has a large consequence on the behavior of the entire beam.

Another important aspect is that the entire beam model fails a-symmetrically, this means that the failure mechanisms could also occur in the right-hand-side of the beam. Therefore it is important to rule out the possibility of the randomness of the crack pattern and failure mode, to ensure that we have obtained the correct results with this particular model and set of parameters. The analysis was therefore repeated, and the exact same results were obtained at every instant.

6.7.4 Summary

For this particular benchmark, a directional as well as an dimensional bias is present in case of the application of the rotating crack model. This bias implies that structural response of the numerical analysis, are different in case of differing spatial discretizations. To summarize both the dimensional and directional bias, table 6.4 displays the obtained ultimate load values and the accompanying failure modes. It is clear that large variations occurs and even different failure modes are possible.

Mesh design	Ultimate shear load V [kN]	Failure mode [-]
quadrilateral mesh 50×50 [mm]	200.3	flexural shear
quadrilateral mesh 35×35 [mm]	186.9	flexural shear
quadrilateral mesh 25×25 [mm]	166.3	flexural shear
triangular mesh aligned	218.3	flexural moment
triangular mesh counter aligned	198.4	flexural shear
quadrilateral mesh slanted	225.0	flexural moment
experimental result	162.7	flexural shear

Table 6.4: Summary ultimate shear loads V and failure modes for different mesh designs

An important fact to consider when reviewing the directional bias, is that the rotating total strain model was applied. Because the fixed model allows no rotating of the cracks the directional bias may be of less significance for triangular elements. As was established in the previous section, the fixed model provides results that were of such a poor quality, that an objective comparison could not be made.

6.8 NLFEA versus experimental results

As a final aspect of the first benchmark study, a comparison will be made between the experimental results and the results obtained from the previous sections. The reason that this comparison will be made in the final section, is because the comparison used the information that was obtained in the previous section. The focus will therefore be on the structural aspects to establish the validity of the obtained NLFEA results in comparison with the real-life behavior of concrete beams.

To compare the results, the rotating crack model was selected due to the fact that it was the only smeared crack model that provided consistent results. The constitutive model consisted of exponential softening in tension and parabolic softening in compression. Furthermore, the entire beam was modeled. The reason for this was the earlier discussed differences between a symmetric and entire beam model. Also, the use of the entire beam model will give a better comparison with the experimental results. The mesh was designed with dimensions $b \times h = 25 \times 25$ [mm].

Figure 6.32 depicts the load-displacement behavior as obtained from the experimental results [15] and from the numerical analysis. As can be observed the load-displacement behavior of the experiment differs strongly in comparison to the numerical analysis. Only in the later stage of loading, close to the moment of failure, a similarity is observed in the load-displacement path. The large differences are of unknown origin since the experimental results only mention the normalized displacement and not the exact displacement of the mid-point versus the applied load, as with the performed FE analysis. After verifying with the linear elastic stiffness, the numerical analysis shows the correct stiffness, while the experimental linear elastic stiffness is too small.

Although the load-displacement behavior was very different between the numerical and experimental results, the obtained ultimate load and displacement at moment of failure was similar.

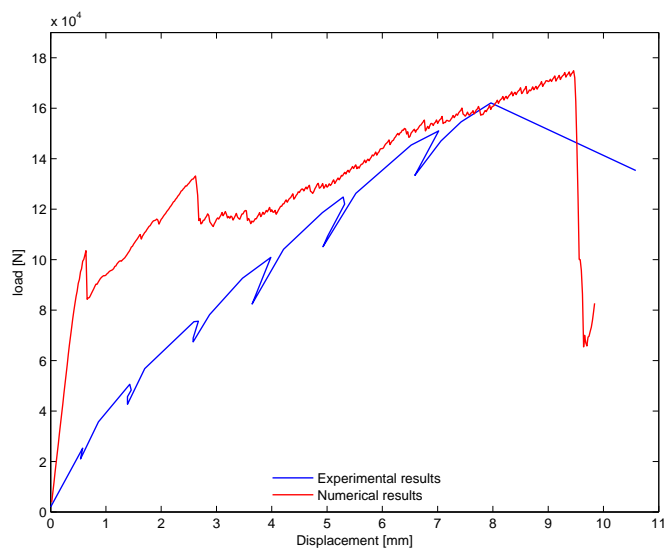


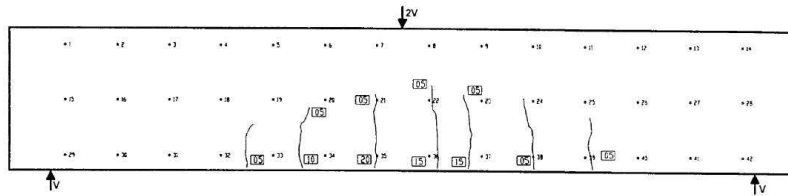
Figure 6.32: Load-displacement diagram for experimental results and numerical analysis results

The numerical analysis failed at a load of 174.3 [kN], which is a difference of 7.0% in relation to the experimentally obtained ultimate load. The displacement at failure is also reasonably similar with a difference of 18.9%. The experimental results also recorded that the beam "displayed no warning as to imminent failure and did not possess any post cracking capacity". This was also recorded as the failure mode in the finite element analysis. However, the possibility exist that the failure of the finite element analysis was due to numerical factors and not due to structural factors. In this particular case however, the sudden failure of the analysis is considered to be caused by structural failure. This conclusion was drawn from three main observations/assumptions, namely: (1) beam already shows extensive cracking, and was expected to reach failure, (2) the experimental results also indicate sudden failure with no post-cracking capacity.

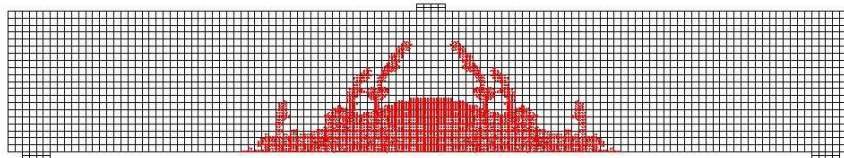
Figures 6.33a to 6.34d depict the crack patterns as obtained from the experimental as well as the numerical results. When considering the initial crack patterns, figures 6.33a and 6.33b, we can distinguish that a number of bending cracks have developed in both the figures. One of the first observations is the blunt formation of the crack pattern for the rotating crack model. The center of the beam shows a somewhat half circle with all the element being cracked, and undergoing softening to certain degree. It can also be observed that the number of cracks that have propagated into the web are fewer in number than in comparison with the experimental crack pattern. The cracks from the rotating crack model also show some significant rotation inwards towards the load-plate. When we continue to the following load-stage, we can see that within a small load increment (25 kN), a large number of cracks have developed in both analysis. However, where the numerical analysis shows large cracks propagating at angles into the web, the experimental crack pattern shows only cracks that just start to rotate towards the load plate. What is also interesting to see is that the numerical analysis shows a crack formation along the entire underside of the beam, while the experimental cracks shows no indication whatsoever of horizontal crack formation. This crack formation at the underside of the beam, was discussed earlier and is considered to be a crack anomaly of the rotating model.

At 150.0 [kN], the experimental crack pattern shows flexural cracks that start to propagate towards the load plate at their crack tips. When comparing this crack pattern with the numerically obtained crack pattern, we distinguish that the crack pattern is more extended than the experimental pattern. Also the critical crack, for which the beam is going to fail, already propagated to the underside of the load plate. At the respective moments of failure of both the experimental and numerical analysis, figures 6.34c and 6.34d, it is visible that the failure modes are very similar. Experimental as well as numerical results show a single large shear crack which propagates from the load plate towards the bottom of the beam. The only difference consist of the shape of this crack. While the numerical analysis shows an straight crack, at approximately 30-40° with the longitudinal axis, the experimental crack pattern shows a crack with a concave form. Both crack-patterns also show a horizontal crack formation near the reinforcement as part of the failure mechanism.

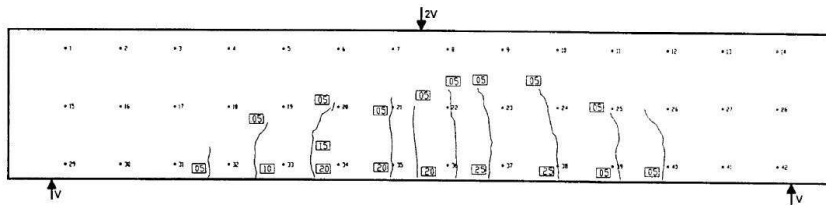
When reviewing the overall performance of the numerical analysis, in this case the rotating crack model, versus the experimental results, the following conclusions were established. It can be concluded that the prediction of the ultimate load, in both the displacement and load value, are in good agreement with the experimental results. Also the failure mode and accompanying crack pattern prediction are reasonably similar. The main drawback of the rotating crack model, as was established earlier, is the over-rotation of the cracks. This over-rotation leads to an unrealistic crack pattern at the underside of the beam. Another issue facing the numerical analysis is the bluntness of the crack pattern, in which little distinction can be made between crack and intact concrete.



(a) 100 kN



(b) 100 kN

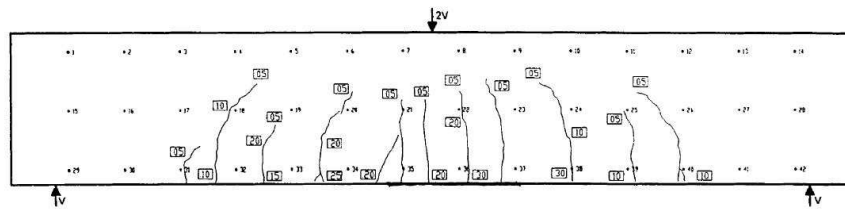


(c) 125 kN

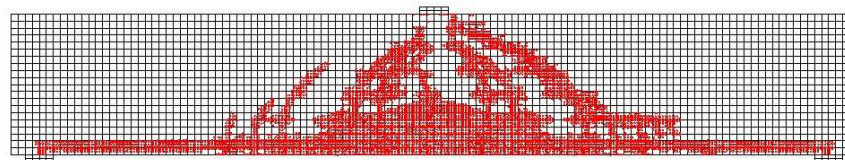


(d) 125 kN

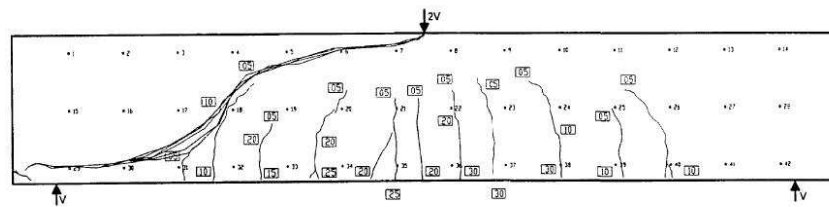
Figure 6.33: Crack patterns obtained from experimental results and from numerical analysis



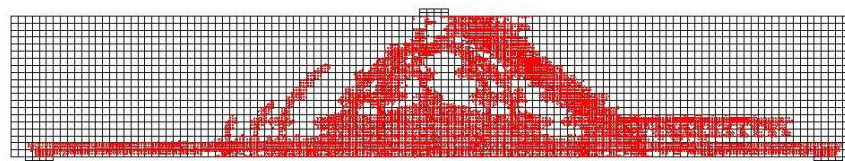
(a) 150 kN



(b) 150 kN



(c) Failure 161.0 kN



(d) Failure 174.3 kN

Figure 6.34: Crack patterns obtained from experimental results and from numerical analysis

7. Benchmark: Beam B

The second benchmark study will be performed on a beam that was also a part of the earlier mentioned workshop on the shear strength of concrete beams. In this workshop the beam was identified as beam #3061, for an uniform approach in this thesis, we will refer to this beam as beam B.

7.1 Beam B properties

7.1.1 Geometry

The beam in question is a simply supported beam, loaded by two concentrated loads. It has a rectangular cross-section, with only longitudinal reinforcement consisting of two bars, no shear reinforcement is present. The total area of reinforcement is 1355 [mm²], which leads to a reinforcement percentage ρ_s of 0.8%. Further geometrical properties are presented in figure 7.1, also included is the crack pattern at moment of failure as was available from the experimental data. The governing crack at which the beam fails is highlighted.

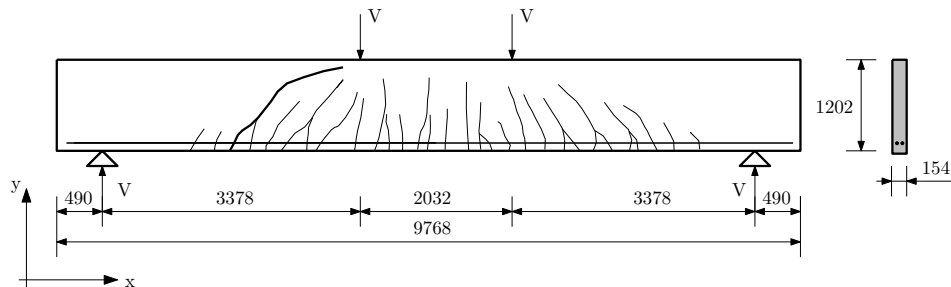


Figure 7.1: Geometry characteristics and crack pattern at moment of failure, the critical crack for which the beam ultimately fails is highlighted. Dimensions are in [mm].

From the geometrical properties it can be concluded that the beam selected for the second benchmark study is a slender beam resulting in a relative large bending stiffness. The absence of shear reinforcement in combination with this large stiffness leads to the probability that the beam will exhibit strong brittle behavior. When regarding the width of the beam, we can also conclude that the formation of a compression strut may be difficult.

7.1.2 Materials

The material properties have been derived from the information provided by the workshop document, values that were not given have been calculated using the CEO-FIP 1990 model code.

Concrete			Reinforcement					
f_{ck}	27.4	[N/mm ²]	ν	0.15	[-]	f_y	398	[N/mm ²]
f_t	2.74	[N/mm ²]	G_f	0.062	[Nmm/mm ²]	E_s	210000	[N/mm ²]
E_c	32766	[N/mm ²]	d_{max}	16	[mm]	ν	0.3	[-]

Table 7.1: Material properties beam B for concrete and reinforcement

7.1.3 Load bearing capacity

The flexural moment capacity of beam B has been determined at 562.4 [kNm] which means an applied load of $V=166.5$ [kN] per loading point. When considering self weight the load is reduced to $V=153.8$ [kN]. The linear elastic capacity of the concrete section, is determined at 101.6 [kNm] which implies a load level of $V=30.1$ [kN].

Using similar reasoning as with the first benchmark beam A, only an estimate is provided for the ultimate shear load based on the shear capacity of the concrete section with an maximum allowable shear stress of $0.4f_t$. This leads to a maximum shear load of $V=73.9$ [kN].

7.1.4 Experimental results

The experimental data was supplied from a test conducted by Prof. Kani at the university of Toronto in 1968 [4]. From these results it was determined that the total load at failure was $V=97.7$ [kN]. Following the remarks [11] that this value represents the lower boundary of the experimental range, an average ultimate value was computed of $V=127.0$ [kN]. From the experimental observations, the following comments were recorded:

Sudden diagonal failure occurred at the west end with a diagonal crack at steel level, the underside crack was approximately 1350 [mm] from the support while the topside of the crack extended under the loading plate". The crack pattern that occurred at failure is depicted in figure 7.1.

When considering the development of the crack pattern, we can distinguish that the first cracks are formed vertically in the region with constant moment. Upon further loading flexural cracks start to appear in the shear span of the beam. These crack eventually grow at angle into the web of beam, leading to the failure of the beam as was recorded. This type of failure is considered to be flexural-shear failure.

7.2 Pre-processing aspects

7.2.1 Modeling environment

Using similar reasoning as was used in the previous benchmark, the second benchmark object will also be modeled using a 2D plane stress state.

7.2.2 Boundary conditions

The boundary conditions of the second benchmark are similar to the previous benchmark. In the centerline of the beam, the condition is enforced that the cross-section will remain perpendicular to the x -axis. To achieve this, all the nodes in the centerline are constrained in the x -direction. In order to let the beam expand and displace freely, the support condition consists only of a constraint in the y -direction.

The load and support forces are introduced via loading plates. The load plates will be connected through an interface element to the concrete. The stiffness of the interface element in the normal direction was set at $8.4e5$ [N/mm³], and the stiffness of tangential direction was set at $k_n=50$ [N/mm³]. The derivation of these quantities was performed in a similar manner as in the first benchmark, see section 6.2.2.

7.2.3 Element selection

The concrete is modeled using iso-parametric eight-node quadrilateral plane stress elements with 3×3 Gauss integration and quadratic interpolation.

The reinforcement will be modeled using discrete truss elements in which the two bars will be modeled as one truss element with the total area of the reinforcement. These elements consist of a 3-node element with two degrees of freedom u_x, u_y per node. The numerical integration occurs through a 2 point Gauss integration scheme.

The discrete option is chosen in favor of the embedded option because the concrete is only lightly reinforced with longitudinal bars. When structures are densely reinforced, an embedded reinforcement is more suitable. Another advantage of discrete modeling is that a bond-slip model can be introduced. Representing the reinforcement with truss elements has the consequence that the bars do not incorporate a possible bending stiffness that can be derived from the bars. Therefore the dowel mechanism does not contribute to the shear capacity.

7.2.4 Spatial discretization

As a first estimate the mesh was designed with dimensions of approximately $b \times h$ of 90×90 [mm], with all of the elements having an aspect ratio of above 0.93 [-]. The chosen dimension represents a normal sized mesh, figure 7.2 displays the finite element model.

7.2.5 Material modeling

The concrete will be modeled with linear softening in tension and parabolic softening in compression (figure 7.3a), unless indicated otherwise. The reinforcement will be modeled using the Von-Mises elastic-perfectly plastic constitutive model, see figure 7.3b.

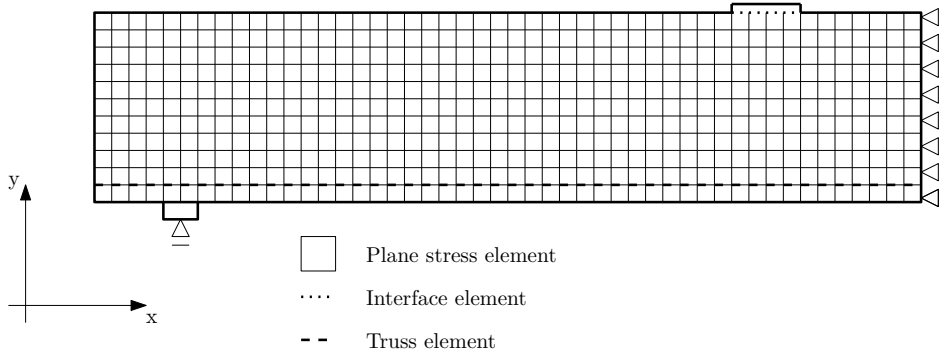


Figure 7.2: Finite element model beam B

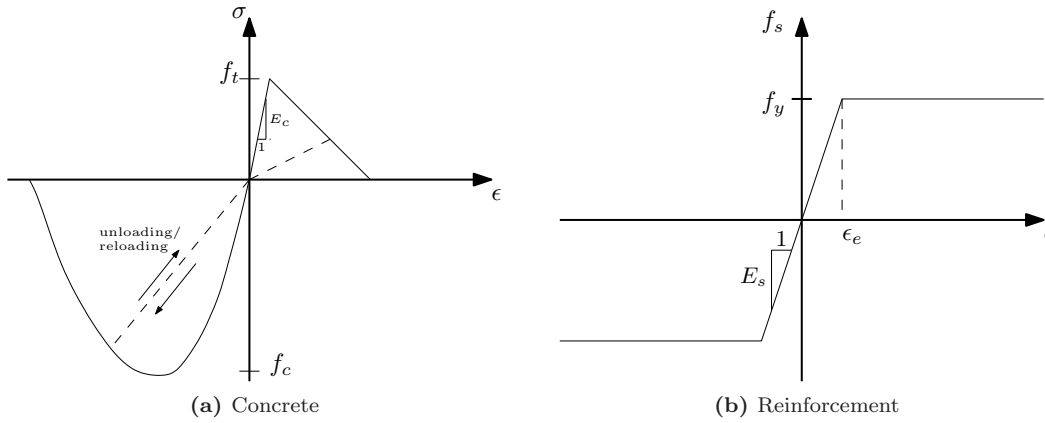


Figure 7.3: Constitutive models reinforcement and concrete

7.3 Preliminary analysis: smeared cracking

A preliminary analysis was performed with the objective of validating the conclusions stated in the previous benchmark study. The beam will therefore be modeled with the same principles that ensured convergent and consistent results in the previous benchmark.

The characteristics of the previous benchmark are defined as following: Rotating crack model in combination with a parabolic softening function for in compression and exponential softening in tension. The iterative method will consist of BFGS method in combination with an explicit line search algorithm. The increment-size will be 0.03 [mm] with convergence governed by the force norm with standard tolerance.

Numerical stability of the previous benchmark was only obtained after applying extensive measures to the incremental-iterative procedure. This particular benchmark proved to lead to even more severe numerical difficulties, which was mainly due to the geometrical properties of the beam. As stated before, the beam has a very slender cross-section in combination with a very small amount of flexural reinforcement and no shear reinforcement. These geometrical properties in combination with the selected crack model would prove to lead to un-realistic crack patterns and failure modes.

Figure 7.4 shows the load-displacement behavior that was found upon analysis. The non-linear part of the structural behavior of the beam starts of with small flexural crack at the bottom part of the beam. At a certain moment a crack propagates from the bottom of the beam up to

underside of the compression zone in a single increment. This crack is depicted in figure 7.5a. The increment in which the crack occurs show a high degree ($>15\%$) of out-of-balance force and consequently, convergence was not obtained. In the load-displacement behavior of the beam, the crack is visible as a large snap-through (see indication figure 7.4). After the formation of this crack, the analysis only shows only a slight increase in load-carrying capacity, before failing at a load of $V=67.3$ [kN]. Failure is caused by a large separation in the y -direction and a large shear displacement of the elements above the reinforcement. The crack pattern of the moment of failure is depicted in figure 7.5c. From this crack-pattern it is also clearly visible that the structural response is very poor. Only a single bending crack has formed in the constant moment region of the beam while no cracks have propagated into the shear span of the beam. Furthermore, due to the over-rotation of the cracks, the entire underside of the beam shows cracks, aligning with the reinforcement.

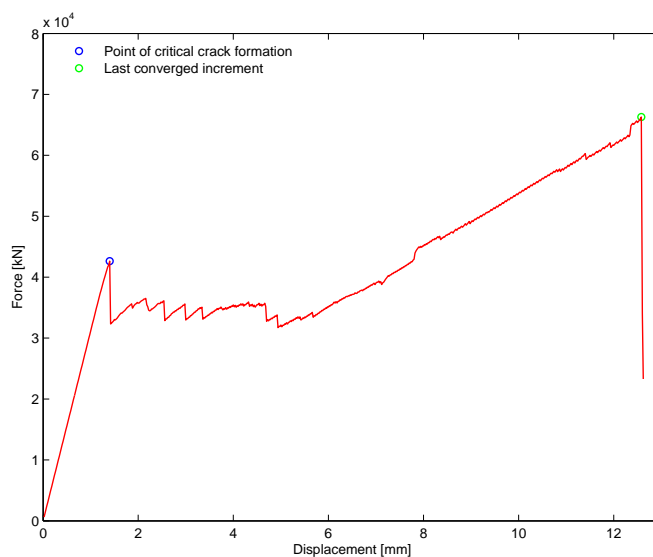
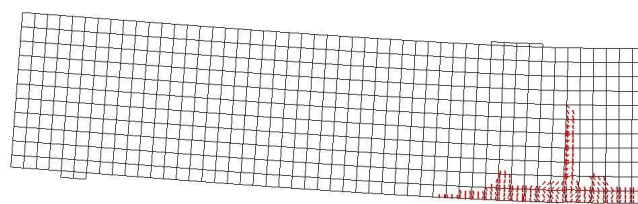


Figure 7.4: Load-displacement diagram with indication of critical events

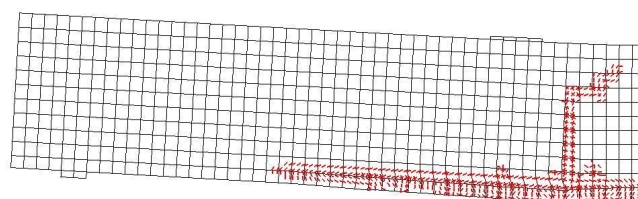
7.3.1 Improving preliminary results: rotating crack model

To improve on the results that were found in the preliminary analysis a number of measures were taken to ensure convergence and improved results. These measures consisted of three categories, namely: (1) selecting different parameters for the incremental-iterative procedure, (2) Selecting different material parameters in order to reduced brittle, e.g. strong non-linear, responses, and (3) Applying a different spatial discretization.

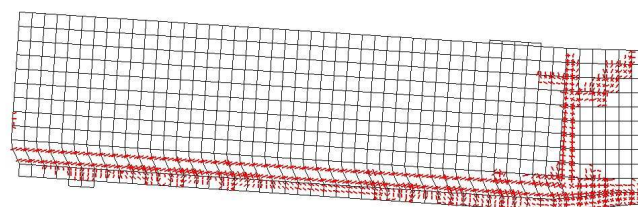
The first category consisted of improving the convergence characteristics through the parameters of the incremental iterative procedure. To achieve this objective a number of parameters were investigated. Firstly, the iterative procedure was investigated whether using a different Secant-Newton formulation or even a standard Newton formulation would lead to a more convergent process. This measure did not prove to be successful. Secondly a smaller increment-size (>0.001) was used to improve convergence. Because of the formation of the critical crack in a single increment, the small increment size was particularly enforced in the neighborhood of the critical



(a) 1.5 [mm] displacement



(b) 4.0 [mm] displacement



(c) 13.3 [mm] displacement

Figure 7.5: Crack patterns during loading of smeared crack analysis beam B

crack formation. But this also proved to be unsuccessful. Furthermore the maximum number of iterations was increased (>750) and a line search technique was applied. Allowing for a very large number of iterations did prove to lead to a fully converged solution, but the structural response corresponding with this fully converged solution was very poor.

In addition to the displacement controlled procedure a force controlled procedure was applied with a crack mouth opening displacement control (CMOD). The CMOD is an extended arc-length method in which the constraint equation is based on the nodal displacements at both sides of a (large) crack. In this particular case, the major crack, as was described in the preceding paragraph, was monitored. This measure however did not improve convergence, but only shifted the crack into the adjacent elements. To avoid this shifting of the crack a consecutive number of CMOD controls were applied. This however proved to be highly numerically unstable.

The second category of measures was applied to the material parameters of the concrete. The main objective of these measure was to decrease the brittle behavior of the beam because of the numerical difficulties that generally accompany this type of behavior. First of all, the concrete tensile strength was varied, but this proved to lead to no significant differences. Next the fracture energy value was doubled (0.15 Nmm/mm^2) but this also proved to be unsuccessful. Following these measure, a Poisson ratio of zero was applied in order to alleviate any numerical problems caused by bi-axial stress-states, but no improvements were realized. Finally the concrete stiffness

E_c was varied. This measure proved to postpone the formation of the critical crack, but eventually all of the analysis performed equally poor with no improvement regarding the convergence and the structural performance. In addition to varying the material parameters there was also a variation between the fixed crack model and the rotating crack model, this however also did not improve convergence or structural response.

As a final set of measures the spatial discretization was scrutinized to improve convergence. These measures consisted of the following aspects: selecting a smaller mesh dimension, using triangular elements, using linear elements and using a model of the entire beam instead of a symmetric model. All of these measures did not improve the numerical stability and the structural response.

Although a fully converged solution was obtained with a large number of iterations, the structural response was very poor. When examining the crack patterns we can distinguish that cracks have only formed in the center of the beam, for which a constant moment is present. The shear span of the beam is completely free of any flexural crack that may have propagated into the web. because the center of the beam is loaded with a constant moment, vertical cracks are expected. In this particular case however, the crack are sloping towards the center-line of the beam. Next to the aforementioned crack, large crack formations are present along the length of the beam at the location of the reinforcement. These crack are considered to be the consequence of the rotating crack model and are not physically justifiable.

7.3.2 Improving preliminary results: fixed crack model

Because some researchers [26] had been able to present better results in using similar crack models and finite element models as used in this thesis, there might be some question regarding the results of the above described analysis. This section will provide an answer to these questions.

One of the objectives of this thesis was to consistently provide numerically correct results. Meaning that in every instance numerical equilibrium was obtained and that the results were not compromised by the choices made in the parameters of the incremental-iterative procedure. One of the main parameters choices in the incremental-iterative procedure is the selection of the size, and the corresponding number, of increments. In using larger increment, difficulties such as the critical crack formation can be overstepped, leading to a different solution.

Therefore, in order to simulate the results of the workshop, an analysis was performed using an increment size of 0.1 [mm]. Further aspects were a fixed crack model with $\beta=0.001$, since the rotating would still lead to incorrect results. Next to the fixed crack model, the fracture energy was doubled and a restart with a previous stiffness matrix was applied in case of the critical crack formation. In using these different aspects the analysis deviate slightly from the initial analysis of the beam. However, the results that were obtained are similar as to the results obtained in the workshop on the shear strength of concrete beams.

To illustrate this, the load displacement diagram has been depicted in figure 7.6 and the crack pattern at various stages of loading are depicted in figures 7.7a to 7.7c. Upon examining the load-displacement diagram, it can be distinguished that the findings of the fixed crack model, even with a very small β , are corroborated through this analysis. After the linear elastic branch,

the fixed crack model displays a slight snap-through. After this initial snap-through, the load-displacement follows a stable load-displacement path towards the moment of failure at $V=170.0$ [kN]. At this load-level the load-displacement path has a horizontal direction, which constitutes the moment capacity of the beam. Upon examining the crack patterns, it can be distinguished that the formation of cracks is in reasonable agreement with the experimental results. Figure 7.7c shows the shear crack for which the beam is expected to fail. The reason that the beam does not fail due to this crack is again caused by the fixed model. Even with a small shear retention factor, the results are considered to be over-stiff with the consequence that failure occurs through reaching the moment capacity of the beam.

However one of the main differences is that, also after extensive loading, the crack patterns of the second benchmarks remain limited, unlike benchmark A. It is viewed, that the main reason for this is the absence of horizontal reinforcement in the web of the beam. Because of the view that the rotation of crack is mainly caused by an incorrect transfer of concrete to steel stresses, this rotation does not occur, simply because there is no reinforcement. And because both the rotating crack model and the fixed crack model are based on the total strain model, both models respond the same with different results. While the rotating crack model allows for over-rotation, leading to incorrect strain localizations. The fixed model uses a shear stresses to control the rotating of the cracks. Therefore this analysis corroborates the findings in the previous benchmark study.

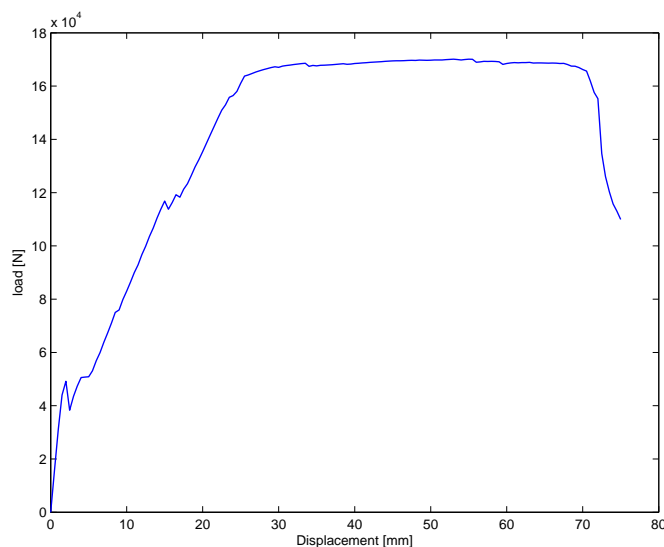
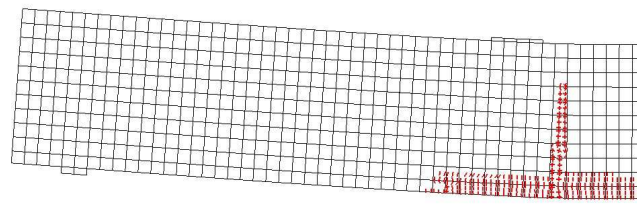


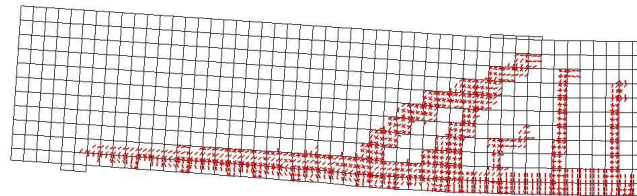
Figure 7.6: Load-displacement diagram using a fixed model and 'forcing' the analysis

7.3.3 Summary

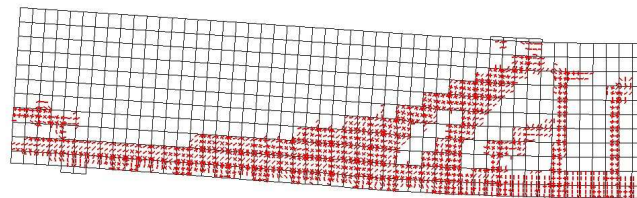
The smeared crack analysis of benchmark B did not lead to structural results that show any similarities with the experimental results. The rotating crack model showed an un-realistic failure mode with accompanying load-displacement behavior. A large number of measures, to improve numerical convergence and the structural behavior, were investigated. However, no improvements were found to be present.



(a) 2.5 [mm] displacement



(b) 15.0 [mm] displacement



(c) 35.0 [mm] displacement (failure)

Figure 7.7: Crack patterns during loading of rotating crack model beam B

Because a correct structural response could not be obtained from the rotating crack model, the incremental-iterative process was adjusted to 'force' the analysis into a certain direction. This 'forcing' was performed using large increment sizes and a fixed crack model. The crack pattern obtained from this analysis showed more agreement with the experimental results. However, in using the fixed crack model, the structural behavior was over-stiff and the failure was caused by reaching the moment capacity.

The main finding from the analysis of benchmark B, is that the smeared crack formulations have large difficulties in representing the structural behavior of a slender beam with no shear reinforcement, that fail due to flexural shear.

7.4 Preliminary analysis: discrete cracking

As was concluded from the preliminary analysis, a correct structural response could not be obtained when using a smeared crack model. Therefore, the second benchmark was continued with a discrete crack modeling study. The principle of discrete crack formulation, were elaborated earlier in section 4.2. In the following section the discrete crack formulation will be applied to obtain an approximation of the experimental failure load and failure pattern.

The preliminary analysis was performed using an approximation of the experimentally obtained crack pattern, as depicted in figure 7.1. The used crack spacing of the flexure induced cracks were set at 200 [mm]. The crack in the center of the beam were allowed to propagate approximately 850 [mm] into the web of beam. The cracks in the shear span were allowed to propagate approximately 670 and 200 [mm] into the web of the beam. The critical crack was modeled using an concave line approximately 1450 [mm] from the support up to the underside of the load-plate, as in correspondence with the experimental comments. The concave shape of the critical crack was selected to improve the mesh process of the beam. Because of the nature of the interface element, e.g. two nodes at either side of the crack, the mesh has to be accommodated for the interface elements. From the experimental crack pattern, it is also observed that the concave crack pattern provides a better estimation, because the crack tend to rotate towards the load plate at a later stage of loading, forming a concave curve.

The constitutive model of the interface element was modeled with linear softening in tension and with a shear stiffness of zero upon cracking. The initial values of the stiffness matrix k_n and k_t were both defined at 10000 [N/mm³], this value proved to sufficiently stiff to model a rigid connection.

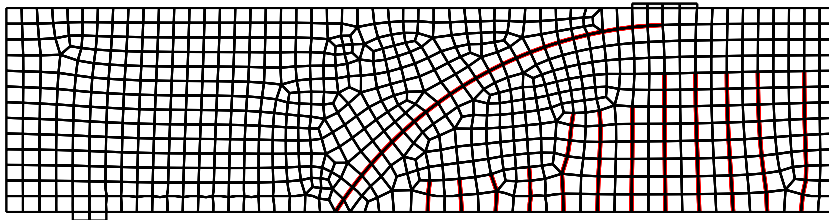


Figure 7.8: Discrete crack-pattern used in preliminary analysis

It was found that the model responds in good agreement with the experimental results and corroborates the findings of the previous section in which a smeared crack analysis was performed. Similar as to the smeared crack analysis, the discrete analysis of the beam showed a large single crack formation in the center of the beam. This flexural crack again propagated violently within a single increment. The consequence of this crack and its extent on the structural behavior is visible in figure 7.10a. In this figure the crack-formation is visible as a snap-through in the load-displacement diagram of the beam, at the end of the elastic capacity of the beam. It is noted that the represented load-displacement diagram was obtained from a fully converged solution. After a number of less severe snap-throughs the analysis find a stable load-displacement path towards failure. The failure load was determined at $V=121.3$ [kN] and was caused by the formation of the critical crack, see figure 7.10d. The ultimate failure load and failure mode show good agreement with the experimental results.

The displacement controlled procedure showed a large and almost vertical snap-through. Although full convergence was obtained, it is important to verify whether this is the actual load-displacement behavior and that the structure does not snap-back. Therefore, a force controlled analysis with arc-length control was applied. From the load-displacement behavior of the force

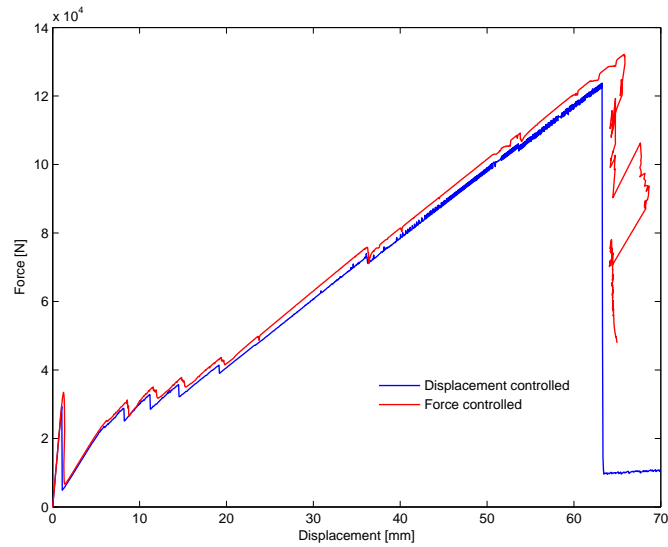


Figure 7.9: Load-displacement diagram for discrete crack model

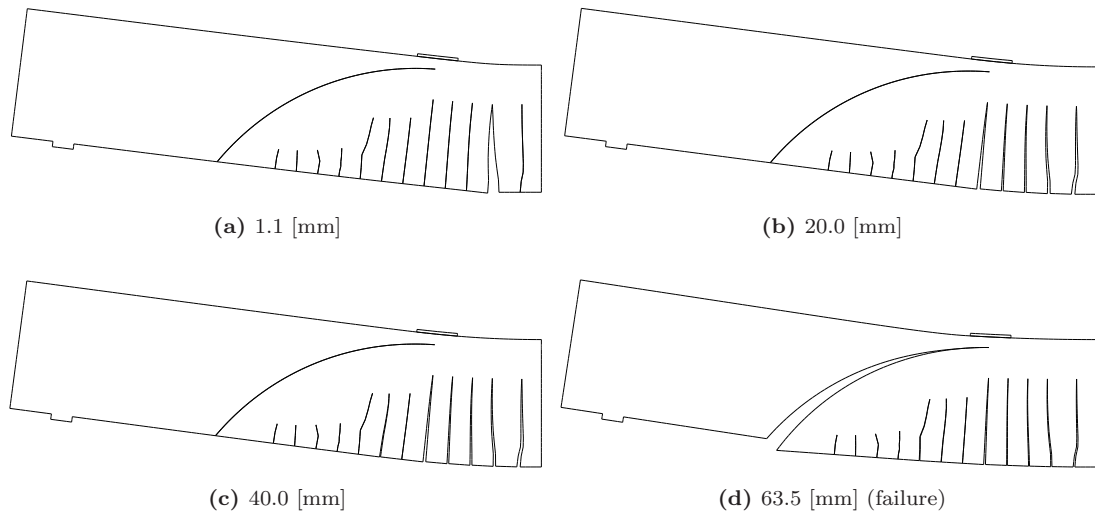


Figure 7.10: Crack patterns at various stages of loading

controlled procedure, it is visible that a very small snap-back occurs. However, after this snap-back, the load-path is almost identical to that of the displacement controlled analysis. Overall, there are no significant differences between both analysis. Only when approaching the moment of failure, the force controlled shows a higher ultimate load ($\approx 10\%$). It may therefore be concluded that the force control and displacement control both provide proper structural results in this instance. However, the force control procedure, similar as with the first benchmark, was characterized by high numbers of non-convergent increments. In total 35% of the increments failed to find convergence within the maximum amount of 150 iterations. Because of these high numbers of non-convergent increments, the force controlled analysis is deemed less accurate.

7.5 Shear formulations for discrete cracking

The preliminary analysis consisted of pure mode I fracture, with upon crack formation, a reduction of the shear stiffness G to zero. The elimination of shear stresses does not constitute an accurate representation of the actual behavior of the beam. Certainly not when cracks are loaded in shear and the aggregate interlock mechanisms occurs. The aggregate interlock mechanisms is in general one of the main load carrying mechanisms in beam with little or no shear reinforcement. In case of the large critical crack, the shear stresses may be significant due sliding across the crack-face.

To investigate the influence of the modeling of a shear stiffness, two different shear formulations were analyzed. The model of the preliminary analysis was extended with a constant shear stiffness and a dilatancy model. The numerical aspects of crack dilatancy were discussed in section 4.2.2. The principle of dilatancy models is to provide a relation between the shear slip Δu_t and crack width Δu_n with the shear stress on the crack face. The model used for the analysis consisted of the rough crack model as developed by Bažant and Gambarova [1].

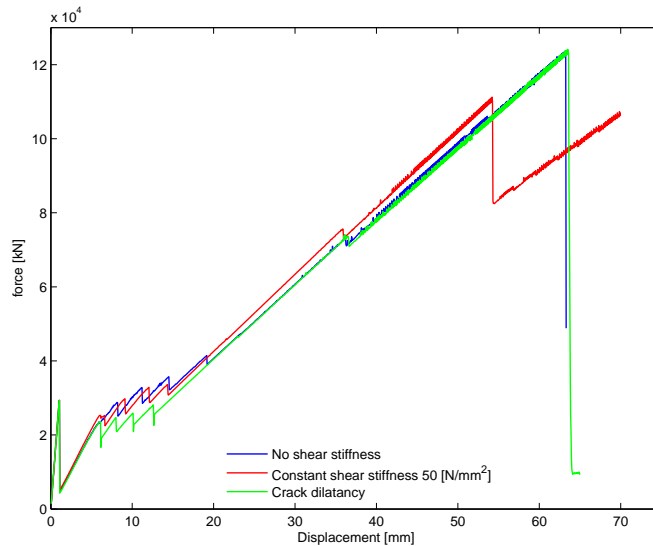


Figure 7.11: Load-displacement diagram for discrete crack model with shear stiffness formulations

Figure 7.11 shows the load-displacement response of the discrete model with the different shear formulations. The analysis with the constant shear stiffness consisted of a stiffness of $50 \text{ [N/mm}^2\text{]}$. The analysis was ended at 70.0 [mm] displacement because of excessive shear stresses on the critical crack, while the crack was completely softened in mode I (see figure 7.12). This behavior is one of the main drawbacks of a constant shear stiffness, as was also visible in the previous benchmark study with the application of the fixed total strain model. Although failure was not obtained, it can still be concluded that there is very little difference between the load-displacement behavior of both models. From this it can also be concluded that the flexural cracks show little to no resistance against shear displacement.

The analysis including the rough crack model, showed very little difference with regards to the preliminary analysis. In fact it showed almost similar load-displacement behavior. Only in

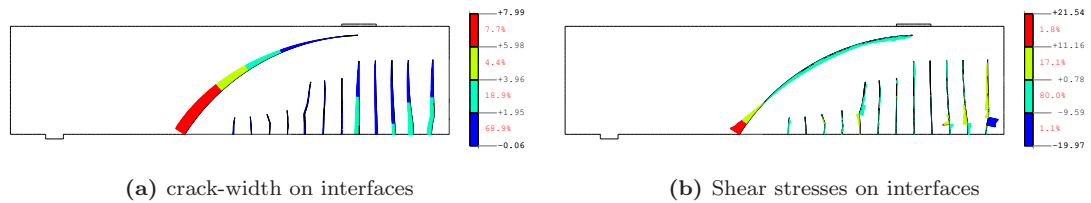


Figure 7.12: Crack-width and shear-stress on crack-faces with constant shear stiffness, at 70.0 [mm] displacement

the beginning stages in which flexural cracks are forming, some slight differences in the load-displacement behavior are present. After this initial tension-stiffening phase, the rough crack model analysis follows a similar load-displacement path towards failure. The accompanying ultimate shear-load showed little difference (1%) with the experimental ultimate shear-load.

It was expected that the flexural cracks would undergo only negligible shear displacement, and that the large shear crack was expected to show more extensive shear displacements and consequently shear-stress. One of the main reasons why the aggregate interlock mechanisms did not fully develop was due to the brittle nature of the beam. Because of this brittle nature the formation of the critical crack coincides with the failure of the beam. This is illustrated in figures 7.13a to 7.13f. These figures display the crack-width and the shear-slip during the two increments in which the critical crack is formed and the beam fails. Figure 7.13a and 7.13b show the moment right before the formation of the critical crack in which the flexural crack are open, the critical crack is at that moment still closed. The following increment, figures 7.13c and 7.13d, show the opening of the critical crack to a maximum crack-width of approximately 5.8 [mm], at this moment a shear-slip is also present of approximately 0.8 [mm]. This ratio of crack-width and shear-slip does lead to significant shear stresses on the crack face. However, when examining the subsequent increment, it can be distinguished that the crack-width has already increased to a maximum of 11.8 [mm]. The consequence of this being, that the crack-width has such a magnitude that it would be un-realistic to model aggregate interlock. The rough crack model also considers this and uses a limit of $\Delta u >^1 /_2 D_{max}$, in which Δu is the crack-width and D_{max} is the maximum aggregate size. Beyond this limit there is considered to be no aggregate interlock mechanism. Another important aspect, next to the sudden failure, is that the failure crack is un-constrained. The aggregate interlock mechanism has therefore limited influence.

7.6 Symmetrical modeling

From the previous benchmark it was concluded that there is a significant difference in case of modeling the entire beam or modeling only the symmetric half. It was found that the load-displacement behavior was affected by cracks that occur in both shear spans in an entire beam model. In relation to the ultimate shear load, the analysis showed mixed results. One analysis showed a small difference (1%) while a finer mesh dimension showed a larger difference (13%).

This section will investigate the influence of modeling only the symmetric half of the structure or modeling the entire structure with discrete cracks. To this end, two finite element models with

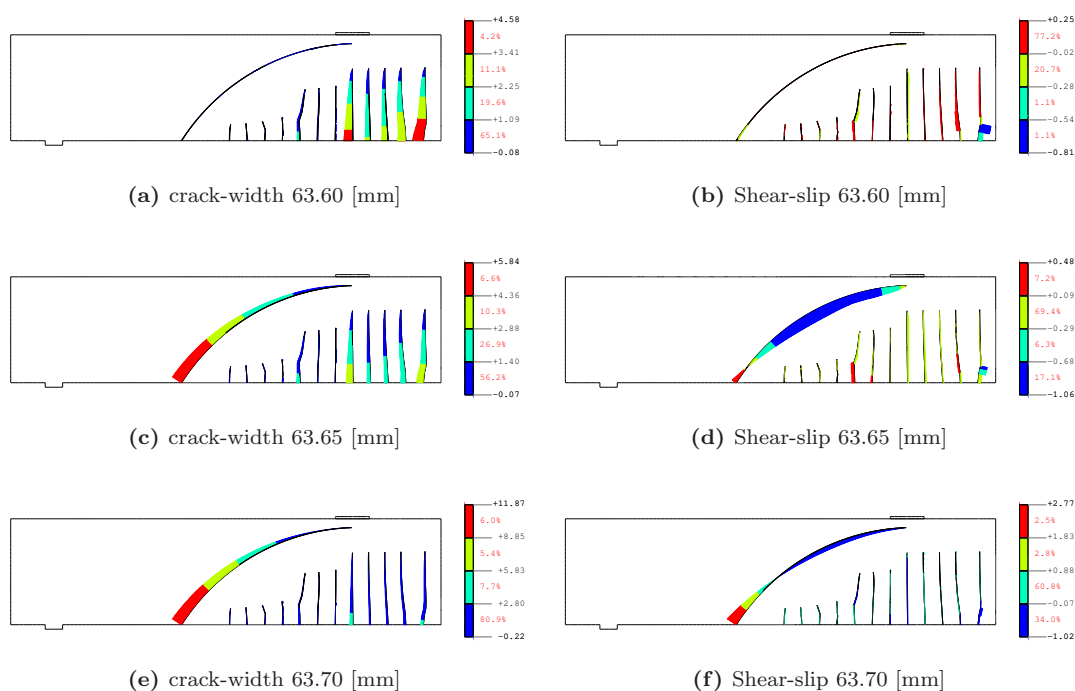


Figure 7.13: Crack-width and shear-slip on crack-faces employing the rough crack model. Displayed increments represent the moment of failure

discrete cracks were developed. The first model consisted of a mirrored discrete crack pattern as used in the preliminary analysis. The second model also consisted of a mirrored version of the discrete bending cracks, but included a smaller critical crack and the left-hand side of the beam. The reason for this was that the failure of the perfect symmetrical model, was indeed symmetrical.

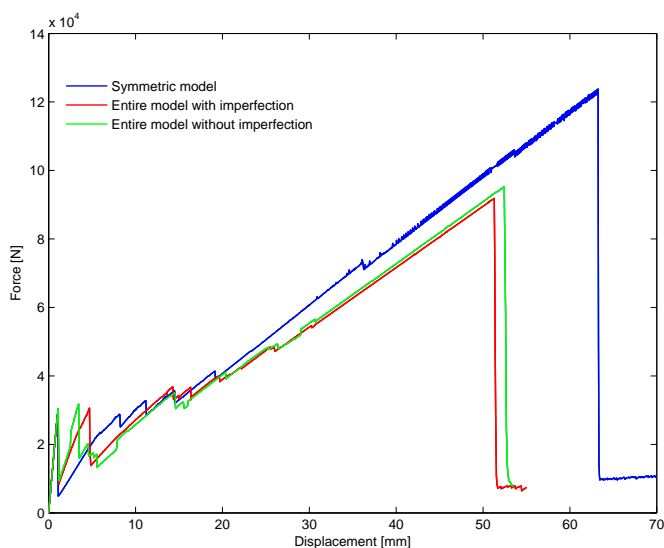


Figure 7.14: Load-displacement diagram for entire beam and symmetric beam models

The load-displacement diagram in figure 7.14 displays three analysis, next to the described complete beam models, the symmetric model of the preliminary analysis was included for comparison.

From the load-displacement diagrams it is clearly visible that the complete beam models show a significantly lower ultimate shear load than compared to the symmetric model. The ultimate shear load is $V=97.6$ [kN] which implies a difference of approximately 21% with the preliminary analysis. Another observation is that the overall stiffness of the entire beam model is consistently smaller after the initial snap-throughs.

The finite element model in which the discrete crack were perfectly mirrored, showed a failure of both critical cracks at the same time. This failure is visible in figure 7.15c which shows the deformed beam at the moment of failure. Although the beam fails symmetrically, the crack development does exhibit consecutive crack formations. Meaning, that first a crack will appear in one side of the beam followed by a crack propagation in the opposing side. This is also the case for the critical crack formation, which begins on the right-hand side of the beam. To investigate whether this symmetric cracking pattern has a large influence on the load-displacement behavior, an imperfect model was analyzed. This model consisted of a smaller critical crack at the left-hand side of the beam. Upon analyzing the imperfect model, it was found that the differences are negligible, and that the ultimate shear load value has a similar value of $V=94.5$ [kN].

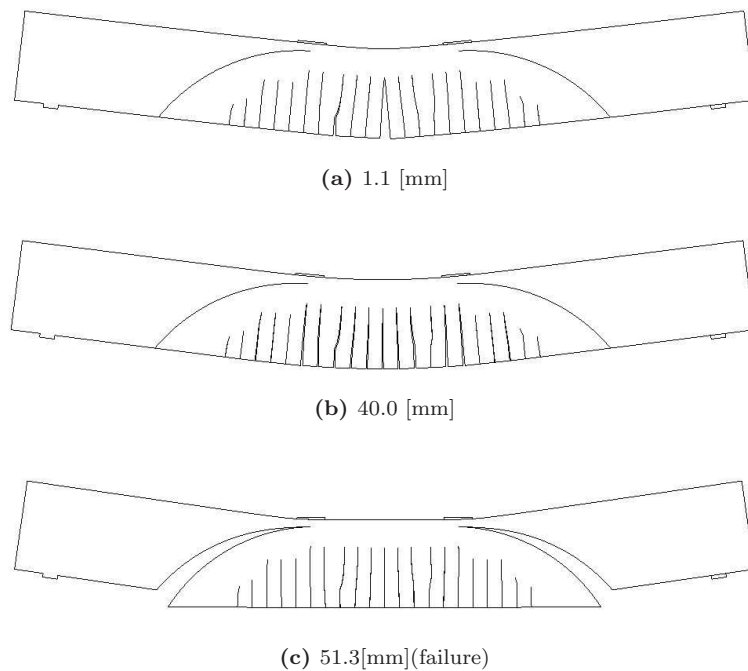


Figure 7.15: Deformed models at respective moments of failure, deformations are exaggerated.

8. Conclusions and recommendations

The following conclusions regard the findings of the two investigated benchmark beams. The conclusions consist of five different categories, namely: (1) structural behavioral characteristics of shear critical beams, (2) the incremental-iterative procedure, (3) constitutive models, material parameters and crack models, (4) spatial discretization, and (5) discrete crack models.

8.1 Structural behavior of shear critical RC beams

The shear critical beams that were analyzed in this thesis exhibited strong non-linear responses, leading to irregular load-displacement behavior with large snap-throughs. No snap-back behavior was found to be present in both benchmarks. Analysis of both beams exhibited no warning as to imminent failure and did not possess any post-cracking capacity, once the failure crack had developed. This behavior was supported by the experimental results and by the fact that no post-cracking load carrying mechanisms were included such as aggregate interlock or dowel action. The main cause for these brittle responses were sudden crack formations within single increments. Analysis of both beams also were characterized by bi-axial stress states in the shear spans of the beams. These stresses were caused by the formation of compression diagonals, the reduction of element stiffness due to cracking, the relatively high level of shear stresses, and the reinforcement action (if present). One of the main consequences of all these components is that a rotation of principal directions occurs. This is of particular importance for the smeared crack models.

8.2 Numerical aspects incremental-iterative analysis

Convergence of the incremental-iterative procedure was difficult to obtain, this was caused by two main reasons: (1) the brittle nature of shear critical beams, and (2) the strain-localizations associated with crack formations. With regards to the first reason, the brittle nature of the shear beams leads to large and sudden crack formation. The consequence being that the stiffness is severely affected, as can be derived from the load-displacement behavior. The incremental-iterative procedure does not have the intrinsic qualities to cope with strong non-linear behavior, therefore convergence was difficult to obtain. In relation to the second reason, the strain-localization phenomenon leads to high levels of out-of-balance force caused by limited number of degrees of freedom. These localizations may not be accurately sensed by the global stiffness matrix that is constructed in the iterative procedures. Another issue with the strain-localizations is that multiple cracks undergo loading, unloading and reloading. This may lead to varying levels of the out-of-balance force, which can lead to a more numerical problematic incremental-iterative process

Although convergence is difficult to obtain, it is not impossible. The following measures proved to be successful in reaching convergence. Using an iterative method based on a Secant-Newton

formulation (in this case the BFGS method) proved to lead to full convergence in all instances. It was also concluded that the BFGS method could provide consistent results with varying increment-sizes. This iterative procedure however, was characterized by a distinct and strongly oscillating convergence behavior. The use of an iterative method based on tangential stiffness, e.g. regular or modified Newton-Raphson, did not lead to full convergence in any of the performed analysis.

Furthermore, if convergence is to be achieved, the incremental-iterative procedure should consist of small increment-sizes, and large numbers of iterations. The large number of iterations are particularly necessary because of the oscillating behavior of the Secant-Newton procedure. Exact values for the number of iterations or the increment-sizes cannot be given, because these quantities are very problem dependent. However, as an indication, full convergence was obtained with approximately 1000 increments and the maximum amount of iteration set at 150 [-] for both benchmarks. It was also concluded that the combination of a small increment-size with a smaller amount of iterations is more computationally efficient than a large increment-size (fewer load-steps) with a larger number of iterations.

It was also found that only displacement-controlled procedures could provide a fully converged incremental-iterative procedure. Force control, with or without arc-length control, could not lead to full convergence. The application of local constraint techniques such as indirect displacement control or crack-mouth opening control could not improve convergence. From this conclusion it is important to understand that true snap-back behavior in the load-displacement curve cannot be captured by a displacement controlled analysis. It was therefore verified that this behavior did not occur for the investigated benchmarks.

8.3 Constitutive model parameters

The behavior of concrete in tension was defined by three main parameters: (1) the tensile strength, (2) the fracture energy, and (3) the shape of the softening curve. It was found that the tensile strength has a significant influence on the structural behavior of the beam, the failure mode and the ultimate shear load. The other parameters proved to be of less significance, only leading to small variations in stiffness and ultimate load values.

Next to the tensile behavior it was concluded that it is also important to include compressive softening in the constitutive model of concrete. Including compressive softening is important for the accurate representation of the formation and degradation of the compression struts. Not including compressive softening also lead to compressive stresses that exceeded the compressive yield strength.

8.4 Crack model evaluation

This thesis investigated three smeared crack models, namely: (1) the fixed model, (2) the fixed multidirectional model, and (3) the rotating model. From these investigations the following conclusions were reported.

In benchmark A, the fixed crack model in combination with a constant shear retention factor proved to result in very poor structural behavior. Although the fixed models provided good structural responses in the early stages of crack formations, the rotation of the principal strain directions in later stages of loading severely corrupted the results. This rotation of principal directions lead to excessive stress-locking through shear stresses on the crack faces. This excessive stress-locking lead to widespread and unrealistic crack patterns, with the beam exhibiting load-carrying capacity completely through shear stresses on the crack faces. Selecting a shear retention factor that approaches zero ($\beta = 0.005$) did not improve the structural response. As a final aspect for benchmark A, a fixed crack model based on variable shear retention was applied. Although slightly less stress-locking was found to be present, it was to such a degree that it constituted an accurate representation of the behavior of the beam.

After analysis of benchmark B with the fixed crack model, it was observed that the cracks did not propagate to the same extent as with benchmark A. However, for elements containing the bottom (and only layer of reinforcement) the crack pattern did show excessive propagation. Although the second benchmark was not corrupted by excessive cracking, the structural response remained too stiff because of stress-locking and caused the beam to fail by reaching it's moment capacity.

The rotating crack model analysis of benchmark A, exhibited good structural responses and provides a reasonable approximations of the experimental results regarding the failure modes and ultimate failure loads. However, the crack patterns that were obtained from the rotating crack showed little distinction between individual cracks. Another drawback, intrinsic to the rotating crack model, is that over-rotation of crack occurs near reinforcing bars. The consequence of over-rotation of crack is that unrealistic crack patterns and strain-localizations occur near reinforcing bars. These strain-localizations lead to vertical and shear deformation of elements along reinforcing bars. It was found that the influence of the over-rotation was displayed more excessively in case of a finer mesh dimension.

In case of the second benchmark, it was not possible to obtain correct structural results using the rotating crack model. The reason for this was the brittle nature of the beam, caused by the dimensions of the beam and the small amount of reinforcement. A large number of measures were applied to ensure convergence of the incremental iterative procedure. And although full convergence was obtained, the structural response remained very poor with only one single bending cracks in the constant moment area of the beam. No cracks had developed in the shear span of the beam, except for cracks along the entire underside of the beam. This part of the beam contains the bottom reinforcement and shows extensive crack-rotation.

In relation to the over-rotation of cracks, it was found that the total strain models (fixed and rotating) have the tendency to show rotation of principal strain directions, and therefore cracks, near reinforcement. The fixed total strain model responds to rotating principal directions by fixing the crack through a shear stress. It is viewed that this generation of shear stress leads to the extensive crack pattern in the fixed crack model. The rotating crack model does allow for rotating of crack, however this leads to incorrect stiffness properties in initially un-cracked directions, which leads to large shear deformations in elements containing reinforcement. It is viewed that this large shear deformation leads to the extensive crack propagation in the rotating crack model. The rotation of principal strain directions is viewed to be caused by: the co-axiality

principal between principal directions, a poor transfer of concrete stresses to steel stresses, and the loading conditions present in shear critical beams. The first two statements however, could not be fully verified.

The fixed multidirectional crack model was not numerically robust enough for the analysis of both benchmark beams, and caused divergence of the incremental-iterative process. Measures to avoid this behavior included using a constant tension cut-off instead of a linear tension cut-off, the use of smaller increments, the use of a zero poisson ratio and the use of linear softening. However, all of the measures failed in avoiding divergence.

8.5 Spatial discretization

With regards to the spatial discretization of the benchmarks, the following conclusions were established regarding three categories, namely: (1) dimensional bias, (2) directional bias, and (3) symmetric modeling.

The strain-localizations tends to occur in rows of single elements, regardless of the element size. The objectivity of energy consumption appears to be remain valid because the strain values are higher in case of a finer mesh dimension, this however was not verified. A significant difference ($\simeq 30\%$) in ultimate failure load was discovered upon analyzing different mesh dimensions.

In general it was found that the quadrilateral element perform optimally when the aspect ratio is near 1.0 [-]. The crack formation and propagation with these types of elements were in good agreement with the experimental results. Next to the standard rectangular quadrilateral mesh, it was found that a slanted quadrilateral mesh displayed poor structural results in crack formation, crack propagation as well as failure modes and failure loads.

The use of triangular elements for the modeling of concrete fracture displayed a distinct directional bias, leading to unrealistic structural results. This directional bias was particularly visible upon comparison of crack-aligned triangular elements with counter crack-aligned triangular elements. In both cases the crack formation and propagation were severely influenced.

As a final aspect, the structural results of an entire beam model was investigated and compared versus the structural results of a symmetric model. On one occasion it was found that the ultimate load was not affected, and on two occasions a difference of 20-25% was found for the ultimate shear load. Although no consistent results were obtained with regards to the ultimate shear load, the load-displacement behavior was severely affected on all occasions.

8.6 Discrete cracking

Because of the earlier described poor structural responses of beam B in using the smeared crack model, a discrete crack model was employed. The discrete fracture pattern was based on the experimentally obtained fracture pattern, with a number of bending crack and one single shear crack for which the beam ultimately fails.

The first analysis of the discrete crack pattern only consisted of mode I softening with upon crack formation a reduction of the shear stiffness to zero. The structural results from this model were in good agreement with the experimental results. Both in failure mode as in failure load. The first analysis also displayed the formation of a very large bending crack constituting a severe snap-through in the load-displacement behavior. This crack formation corroborates the conclusions why the smeared crack models could not lead to correct structural behavior.

Because the reduction of shear stiffness to zero upon crack formation, does not constitute a correct portrayal of the actual behavior, two different shear formulations were investigated. It was found that the constant shear stiffness provides over-stiff results because the shear stress remains on the crack-face. The other shear formulation consisted of a dilatancy model to account for the aggregate interlock mechanism on the crack face. However, the structural response when this model was included, displayed no significant differences between the model with zero shear stiffness. This was mainly due to the fact that the crack-face of the critical shear crack was unconstrained, and the fact that the failure was sudden with large crack-widths and small amount of shear-slip.

8.7 Recommendations

The following sections will shortly discuss what in the view of the author constitutes a correct (or least incorrect) non-linear analysis of a shear critical beam.

8.7.1 Recommendations for the NLFEA for shear critical RC beams

The incremental-iterative analysis should consist of a Secant-Newton procedure, with an explicit line search technique. If the user has a choice whether to apply load or displacement control, the latter should always be selected. Only in the case when snap-backs are a possibility, should the force controlled procedure be used in favor of the displacement controlled procedure. Other aspects of the incremental iterative procedure are: small increment sizes, large number of iterations and the use of the force norm with a tolerance of 0.01 [-]. In both benchmark an average of approximately 1000 increments was used for consistent and convergent results. The maximum number of iterations for both the benchmark beams was 150 [-].

The most viable model for smeared crack modeling is the rotating total strain model. To verify the results of smeared crack modeling, or if smeared crack modeling fails, discrete crack modeling should be applied. The tensile behavior of concrete should be modeled with a exponential softening function. The concrete compression model should consist of a softening branch to account for the formation and degradation of the compression struts. The tensile strength of the concrete structure in question is of critical importance, if there are uncertainties regarding the exact value, multiple analysis should be performed.

For an accurate representation of the structural behavior of the model, it is recommended to use an entire beam model. The used element should preferably be 8-node quadrilaterals with an aspect ratio of $\simeq 1.0$ [-] and should be integrated using a 3×3 Gauss integration. If the use of

triangular elements is inevitable than these elements should be integrated using a 7-point Gauss integrations scheme. The mesh dimensions should be selected relative small, in benchmark A this constituted a dimension of $b = h$ being approximately $1/20$ of the height of the beam.

To accurately model the introduction of forces into the concrete, load-plates should be applied. To avoid un-realistic stresses and structural behavior, interface element need to be constructed to model the actual connection between the concrete and the load-plate.

Bibliography

- [1] BAŽANT, Z. P., AND GAMBAROVA, P. G. Rough cracks in reinforced concrete. *ASCE journal of the structural engineering* 4 (1980), 819–842.
- [2] BAŽANT, Z. P., AND OH, B. Crack band theory for fracture of concrete. *Materials and structures* 16 (1983), 155–177.
- [3] BAŽANT, Z. P., AND PLANAS, J. *Fracture and size effect in concrete and other quasibrittle materials*. CRC Press, 1998.
- [4] BENTZ, E. Experimental test results: Kani’s lost shear test. Beam nr. 3061 / Benchmark beam A, 2008.
- [5] BORST DE, R., AND NAUTA, P. Non-orthogonal cracks in a smeared finite element model. *Engineering Computations* 2 (1985), 35–42.
- [6] BORST DE, R., AND SLUYS, L. J. *Computational methods in non-linear solid mechanics*. Mechanics and Constructions group, Faculty of Civil Engineering and Geosciences, 2002.
- [7] CRISFIELD, M. A. A faster modified Newton-Raphson iteration. *Computer methods in applied mechanics and engineering* 20 (1978), 267–278.
- [8] CRISFIELD, M. A. Accelerated solution techniques and concrete cracking. *Computer methods in applied mechanics and engineering* 33 (1982), 585–607.
- [9] CRISFIELD, M. A., AND WILLS, J. Solution strategies and softening materials. *Computer methods in applied mechanics and engineering* 66(1988) (1988), 267–289.
- [10] FEENSTRA, P. H., AND ROTS, J. G. Comparison of concrete models for cyclic loading. *Committee report ASCE: modeling of inelastic behavior of RC structures under seismic loads* (2001), 38–55.
- [11] GIJSBERS, F. B. J., AND ROTS, J. G. Evaluatie resultaten workshop: empirisch/analytische en numerieke modellen. Tech. rep., TNO Built environment and geosciences, 2008.
- [12] HILLERBORG, A. MODEER, M., AND PETERSON, P. E. Analysis of crack formation and crack growth in concrete by means of fracture mechanics and finite elements. *Cement and concrete research* 6 (1976), 773–782.
- [13] KIKSTRA, W., AND DE WITTE, F., Eds. *DIANA User’s manual release 8.1*. TNO building and construction research, 2002.

-
- [14] LI, Y. J., AND ZIMMERMAN, T. Numerical evaluation of the rotating crack model. *Computers and structures* (1998), 487–497.
- [15] PODGORNIAK-STANIK, B. A. *The influence of concrete strength, distribution of longitudinal reinforcement, amount of transverse reinforcement member size on shear strength of reinforced concrete members*. PhD thesis, Department of Civil Engineering University of Toronto, 1998. Beam nr. 5 / BND50 / Benchmark beam B.
- [16] PRUIJSSERS, A. F. *Theoretical and experimental analysis of the behavior of cracked concrete under monotonic and cyclic shear loading*, vol. 33 no. 4. Heron, 1988.
- [17] REINHARDT, H. W. Fracture mechanics of an elastic softening material like concrete. *Heron* 29 (1982).
- [18] RIJKSWATERSTAAT. Inventarisatie kunstwerken (bruggen, tunnels en viaducten). *Ministerie van Verkeer en Waterstaat* (2007).
- [19] ROTS, J. G. *Computational modeling of concrete fracture*. PhD thesis, Department of Civil Engineering, Delft University of technology, 1988.
- [20] ROTS, J. G. Crack models for concrete: discrete or smeared? fixed, multidirectional or rotating? *Heron vol. 38 no. 4* (1993).
- [21] VECCHIO, F., AND LAI, D. Crack shear slip in reinforced concrete elements. *journal of advanced concrete technology* 2 nr. 3 (2004), 289–300.
- [22] VECCHIO, F. J. Analysis of shear-critical reinforced concrete beams. *ACI Structural journal No. 97-S12* (2000).
- [23] VECCHIO, F. J. Non-linear finite element analysis of reinforced concrete. *ACI Special publication, Finite Element Analysis of Reinforced Concrete Structures No. SP-205* (2002), 1–14.
- [24] VECCHIO, F. J., AND COLLINS, M. P. The modified compression field theory for reinforced concrete elements subjected to shear. *ACI Journal* 83 22 (1986), 219–231.
- [25] VECCHIO, F. J., AND COLLINS, M. P. Compression response of cracked reinforced concrete. *Journal of Structural Engineering ASCE* (1993).
- [26] VERVUURT, A. H. J. M., AND LEEGWATER, G. A. Workshop on the assessment of the shear strength of concrete structures. Tech. rep., TNO Built environment and geosciences, 2008.